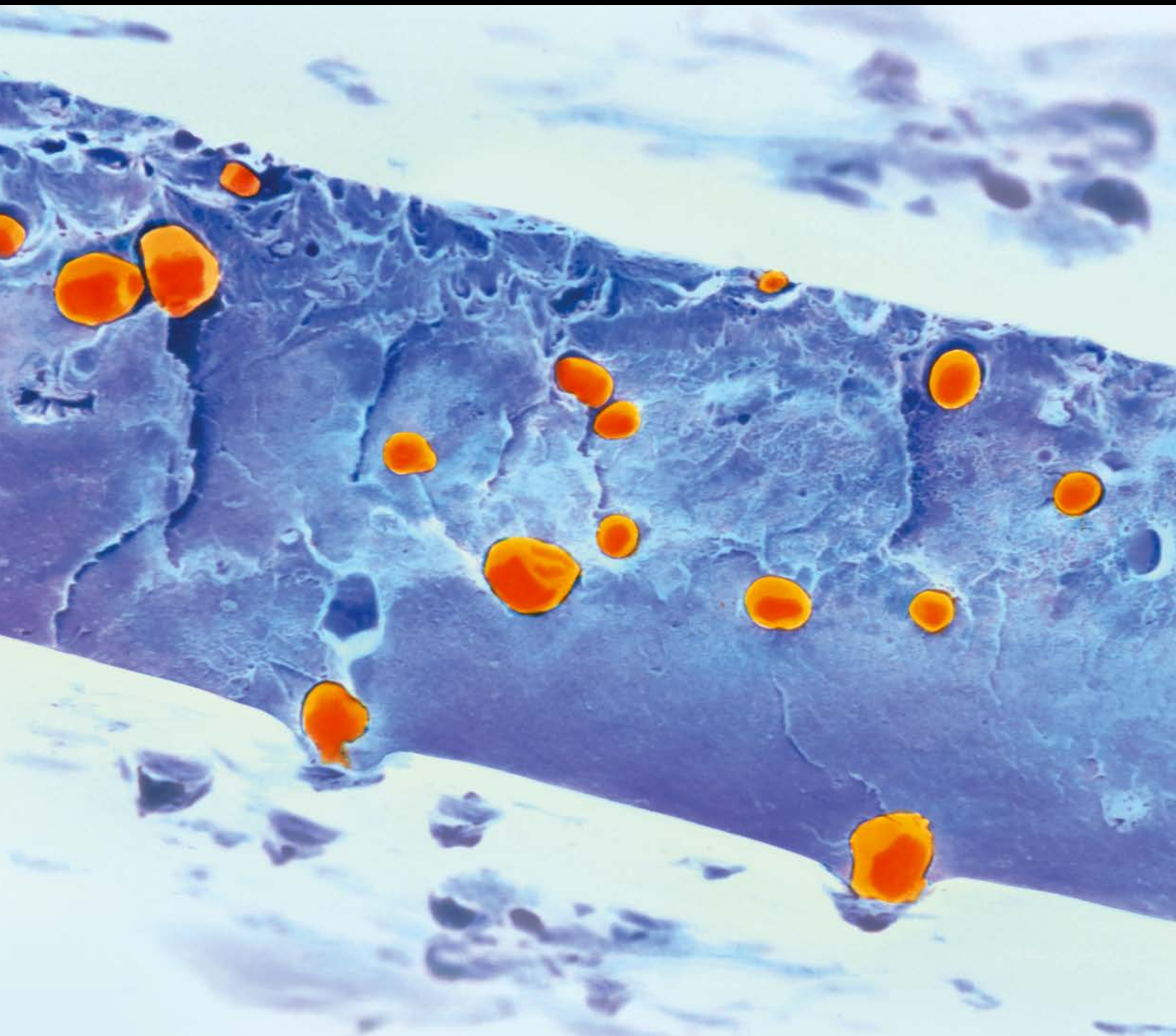


International Journal of Polymer Science

Functional Polymers for Biointerface Engineering

Guest Editors: Qiang Wei, Jie He, Weifeng Zhao, and Yin Chen





Functional Polymers for Biointerface Engineering

International Journal of Polymer Science

Functional Polymers for Biointerface Engineering

Guest Editors: Qiang Wei, Jie He, Weifeng Zhao,
and Yin Chen



Copyright © 2017 Hindawi Publishing Corporation. All rights reserved.

This is a special issue published in "International Journal of Polymer Science." All articles are open access articles distributed under the Creative Commons Attribution License, which permits unrestricted use, distribution, and reproduction in any medium, provided the original work is properly cited.

Editorial Board

Domenico Acierno, Italy
Sharif Ahmad, India
Mats R. Andersson, Australia
Luc Averous, France
Massimiliano Barletta, Italy
Christopher Batich, USA
Giuseppe Battaglia, UK
Marc Behl, Germany
Laurent Billon, France
David G. Bucknall, USA
Andrea Camposeo, Italy
Wen Shyang Chow, Malaysia
J. deClaville Christiansen, Denmark
Yoshiki Chujo, Japan
Angel Concheiro, Spain
Marek Cypryk, Poland
Li Ming Dai, USA
Yulin Deng, USA
Maria Laura Di Lorenzo, Italy
Eliane Espuche, France
Antonio Facchetti, USA
Marta Fernández-García, Spain
Benny Dean Freeman, USA
Jean-François Gérard, France
Peng He, USA
Jan-Chan Huang, USA
Wei Huang, China
Nabil Ibrahim, Egypt
Tadashi Inoue, Japan

Avraam I. Isayev, USA
Koji Ishizu, Japan
Patric Jannasch, Sweden
Nobuhiro Kawatsuki, Japan
J.M. Kenny, Italy
Mubarak A. Khan, Bangladesh
Ruhul A. Khan, Canada
Saad Khan, USA
Jui-Yang Lai, Taiwan
Jose Ramon Leiza, Spain
Guiping Ma, China
Evangelos Manias, USA
Ulrich Maschke, France
Jani Matisons, Australia
Geoffrey R. Mitchell, UK
Subrata Mondal, India
Christian Nielsen, UK
Toribio F. Otero, Spain
Qinmin Pan, Canada
Alessandro Pegoretti, Italy
"Onder Pekcan, Turkey
Zhonghua Peng, USA
Antje Potthast, Austria
Debora Puglia, Italy
Miriam Rafailovich, USA
Arthur J. Ragauskas, USA
Subramaniam Ramesh, Malaysia
Bernabé L. Rivas, Chile
Juan Rodriguez-Hernandez, Spain

Hossein Roghani-Mamaqani, Iran
Pietro Russo, Italy
Mehdi Salami-Kalajahi, Iran
Erol Sancaktar, USA
A. P. H. J. Schenning, Netherlands
Markus Schmid, Germany
Matthias Schnabelrauch, Germany
Shu Seki, Japan
Vitor Sencadas, Australia
Robert A. Shanks, Australia
Mikhail Shtilman, Russia
Basavarajaiah Siddaramaiah, India
Dennis W. Smith Jr., USA
Atsushi Sudo, Japan
Kohji Tashiro, Japan
Hideto Tsuji, Japan
Masaki Tsuji, Japan
Stefano Turri, Italy
Hiroshi Uyama, Japan
Cornelia Vasile, Romania
Alenka Vesel, Slovenia
Yakov S. Vygodskii, Russia
De-Yi Wang, Spain
Qinglin Wu, USA
Frederik Wurm, Germany
Huining Xiao, Canada
Yiqi Yang, USA
Long Yu, Australia
Philippe Zinck, France

Contents

Functional Polymers for Biointerface Engineering

Qiang Wei, Jie He, Weifeng Zhao, and Yin Chen

Volume 2017, Article ID 2474397, 2 pages

Bioinspired Polyethersulfone Membrane Design via Blending with Functional Polyurethane

Mei Han, Qiang Liu, Baihai Su, Shudong Sun, and Changsheng Zhao

Volume 2017, Article ID 2158124, 10 pages

Use of Oxalic-Acid-Modified Stellerite for Improving the Filter Capability of PM_{2.5} of Paper Composed of Bamboo Residues

Hua Chen, Jian Lou, Fei Yang, Jia-nan Zhou, Yan Zhang, and Huabo Yao

Volume 2016, Article ID 2198506, 7 pages

Constructing Functional Ionic Membrane Surface by Electrochemically Mediated Atom Transfer Radical Polymerization

Fen Ran, Dan Li, and Jiayu Wu

Volume 2016, Article ID 3083716, 9 pages

Fish Collagen Promotes the Expression of Genes Related to Osteoblastic Activity

Mark Luigi Fabian Capati, Ayako Nakazono, Kohei Yamamoto, Kouji Sugimoto,

Kajiro Yanagiguchi, Shizuka Yamada, and Yoshihiko Hayashi

Volume 2016, Article ID 5785819, 7 pages

The Influence of Irradiation and Accelerated Aging on the Mechanical and Tribological Properties of the Graphene Oxide/Ultra-High-Molecular-Weight Polyethylene Nanocomposites

Guodong Huang, Zifeng Ni, Guomei Chen, and Yongwu Zhao

Volume 2016, Article ID 2618560, 9 pages

Bottom-Up Fabrication of PEG Brush on Poly(dimethylsiloxane) for Antifouling Surface Construction

Junmei Tang, Yuemei Han, Hao Chen, and Quankui Lin

Volume 2016, Article ID 8458752, 5 pages

Influence of Sodium Alginate on Hypoglycemic Activity of Metformin Hydrochloride in the Microspheres Obtained by the Spray Drying

Marta Szekalska, Magdalena Wróblewska, Katarzyna Sosnowska, and Katarzyna Winnicka

Volume 2016, Article ID 8635408, 12 pages

Editorial

Functional Polymers for Biointerface Engineering

Qiang Wei,¹ Jie He,² Weifeng Zhao,³ and Yin Chen⁴

¹Max Planck Institute for Medical Research, Stuttgart, Germany

²University of Connecticut, Storrs, CT, USA

³Sichuan University, Chengdu, China

⁴The Hong Kong University of Science and Technology, Hong Kong, China

Correspondence should be addressed to Qiang Wei; wei@is.mpg.de, Jie He; jie.he@uconn.edu, Weifeng Zhao; weifeng@kth.se, and Yin Chen; yinchen@ust.hk

Received 2 January 2017; Accepted 4 January 2017; Published 28 February 2017

Copyright © 2017 Qiang Wei et al. This is an open access article distributed under the Creative Commons Attribution License, which permits unrestricted use, distribution, and reproduction in any medium, provided the original work is properly cited.

Biomaterials and biomedical devices can induce a set of adverse biological responses upon contact with body fluids and/or implantation into living organs, as a result of the formation of biointerfaces between biomolecules and surfaces. Functional polymers have been of great interest because of their promising properties for improving the biocompatibility of the materials and mimicking the biological systems to stimulate/interact with cells. Given the great potential of polymers in solving problems at biointerfaces and the growing demands in their biomedical applications, we launched this special issue, which includes seven research articles, to illustrate the applications of functional polymers in engineering biointerfaces between biological systems and polymeric materials and preparing novel biomaterials with desired surface characters.

Surface modification of solid materials is a key to generating artificial biointerface. When bioinert and/or bioactive polymers are immobilized on the surface of biomaterials and biomedical devices via modern fabrication technologies, newly resulting biointerfaces exhibit versatile biological effects, including antifouling, anticoagulation, specific adhesion, and tissue regeneration [1]. The strategies of generating polymeric surfaces include “grafting from,” “grafting to,” and “blending” techniques. The article “Bottom-Up Fabrication of PEG Brush on Poly(dimethylsiloxane) for Antifouling Surface Construction” and the article “Constructing Functional Ionic Membrane Surface by Electrochemically Mediated Atom Transfer Radical Polymerization” show the “grafting from” technique via surface-initiated reversible

addition-fragmentation chain transfer (SI-RAFT) polymerization and surface-initiated atom transfer radical polymerization (SI-ATRP), respectively. The “grafting to” technique was utilized in the article “Use of Oxalic-Acid-Modified Stellerite for Improving the Filter Capability of PM_{2.5} of Paper Composed of Bamboo Residues” to immobilize oxalic acid and cationic starch on the surface of stellerites and to further stabilize the modified stellerites on the paper sheets. As an alternative way, the surface of ultrafiltration membrane was modified by simply blending polyurethane in the article “Bio-Inspired Polyethersulfone Membrane Design via Blending with Functional Polyurethane.” As such, the biocompatibility, hemocompatibility, and specific filtration ability of the materials were improved, which were highly required to meet the growing demands of the biomedical applications. Besides the traditional specific surface coatings shown above, materials-independent universal polymer coatings are increasing needed because of the fast development and diversification in materials science. The general rules were proposed to develop this type of coatings [2]: (1) there must be appropriate interactions between the coating polymers and the substrates; (2) intracoating crosslinking is required to stabilize the polymer coatings; (3) the coatings should present available functions or reactive functionalities for further functionalization.

The scale size of the polymeric materials also results in versatile effects at biointerfaces, for example, benefiting the rapid responses to external stimuli [3]. Thanks to the rapid development of nanotechnology, the polymers in

microscale and nanoscale have been extensively studied. The advantages of nanomaterials/macromaterials are often due to the high surface/volume ratios. Generally, the construction of a nanoscale or microscale system requires synthesis or fabrication of scalable polymers, suitable devices, and so on. For example, the article “Influence of Sodium Alginate on Hypoglycemic Activity of Metformin Hydrochloride in the Microspheres Obtained by the Spray Drying” employed spray drying approach towards fabricating soft microgels for metformin hydrochloride delivery, which could improve the lipid profile in human body with no risk of hypoglycemia. By incorporating Fe_3O_4 nanoparticles into polysaccharide hydrogels, the soft drug controlled delivery system could be achieved by magnetic field stimuli [4]. For repairing hard tissues, the article “The Influence of Irradiation and Accelerated Aging on the Mechanical and Tribological Properties of the Graphene Oxide/Ultra-High-Molecular-Weight Polyethylene Nanocomposites” introduces nano-size graphene oxide into widely used ultra-high-molecular-weight polyethylene for improvement of mechanical properties of artificial joints. Generally, high repairing efficiency, low toxicity, and good tolerance should be taken into consideration during use of nanoscale/microscale polymers in biomedical applications [5].

Natural biopolymers are macromolecules derived from biological systems, such as DNA, protein, and polysaccharide. They have been extensively used as biomaterials for drug delivery, disease diagnosis, wound dressing, and tissue engineering as a result of their good biocompatibility and programmable biodegradability [6] or even directly as biospecific stimulants for tuning cell behaviors via the surface receptors of cells and tissues. In the article “Fish Collagen Promotes the Expression of Genes Related to Osteoblastic Activity,” fish collagen was demonstrated to promote the differentiation and maturation of a preosteoblast cell line (MC3T3-E1).

In summary, this special issue bridges the polymer science and the biointerface engineering. We sincerely hope that the readers enjoy reading the presented original research work in this special issue and they can get inspired for their future studies.

Acknowledgments

We appreciate the great effort and the kind contributions from the authors, reviewers, and the editorial staff members to this special issue.

Qiang Wei
Jie He
Weifeng Zhao
Yin Chen

References

- [1] Q. Wei, T. Becherer, S. Angioletti-Uberti et al., “Protein interactions with polymer coatings and biomaterials,” *Angewandte Chemie—International Edition*, vol. 53, no. 31, pp. 8004–8031, 2014.
- [2] Q. Wei and R. Haag, “Universal polymer coatings and their representative biomedical applications,” *Materials Horizons*, vol. 2, no. 6, pp. 567–577, 2015.
- [3] W. Zhao, R. W. N. Nugroho, K. Odelius, U. Edlund, C. Zhao, and A.-C. Albertsson, “In situ cross-linking of stimuli-responsive hemicellulose microgels during spray drying,” *ACS Applied Materials & Interfaces*, vol. 7, no. 7, pp. 4202–4215, 2015.
- [4] W. Zhao, K. Odelius, U. Edlund, C. Zhao, and A.-C. Albertsson, “In situ synthesis of magnetic field-responsive hemicellulose hydrogels for drug delivery,” *Biomacromolecules*, vol. 16, no. 8, pp. 2522–2528, 2015.
- [5] H. Malhaire, J.-C. Gimel, E. Roger, J.-P. Benoit, and F. Lagarce, “How to design the surface of peptide-loaded nanoparticles for efficient oral bioavailability?” *Advanced Drug Delivery Reviews*, vol. 106, pp. 320–336, 2016.
- [6] S. Van Vlierberghe, P. Dubruel, and E. Schacht, “Biopolymer-based hydrogels as scaffolds for tissue engineering applications: a review,” *Biomacromolecules*, vol. 12, no. 5, pp. 1387–1408, 2011.

Research Article

Bioinspired Polyethersulfone Membrane Design via Blending with Functional Polyurethane

Mei Han,^{1,2} Qiang Liu,^{1,2} Baihai Su,^{1,2} Shudong Sun,¹ and Changsheng Zhao¹

¹College of Polymer Science and Engineering, State Key Laboratory of Polymer Materials Engineering, Sichuan University, Chengdu 610065, China

²Department of Nephrology, West China Hospital, Sichuan University, Chengdu 610041, China

Correspondence should be addressed to Baihai Su; subaihai@scu.edu.cn and Changsheng Zhao; zhaochsh70@163.com

Received 1 October 2016; Revised 28 November 2016; Accepted 27 December 2016; Published 13 February 2017

Academic Editor: Yin Chen

Copyright © 2017 Mei Han et al. This is an open access article distributed under the Creative Commons Attribution License, which permits unrestricted use, distribution, and reproduction in any medium, provided the original work is properly cited.

Polyurethanes (PUs) are currently considered to be biocompatible materials but limited by a low resistance to thrombus. We therefore design a heparin-like PU (HLPU) to modify polyethersulfone (PES) membranes approaching integrated antifouling and antithrombotic properties by bioinspiration of heparin structure. Poly(vinyl pyrrolidone)-HLPU (PVP-HLPU) was synthesized via reversible addition-fragmentation chain transfer polymerization of VP using PU as a macroinitiator and then sulfonated by concentrated H₂SO₄. FTIR and NMR results demonstrated the successful synthesis of PVP-HLPU. By incorporation of PVP-HLPU, the cross-sectional structure of PES composite membranes altered from finger-like structure to sponge-like structure resulting in tunable permeability. The increased hydrophilicity verified by water contact angles benefited both the permeability and antifouling property. As a consequence, the composite membranes showed good blood compatibility, including decreased protein adsorption, suppressed platelet adhesion, lowered thrombin-antithrombin III generation, reduced complement activation, and prolonged clotting times. Interestingly, the PVP-capped HLPU showed better blood compatibility compared to polyethyleneglycol-capped and citric acid-capped HLPUs. The results demonstrated the enhanced antifouling and antithrombotic properties of PES hemodialysis membranes by the introduction of functional HLPUs. Also, the proposed method may forward the fabrication of hemocompatible membranes via bioinspired surface design.

1. Introduction

Polyurethanes (PUs) are currently facing growing applications in biomedical fields such as bone regeneration [1], near-infrared imaging [2], shape memory [3], anti-inflammatory platform [4], cancer gene therapy [5], controlled drug delivery [6], tissue engineering [7], and nervous system repair [8], due to the main advantage of their flexible chemical structure. Simple alterations of stoichiometry and/or monomers during the synthesis of PUs can produce various materials ranging from elastic thermoplastic polymers to rigid thermoset ones [9]. Besides these, a facile modification of pendent groups of PU can result in a broad spectrum of properties ranging from removing toxin bilirubin to antibacterial properties [10]. However, a limitation of low resistance to thrombi is still associated with these biomaterials that restricted their uses as blood-contacting materials.

Heparin is a highly acidic, polyanionic, and dispersive linear polysaccharide [11]. The bearing of highly negative charged groups (sulfate and carboxylate groups) and the acceptably hydrophilic structure facilitate its anticoagulant property, leading to a wide use in clinical practice. Therefore, numerous approaches have been developed to prepare heparin-immobilized PUs for potential biomedical applications with improved biocompatibility and anticoagulant activity [12], enhanced antiadhesive and antibacterial properties [13], inhibited protein and platelet adhesion [14], enhanced viability of transplanted hepatocytes and inducing angiogenesis [15], and so on. In an earlier study, blood-contacting PU films were prepared by alternatively immersing PU films in human serum albumin and heparin solutions [16]. However, the physically coated heparin onto PUs is not stable with the ionic interaction between human serum albumin (HSA) and heparin. Thereafter, researches turn

the direction towards covalently immobilization of heparin onto PUs. Tan et al. covalently linked heparin onto PU surfaces by the reaction between the amino group from pregrafted polyethylenimine and the carboxyl group from heparin, which significantly improved the hydrophilicity and hemocompatibility of the materials [12]. However, fabricating a heparin-like structure in PU polymer chains is rarely targeted. Herein, we aim to design novel heparin-like PU (HLPU) for the modification of polyethersulfone (PES) membrane by a simple blending method, which may be used for the fabrication of hollow dialysis membranes.

PES has become one of widely used polymers, due to its good oxidative, thermal and hydrolytic stabilities, and good mechanical and film-forming properties [17, 18]. However, the anticoagulant and antifouling properties of PES are not ideal so far. Therefore, our recent study focused on the functionalization of PES dialysis membranes by HLPUs. The heparin-like polyurethanes contained $-SO_3H$, $-COOH$, and $-OH$ groups, which were fabricated to modify the anticoagulate property of PES membranes by a blending method [19]. In order to endow PES membrane with both anticoagulant and antifouling properties, herein, poly(vinyl pyrrolidone) (PVP) is employed as an end-capped groups in HLPU. The resultant PVP-HLPU was then blended with PES. The water contact angle, antifouling property, and hemocompatibility for the membranes were performed. In addition, the effect of the end-capped groups on the properties of modified PES membranes was studied.

2. Experimental

2.1. Materials. Polyethersulfone (PES, Ultrason E6020P) was purchased from BASF chemical company (Germany). *N*-Vinyl-pyrrolidone (VP; 99%) was purchased from Alfa Aesar. Diphenyl-methane-diisocyanate (MDI; 98%) and dimethylolpropionic acid (DMPA; 98%) were obtained from Aladdin (China). MDI, DMAP, VP, and DMAc were distilled under reduced pressure prior to use. *N,N*-dimethylacetamide (DMAc; 98%) was obtained from Chengdu Kelong Company (China). Bovine serum albumin (BSA) and bovine serum fibrinogen (FBG) were purchased from Sigma (USA). All the other chemicals were obtained from Chengdu Kelong Inc., China.

2.2. Synthesis and Characterization of PVP-HLPU. PU was firstly synthesized. Typically, 0.060 mol MDI was dissolved in 200 mL DMAc with stirring under N_2 , followed by adding 0.062 mol DMPA. After completely dissolving the monomers, the reaction was performed in airtight equipment at 70°C for 4 h under N_2 . The reaction pathway is presented in Scheme 1. The crude product was purified by methanol and hot deionized (DI) water, respectively, to remove the residues. The obtained PU was dried completely at 40°C in a vacuum oven over 3 days.

Then, PU RAFT agent was synthesized. Typically, 1.74 g chain transfer agent (CTA), 1.18 g EDC, and 0.83 g HOBT were dissolved in 200 mL DMAc with continuous stirring at nitrogen atmosphere. After the activation for 1 h, 18 g PU was added to above-mentioned solution and kept the reaction at

TABLE 1: The compositions of modified PES membranes.

Sample code	PES (wt.%)	PVP-HLPU (wt.%)	DMAc (wt.%)
M-0	18	0	72
M-2	18	2	70
M-4	18	4	68
M-6	18	6	66
M-8	18	8	64

room temperature for 24 h. The product was purified with methanol and hot DI water, respectively, to guarantee a full removal of the impurities. The obtained product (macro-RAFT agent) was dried completely at 30°C in a vacuum oven until reaching constant weight.

Polymerization of VP into the polymer chain of PU was carried out in a sealed tube. Briefly, 2.49 g of VP, 1 g of the macro-RAFT agent, and 0.02 g of AIBN were added to a Schlenk flask followed by the addition of DMAc. After three cycles of freeze-pump-thaw, the reaction mixture was allowed to warm to 80°C under a nitrogen atmosphere, and the polymerization was carried out for 10.5 h. After dialysis against DI water for couple of days, the product was freeze-dried resulting in white powders and termed as PVP-PU.

The obtained PVP-PU was sulfonated by concentrated H_2SO_4 with a mass ratio of 1:10. After stirring at room temperature in the H_2SO_4 for 10 h, the PVP-HLPU was purified with DI water for couple of times to remove the residue H_2SO_4 . The HLPU powder was dried at 30°C for 72 h. A Fourier transform infrared spectroscope (FTIR) and a BRUKER spectrometer were used to characterize PVP-HLPU polymer.

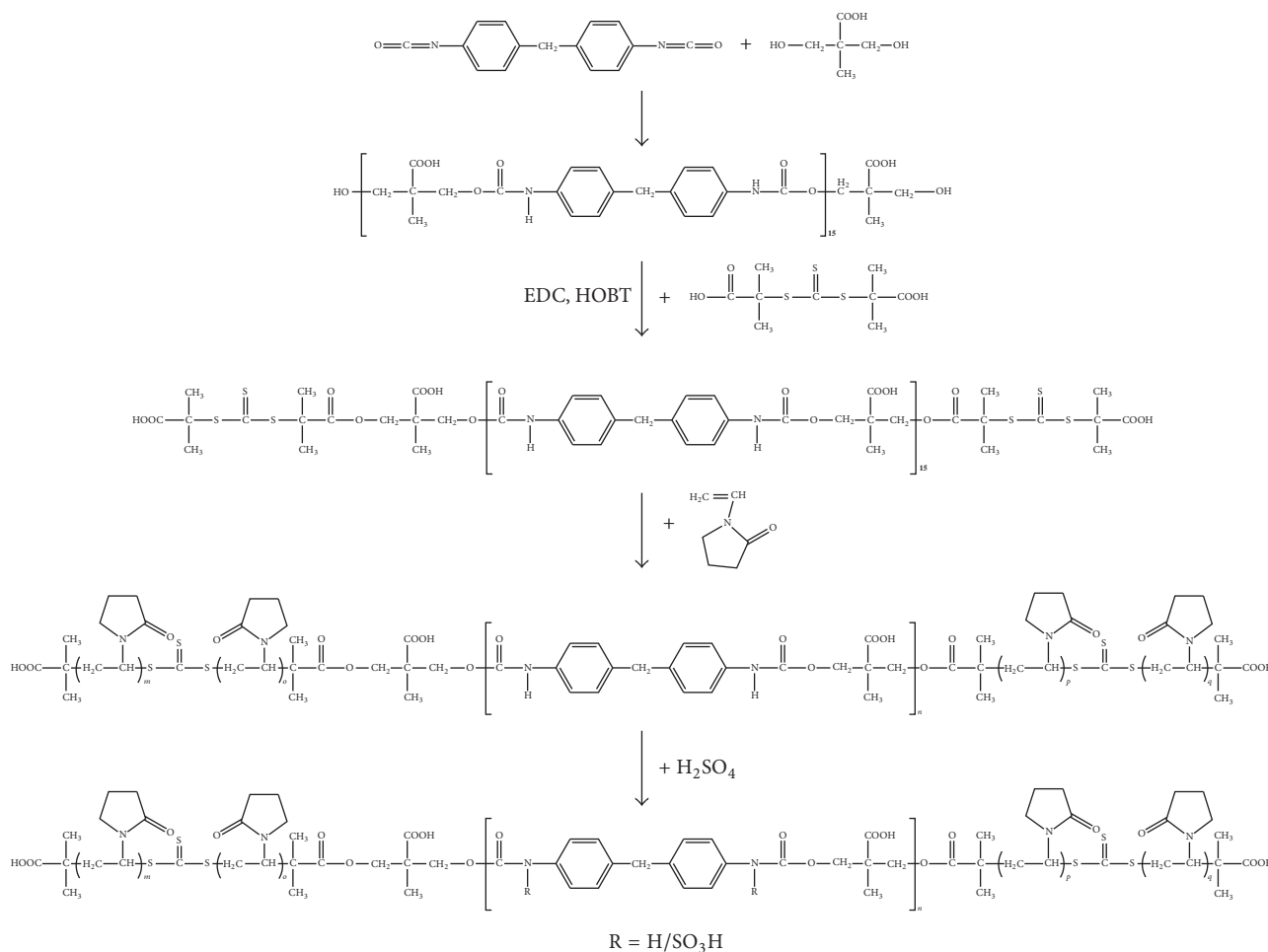
2.3. Preparation and Characterization of Membranes. The membranes were prepared by a liquid-liquid phase-inversion technique as described in our earlier studies [20]. The modified membranes with different mass percentages of the PVP-HLPU are shown in Table 1.

A scanning electron microscope (FE-SEM, JSM-7500F, JEOL, Japan) was used to characterize the cross section morphology of the membranes.

The hydrophilicity of the membranes was characterized by a contact angle goniometer (OCA20, Dataphysics, Germany) equipped with video capture. At least five measurements were averaged to reach a reliable value.

2.4. Antifouling Property of Membranes. The characterization of the antifouling property of membranes were provided in S1 (see Supporting Material available online at <https://doi.org/10.1155/2017/2158124>).

2.5. Blood Compatibility of Membranes. The protein adsorption behavior of PES membranes was carried out according to our previous study [10]. The protein adsorption, platelet adhesion, clotting times (activated partial thromboplastin times (APTTs) and thrombin times (TTs)), platelet activation (Human Platelet Factor 4 (PF4)), coagulation activation (thrombin-antithrombin III complex (TAT)), and complement activation (C3a and C5a) of PES membranes were



SCHEME 1: Synthesis of PVP-HLPU.

carried out, and the details were provided in S2 (see Supplementary Material).

3. Results and Discussion

3.1. Synthesis and Characterization of HLPV. The FTIR spectra for the PVP-PU and PVP-HLPU are shown in Figure 1. It was observed that the peaks at 3310 cm⁻¹ and 3391 cm⁻¹ were the characteristic stretching vibration peaks of the N-H of the isocyanate [19] in the PVP-PU and PVP-HLPU, respectively. After the sulfonation, the peak intensity at 3310 cm⁻¹ decreased, which indicated the successful sulfonation of PVP-PU. The peaks at 2914 cm⁻¹ and 2908 cm⁻¹ were attributed to the -CH₃ of the CTA in the PVP-PU and PVP-HLPU, respectively, while the peaks at 1732 and 1736 cm⁻¹ were attributed to the -C=O in the carboxyl group of the isocyanate in both the PVP-PU and PVP-HLPU. The characteristic stretching vibration peak of cyclanone in VP was observed at 1662 cm⁻¹. Besides, the characteristic peak of S=O of the sulfonate group in PVP-HLPU should be between 1600 and 1750 cm⁻¹, which was covered by the characteristic peak of C=O.

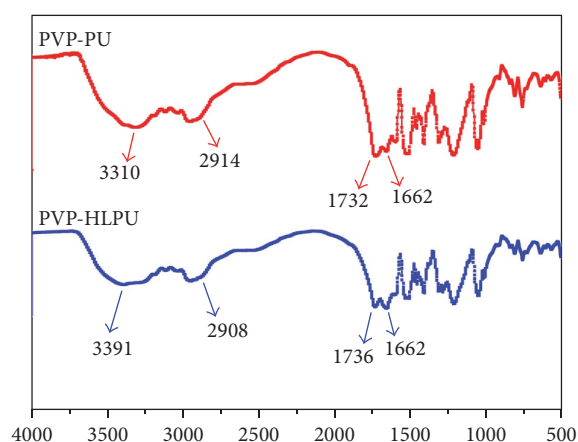


FIGURE 1: FTIR spectra of PVP-PU and PVP-HLPU.

The NMR spectra for the PVP-PU and PVP-HLPU are presented in Figure 2. The synthesized PVP-PU was verified by the signals at a ($\delta = 9.59$ ppm, N-H), b and c ($\delta = 7-7.5$ ppm, Ar-H), d ($\delta = 4.22$ ppm, -CH₂- in DMPA), e

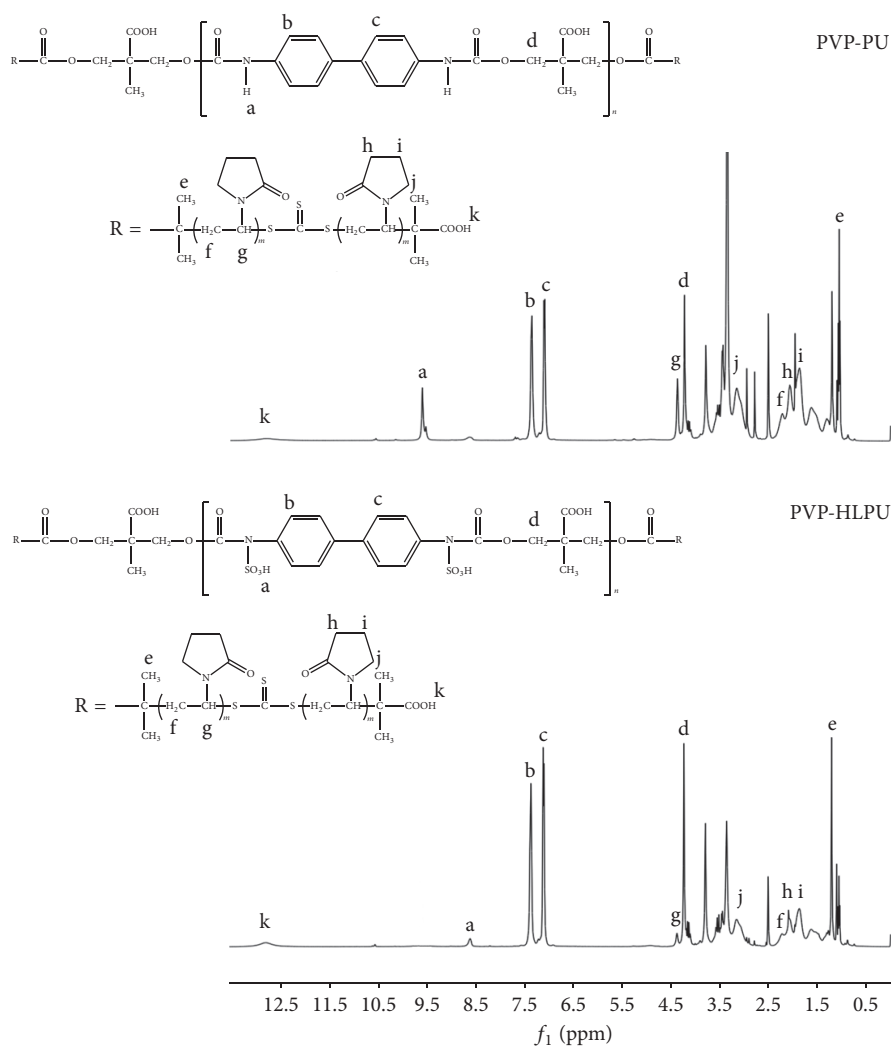


FIGURE 2: The ^1H NMR of PVP-PU and PVP-HLPU.

($\delta = 1.21$ ppm, $-\text{CH}_3$ of the CTA), f ($-\text{CH}_2-$ on the PVP backbone), g (C-H on the PVP backbone), h, i, and j (the $-\text{CH}_2-$ of the cyclanone in VP), and k ($-\text{COOH}$ of the PVP-PU). Compared to the NMR spectrum for the PVP-PU, the signal at $\delta = 9.59$ ppm (N-H) of the NMR spectrum for the PVP-HLPU almost disappeared, which was replaced with an intensified signal at $\delta = 8.53$ ppm due to the sulfonic group in PVP-HLPU).

3.2. Morphologies and Hydrophilicity of PES Membranes. Figure 3 shows the SEM images for the cross section of the membranes. It was observed that the cross section structure of the membranes showed two dense layers and an interlayer. Interestingly, the pores of the modified membranes changed gradually from finger-like structure to sponge-like structure with the addition of the PVP-HLPU, when compared to the membrane M-0. Especially when the PVP-HLPU content reached 8 wt.% (M-8), the finger-like pores almost disappeared and the cross-sectional structure nearly changed to sponge-like structure. Furthermore, the sponge-like pore size

increased gradually with the PVP-HLPU content changing from 2 wt.% to 8 wt.%; the reason might be that the hydrophilic PVP-HLPU migrated to the membrane surfaces and the pore surfaces during the phase separation process of the membrane preparation [17].

3.3. Antifouling Property of Membranes. To investigate the antifouling property of the membranes, BSA ultrafiltration was carried out, and the data are shown in Figure 4. The PBS fluxes of all the modified membranes were higher than that of the pristine PES membrane. For the modified membranes, the PBS flux increased with increasing the HLPU amount, which might be resulted from the changed membrane structure and the increased surface hydrophilicity (as shown in Figure 3 and Table 2). It was reported that the viscosity of the casting solution would be changed after blending the amphiphilic PU, which had great effect on the phase separation during membrane formation [21].

Meanwhile, a slight reduction in the PBS solution was observed with time as shown in Figure 4. The fluxes of

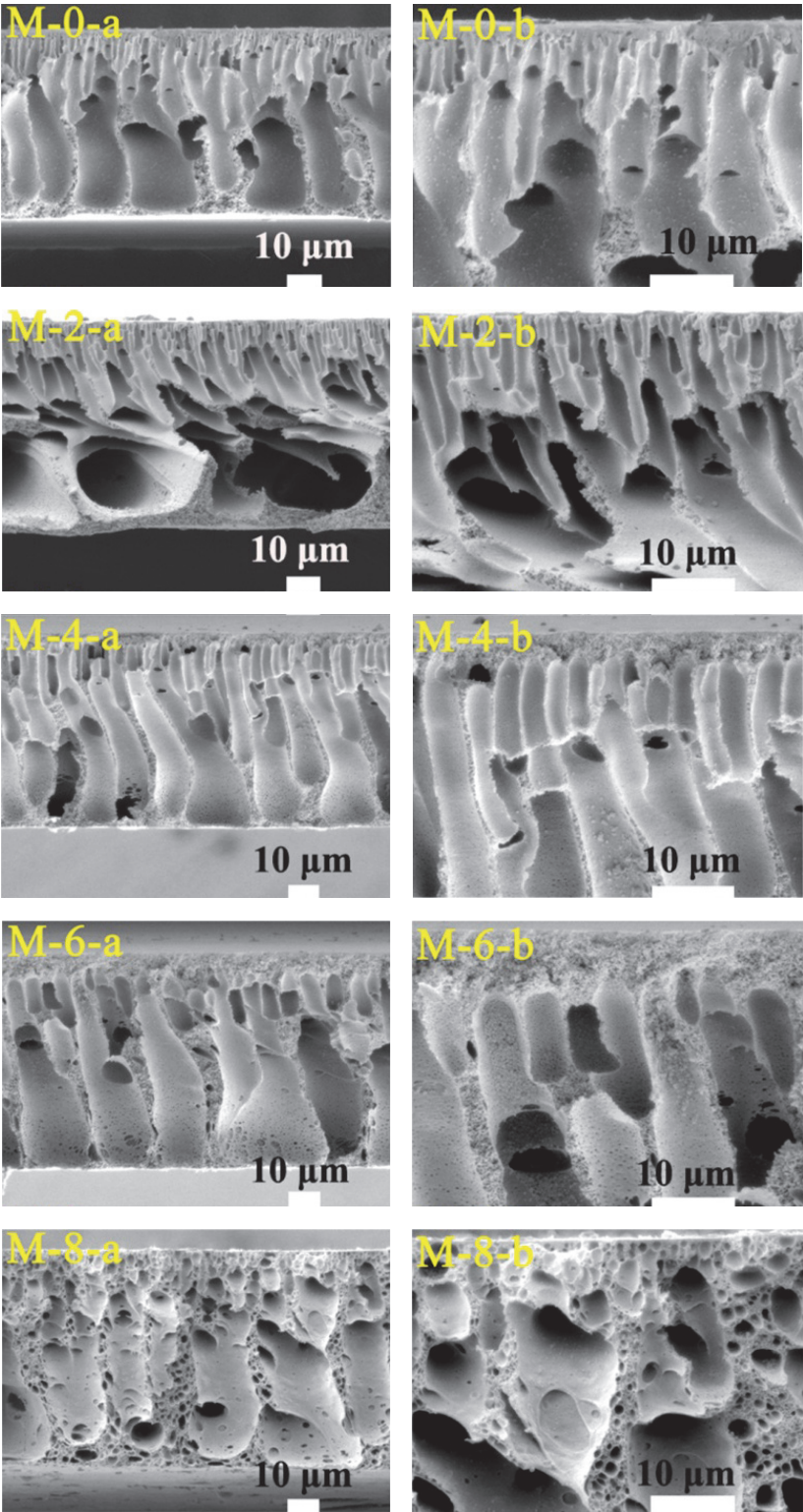


FIGURE 3: SEM images of the cross sections of different PES membranes. Magnification: (a) 1000x; and (b) 2500x.

TABLE 2: Water contact angle and permeability of PES membranes.

Sample code	Copolymer (wt. %)	Water contact angle ($^{\circ}$)	Water flux ($\text{mL/h}\times\text{m}^2\times\text{mmHg}$)	Flux recovery ratio (%)
M-0	0.0	76.8 ± 2.2	30.6	40.8
M-2	2.0	65.8 ± 1.9	90.0	81.7
M-4	4.0	58.2 ± 1.5	113.6	84.7
M-6	6.0	51.3 ± 1.8	133.5	88.2
M-8	8.0	46.7 ± 2.5	155.1	92.0

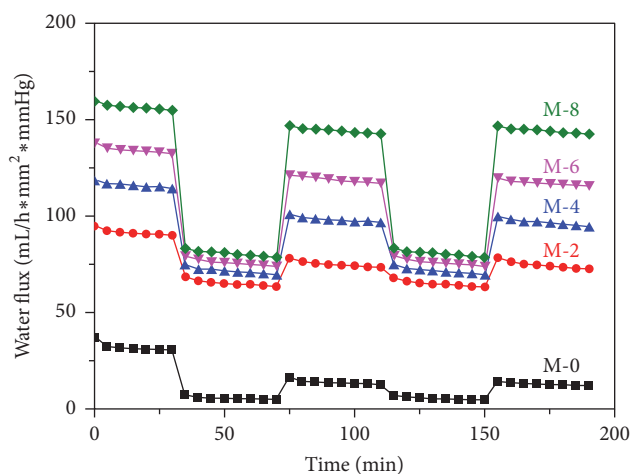


FIGURE 4: Time-dependent fluxes of the PES and modified membranes. PBS solution: 0–30 min, 80–110 min, and 160–190 min; BSA solution: 40–70 min and 120–150 min.

the membranes decreased dramatically when the filtration solution changed from PBS to BSA solution. This might be due to BSA molecules deposition/adsorption on the membrane surfaces and/or in the membrane pore surfaces [22].

The decline in flux under constant pressure was caused by two reasons: concentration polarization and membrane fouling [23]. As a result, several cycles of filtration and flux recovery ratios were tested to determine the main reason for the flux decline of the membranes. The composite membranes were washed with PBS solution for 10 min after 60 min of protein ultrafiltration. Afterward, the PBS solution fluxes were carried out once again. It could be observed in Figure 4 that the fluxes for all the modified membranes recovered in a larger extent compared to the pristine PES membrane after rinsing in DI water for 30 min. It indicated that the fluxes of the modified membranes were much easier to be recovered and thus showed better antifouling property.

In addition, flux recovery ratios (F_{RR}) were used to judge the antifouling property [24]. The better antifouling property of the membrane is reflected by higher F_{RR} values. As shown in Table 2, all F_{RR} values for the modified membranes were over 80%, which are higher than that (40.8%) of the pristine PES one. In addition, F_{RR} increased gradually with increasing blended amounts of HLPUs. It indicated that the composite membranes showed good antifouling property after the addition of HLPUs.

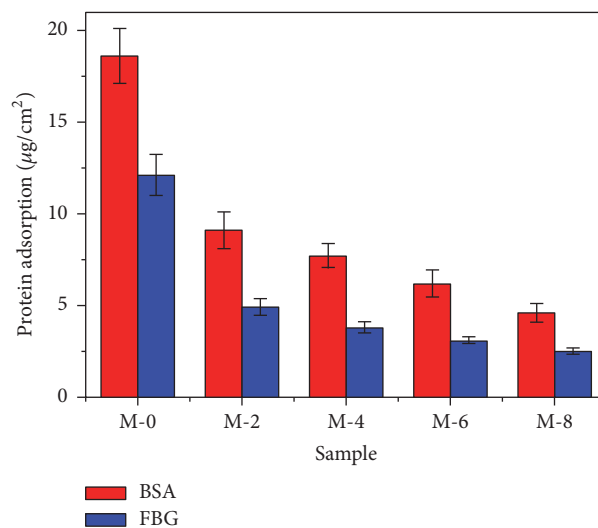


FIGURE 5: The protein adsorbed amount for the pure PES membrane and the composite membranes.

3.4. Blood Compatibility of Membranes

3.4.1. Protein Adsorption. Protein adsorption on biomaterial surfaces is always considered as the first step of many undesired bioreactions and bioresponses [25]. Protein adsorption is affected by numerous factors, such as hydrophilicity/hydrophobicity, surface charge, surface topology, interactions between the adsorbed molecules, the composition of the protein solution, and the surface chemistry [26]. The modified membranes after blending with hydrophilic additives exhibited decreased protein adsorption and enhanced biocompatibility [22]. Otherwise, plasma protein adsorbed on material surface had great influence on platelet adhesion and activation [27]. Thus, protein adsorption was firstly tested to investigate the blood compatibility of the membranes.

The adsorption of BSA and FBG of the membranes was studied in vitro, and the results are presented in Figure 5. As expected, all the modified membranes exhibited decreased protein adsorption amounts compared to the pristine PES membrane (M-0). The BSA adsorption and FBG adsorption for the pristine PES membrane were $18.5 \mu\text{g}/\text{cm}^2$ and $11.8 \mu\text{g}/\text{cm}^2$, respectively. As for the modified membranes, the protein adsorption amounts decreased with increasing the blended HLPUs content. In particular, when the PVP-HLPUs content was 8 wt.%, the BSA and FBG adsorption of the membrane (M-8) decreased dramatically to $4.9 \mu\text{g}/\text{cm}^2$ and $2.4 \mu\text{g}/\text{cm}^2$, respectively. It might be caused by the

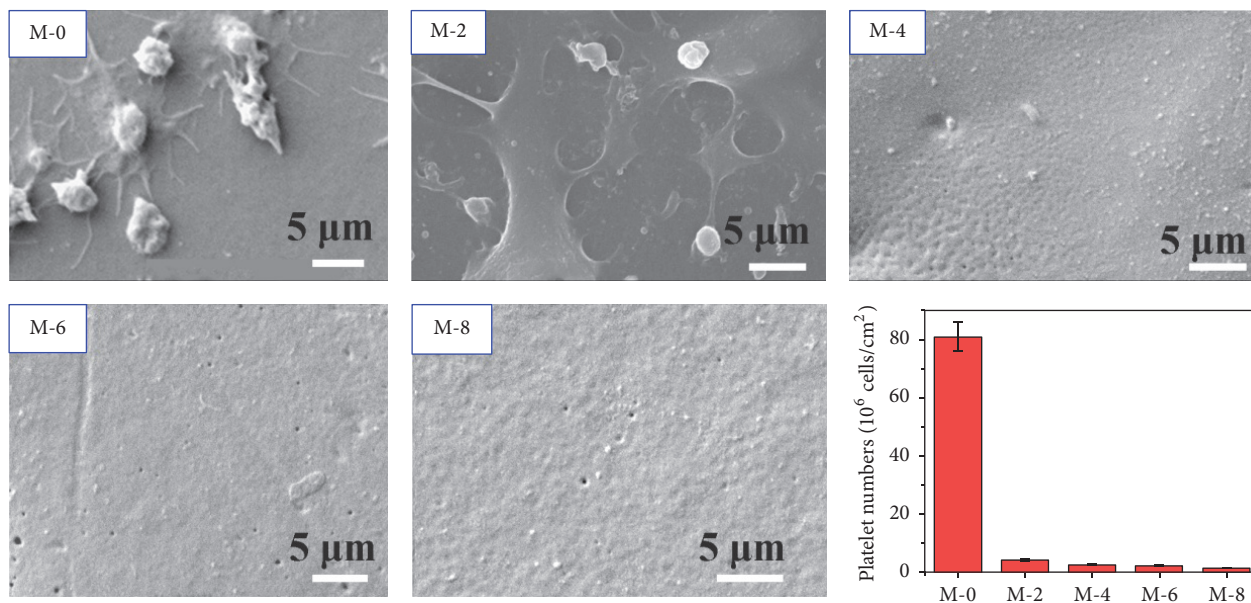


FIGURE 6: SEM micrographs of platelets adhered on the membrane surface.

increased hydrophilicity and electrostatic repulsion of the negative charge of the modified membrane surface. The enhanced protein antifouling properties improved the blood compatibility of the modified membranes.

3.4.2. Platelet Adhesion. Platelet adhesion on the surface of biomaterials is also critical to evaluate hemocompatibility. Once a foreign material contacts with blood, inducing of adsorbing proteins in blood, platelet adhesion and platelet activation cannot be avoided, then forming thrombus [28].

The results of platelet adhesion onto PES membranes are presented in Figure 6. It could be observed that the amount of adhering platelets decreased sharply with increasing the PVP-HLPU amounts in the modified membranes. When the PVP-HLPU content reached above 6 wt.% (M-6 and M-8), there was almost no platelet adhesion on the modified membranes. Meanwhile, the adhered platelets on the surface of modified membranes showed rounded shape, and almost no pseudopodium and deformation were observed on the surface of the modified membrane. However, an aggregation of the adhered platelets on the original PES membrane were deformed with extended pseudopodia. It was due to the improved hydrophilicity and the relatively low protein adsorption on the modified membranes. It indicated that the hemocompatibility of the PVP-HLPU modified membranes was improved.

3.4.3. Clotting Times (APTT and TT). The activated partial thromboplastin time (APTT) and thrombin time (TT) are also used to characterize the anticoagulant properties of the membranes. We measured the APTTs and TTs for the membranes to investigate the anticoagulation activity of the membranes, and the results are presented in Figure 7.

Both the APTTs and TTs increased sharply with increasing the blended PVP-HLPU amounts. When the blended

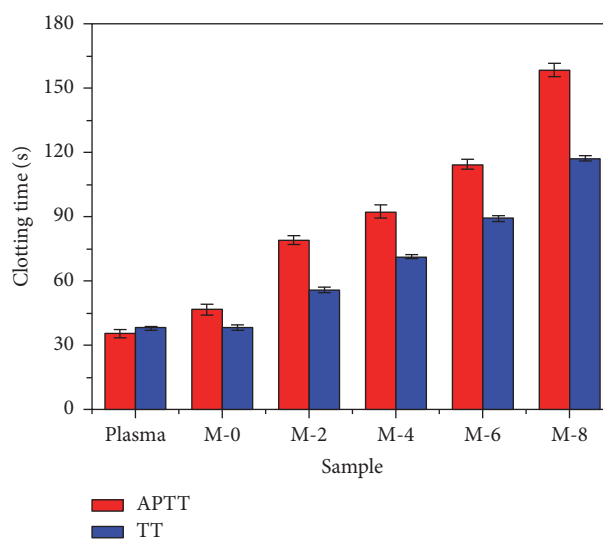


FIGURE 7: Clotting time results for all the membranes. Values are expressed as means \pm SD ($n = 3$).

amounts of PVP-HLPU reached 8 wt.%, both the APTT and TT of the membrane M-8 were over three times longer than the APTT and TT of the membrane M-0. The increase of clotting time was much higher than those reported in other studies [29]. The excellent anticoagulant property was caused by the heparin-mimicking structure of HLPU, the enhanced hydrophilicity, and antifouling properties. Therefore, the clotting time tests indicated the anticoagulant properties of the PVP-HLPU modified membranes were improved.

3.4.4. Platelet Activation and Thrombin Generation. Contact activation of the coagulation system is crucial to induce blood coagulation. Platelet activation could result in platelet

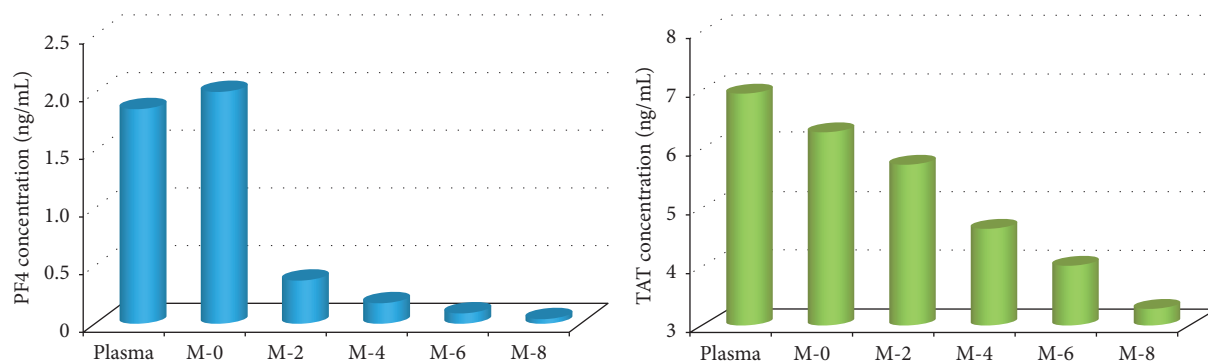


FIGURE 8: Platelet factor 4 (PF4) and thrombin-antithrombin III (TAT III) complex concentrations for the membranes.

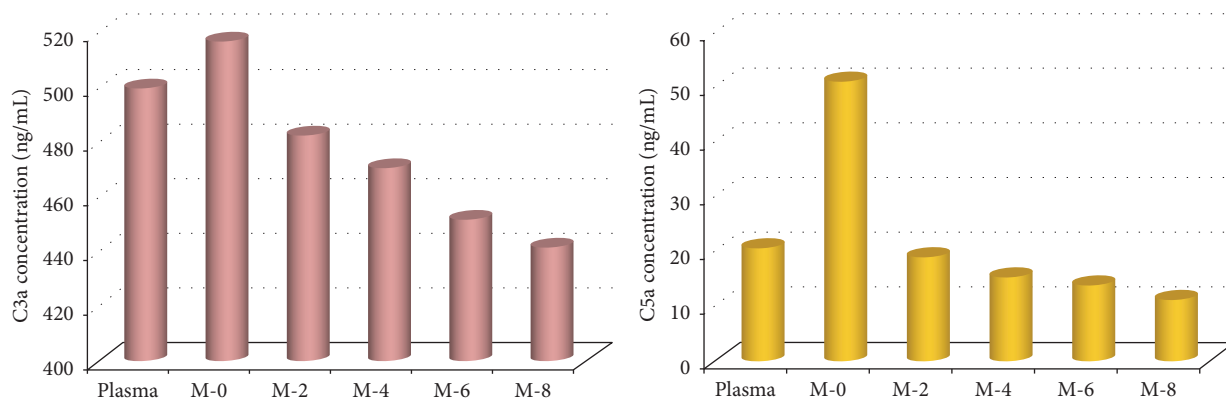


FIGURE 9: C3a and C5a concentrations for the membranes.

aggregation and activate the coagulation cascade system. Platelets interact with coagulation factors, while formed thrombin is a potent platelet-activating agonist [30]. The activated platelets could result in forming platelet factor 4 (PF4), while the formed thrombin could couple with antithrombin III to generate thrombin-antithrombin III (TAT) complexes [31]. Therefore, the concentrations of PF4 and TAT complexes could reflect the contact activation level, and the results are presented in Figure 8.

Both the PF4 and TAT complexes concentrations for the modified membranes decreased dramatically compared to the pristine PES membrane (M-0) or the plasma, which indicated that the modified membranes would not induce the activation of platelet and coagulation cascade. Thus, the modified membranes showed excellent blood compatibility after introducing the PVP-HLPU.

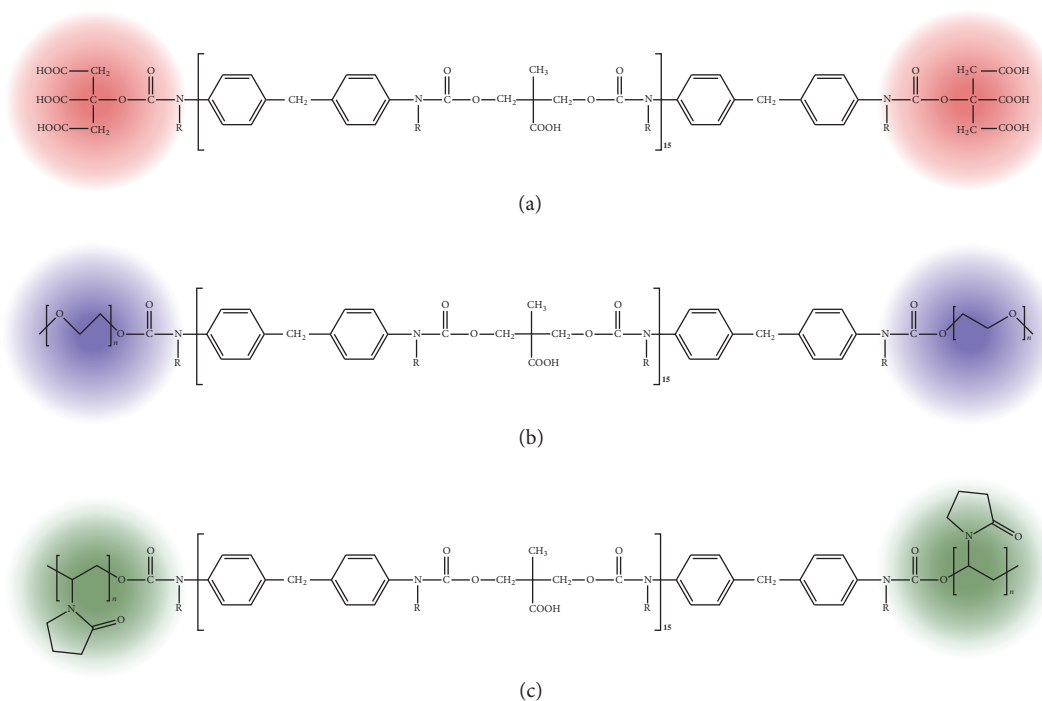
3.4.5. Complement Activation. Human complement system is also important in the body's defense mechanisms against infection and "nonself" elements [32]. After contacting the blood, the complement activation reflects the hemocompatibility of materials. After complement activation, followed by C3a, C4a, and C5a release, which are anaphylatoxins [33]. In current study, activation of C3a and C5a was tested to evaluate the complement activation of the modified membranes, and the results are presented in Figure 9.

Both the C3a and the C5a concentrations in plasma increased after the membrane M-0 contacted with the

plasma. However, for the modified membranes, the C3a and the C5a concentrations in plasma decreased to a certain extent. In addition, their concentrations decreased with increasing the amount of PVP-HLPU additive. The results indicated that the modified membranes showed suppressed complement activation after introducing the PVP-HLPU.

3.4.6. Comparison of End-Capped Hydrophilic Segments. In order to study the influence of the HLPUs with different end-capped hydrophilic segments on membrane performances, CA- and PEG-capped HLPUs were also synthesized and used for the modification of PES membranes. The molecular structures of the HLPUs are illustrated in Scheme 2.

In the study, 8 wt.% of CA-, PEG-, and PVP-capped HLPUs were blended with 18 wt.% of PES, and the membranes were fabricated by a phase-inversion method and termed as M-CA-HLPU, M-PEG-HLPU, and M-PVP-HLPU, respectively. Pure PES membrane was also prepared as the reference and named as M-PES. The properties of PES membranes are listed in Table 3. The hydrophilicity, water flux, and F_{RR} of modified PES membranes increased after blending functional HLPUs. The PES composite membranes with PEG-capped HLPU exhibited lowest protein adsorption compared with those with other functional HLPUs. PVP-capped HLPU could endow PES membranes (M-PVP-HLPU) with the best blood compatibility, which was demonstrated by the highest APTT and TT and the lowest platelet activation, TAT generation, and complement activation.



SCHEME 2: Molecular structures of HLPUs with different end-capped segments.

TABLE 3: Systematical comparison of different HLPUs modified membranes.

Testing Name	Plasma	M-PES	M-CA-HLPU	M-PEG-HLPU	M-PVP-HLPU
Contact angle (°)	/	81.5	54.3	51.2	46.7
Water flux (mL/h*m ² *mmHg)	/	30.6	165.2	175.5	155.1
F_{RR} (%)	/	40.8	95.3	95.3	92.0
BSA adsorption ($\mu\text{g}/\text{cm}^2$)	/	18.6	3.8	3.3	4.6
FBG adsorption ($\mu\text{g}/\text{cm}^2$)	/	12.1	2.7	1.6	2.5
APTT (s)	35.5	46.8	136.2	100.2	158.7
TT (s)	37.9	38.5	108.7	88.5	117.5
PF4 concentration (ng/mL)	1.86	2.01	0.06	1.05	0.04
TAT concentration (ng/mL)	6.95	6.29	5.05	4.86	3.29
C3a concentration (ng/mL)	499.7	516.8	482.5	456.1	441.6
C5a concentration (ng/mL)	20.6	51.1	16.9	13.9	11.2

4. Conclusion

In this study, a heparin-like poly(vinyl pyrrolidone)-capped polyurethane (PVP-HLPU) was designed by reversible addition-fragmentation chain transfer polymerization combined with a sulfonation. The obtained PVP-HLPU could be directly blended with PES matrix to prepare membranes. The modified membranes showed excellent hemocompatibility and excellent protein antifouling properties compared with pristine PES membrane. In a conclusion, it is an effective system to evaluate the blood compatibility of the membranes by combination of APTT, TT, and platelet adhesion and so on. That is not to say that there is no drawback by use of these three methods. Other methods such as complement activation, hemolysis test could also be employed to characterize the blood compatibility of polymeric materials. Nonetheless,

our results indicated that the PVP-HLPU modified membranes had great potential to be used in blood purification.

Competing Interests

The authors declare that they have no competing interests.

Acknowledgments

This work was financially sponsored by the National Natural Science Foundation of China (nos. 51225303 and 51433007).

References

- [1] K. Sariibrahimoglu, W. Yang, S. C. G. Leeuwenburgh et al., "Development of porous polyurethane/strontium-substituted

- hydroxyapatite composites for bone regeneration,” *Journal of Biomedical Materials Research Part A*, vol. 103, no. 6, pp. 1930–1939, 2015.
- [2] A. T. Stevenson, L. M. Reese, T. K. Hill et al., “Fabrication and characterization of medical grade polyurethane composite catheters for near-infrared imaging,” *Biomaterials*, vol. 54, pp. 168–176, 2015.
 - [3] Q. Chai, Y. Huang, and N. Ayres, “Shape memory biomaterials prepared from polyurethane/ureas containing sulfated glucose,” *Journal of Polymer Science, Part A: Polymer Chemistry*, vol. 53, no. 19, pp. 2252–2257, 2015.
 - [4] Y.-J. Huang, K.-C. Hung, F.-Y. Hsieh, and S.-H. Hsu, “Carboxyl-functionalized polyurethane nanoparticles with immunosuppressive properties as a new type of anti-inflammatory platform,” *Nanoscale*, vol. 7, no. 48, pp. 20352–20364, 2015.
 - [5] J. Cheng, X. Tang, J. Zhao, T. Shi, P. Zhao, and C. Lin, “Multifunctional cationic polyurethanes designed for non-viral cancer gene therapy,” *Acta Biomaterialia*, vol. 30, pp. 155–167, 2016.
 - [6] C. Akduman, I. Özgüney, and E. P. A. Kumbasar, “Preparation and characterization of naproxen-loaded electrospun thermoplastic polyurethane nanofibers as a drug delivery system,” *Materials Science and Engineering: C*, vol. 64, pp. 383–390, 2016.
 - [7] R. B. Trinca, G. A. Abraham, and M. I. Felisberti, “Electrospun nanofibrous scaffolds of segmented polyurethanes based on PEG, PLLA and PTMC blocks: physico-chemical properties and morphology,” *Materials Science & Engineering C*, vol. 56, pp. 511–517, 2015.
 - [8] F.-Y. Hsieh, H.-H. Lin, and S.-H. Hsu, “3D bioprinting of neural stem cell-laden thermoresponsive biodegradable polyurethane hydrogel and potential in central nervous system repair,” *Biomaterials*, vol. 71, pp. 48–57, 2015.
 - [9] L. Rueda-Larraz, B. F. d’Arlas, A. Tercjak, A. Ribes, I. Mondragon, and A. Eceiza, “Synthesis and microstructure–mechanical property relationships of segmented polyurethanes based on a PCL–PTHF–PCL block copolymer as soft segment,” *European Polymer Journal*, vol. 45, no. 7, pp. 2096–2109, 2009.
 - [10] R. Wang, T. Xiang, W.-F. Zhao, and C.-S. Zhao, “A facile approach toward multi-functional polyurethane/polyethersulfone composite membranes for versatile applications,” *Materials Science and Engineering: C*, vol. 59, pp. 556–564, 2016.
 - [11] F. Zia, K. M. Zia, M. Zuber, S. Tabasum, and S. Rehman, “Heparin based polyurethanes: a state-of-the-art review,” *International Journal of Biological Macromolecules*, vol. 84, pp. 101–111, 2016.
 - [12] M. Tan, Y. Feng, H. Wang et al., “Immobilized bioactive agents onto polyurethane surface with heparin and phosphorylcholine group,” *Macromolecular Research*, vol. 21, no. 5, pp. 541–549, 2013.
 - [13] F. Kara, E. A. Aksoy, S. Calamak, N. Hasirci, and S. Aksoy, “Immobilization of heparin on chitosan-grafted polyurethane films to enhance anti-adhesive and antibacterial properties,” *Journal of Bioactive and Compatible Polymers: Biomedical Applications*, vol. 31, no. 1, pp. 72–90, 2016.
 - [14] E. A. Aksoy, V. Hasirci, N. Hasirci, A. Motta, M. Fedel, and C. Migliaresi, “Plasma protein adsorption and platelet adhesion on heparin-immobilized polyurethane films,” *Journal of Bioactive and Compatible Polymers*, vol. 23, no. 6, pp. 505–519, 2008.
 - [15] Y.-T. Hou, H. Ijima, T. Takei, and K. Kawakami, “Growth factor/heparin-immobilized collagen gel system enhances viability of transplanted hepatocytes and induces angiogenesis,” *Journal of Bioscience and Bioengineering*, vol. 112, no. 3, pp. 265–272, 2011.
 - [16] E. Brynda and M. Houska, “Multiple alternating molecular layers of albumin and heparin on solid surfaces,” *Journal of Colloid and Interface Science*, vol. 183, no. 1, pp. 18–25, 1996.
 - [17] C. Zhao, J. Xue, F. Ran, and S. Sun, “Modification of polyethersulfone membranes—a review of methods,” *Progress in Materials Science*, vol. 58, no. 1, pp. 76–150, 2013.
 - [18] C. Zhao, S. Nie, M. Tang, and S. Sun, “Polymeric pH-sensitive membranes—a review,” *Progress in Polymer Science*, vol. 36, no. 11, pp. 1499–1520, 2011.
 - [19] L. Ma, B. Su, C. Cheng et al., “Toward highly blood compatible hemodialysis membranes via blending with heparin-mimicking polyurethane: study in vitro and in vivo,” *Journal of Membrane Science*, vol. 470, pp. 90–101, 2014.
 - [20] W. Zhao, Q. Mou, X. Zhang, J. Shi, S. Sun, and C. Zhao, “Preparation and characterization of sulfonated polyethersulfone membranes by a facile approach,” *European Polymer Journal*, vol. 49, no. 3, pp. 738–751, 2013.
 - [21] R. Chan and V. Chen, “Characterization of protein fouling on membranes: opportunities and challenges,” *Journal of Membrane Science*, vol. 242, no. 1-2, pp. 169–188, 2004.
 - [22] Y.-L. Su, W. Cheng, C. Li, and Z. Jiang, “Preparation of antifouling ultrafiltration membranes with poly(ethylene glycol)-graft-polyacrylonitrile copolymers,” *Journal of Membrane Science*, vol. 329, no. 1-2, pp. 246–252, 2009.
 - [23] A. L. Lim and R. Bai, “Membrane fouling and cleaning in microfiltration of activated sludge wastewater,” *Journal of Membrane Science*, vol. 216, no. 1-2, pp. 279–290, 2003.
 - [24] A. Rahimpour, S. S. Madaeni, S. Zeresghi, and Y. Mansourpanah, “Preparation and characterization of modified nanoporous PVDF membrane with high antifouling property using UV photo-grafting,” *Applied Surface Science*, vol. 255, no. 16, pp. 7455–7461, 2009.
 - [25] J. Kost, “Protein at interfaces II. Fundamentals and applications,” *Journal of Controlled Release*, vol. 45, no. 1, p. 113, 1997.
 - [26] M. Rabe, D. Verdes, and S. Seeger, “Understanding protein adsorption phenomena at solid surfaces,” *Advances in Colloid and Interface Science*, vol. 162, no. 1-2, pp. 87–106, 2011.
 - [27] H. Chen, L. Yuan, W. Song, Z. Wu, and D. Li, “Biocompatible polymer materials: role of protein–surface interactions,” *Progress in Polymer Science*, vol. 33, no. 11, pp. 1059–1087, 2008.
 - [28] B. Sivaraman and R. A. Latour, “Delineating the roles of the GPIIb/IIIa and GP-Ib-IX-V platelet receptors in mediating platelet adhesion to adsorbed fibrinogen and albumin,” *Biomaterials*, vol. 32, no. 23, pp. 5365–5370, 2011.
 - [29] H. Wang, T. Yu, C. Zhao, and Q. Du, “Improvement of hydrophilicity and blood compatibility on polyethersulfone membrane by adding polyvinylpyrrolidone,” *Fibers and Polymers*, vol. 10, no. 1, pp. 1–5, 2009.
 - [30] J. W. M. Heemskerk, E. M. Bevers, and T. Lindhout, “Platelet activation and blood coagulation,” *Thrombosis and Haemostasis*, vol. 88, no. 2, pp. 186–193, 2002.
 - [31] C. H. Gemmell, “Assessment of material-induced procoagulant activity by a modified russell viper venom coagulation time test,” *Journal of Biomedical Materials Research*, vol. 42, no. 4, pp. 611–616, 1998.
 - [32] M. B. Gorbet and M. V. Sefton, “Biomaterial-associated thrombosis: roles of coagulation factors, complement, platelets and leukocytes,” *Biomaterials*, vol. 25, no. 26, pp. 5681–5703, 2004.
 - [33] A. Remes and D. F. Williams, “Immune response in biocompatibility,” *Biomaterials*, vol. 13, no. 11, pp. 731–743, 1992.

Research Article

Use of Oxalic-Acid-Modified Stellerite for Improving the Filter Capability of PM_{2.5} of Paper Composed of Bamboo Residues

Hua Chen,^{1,2,3} Jian Lou,¹ Fei Yang,⁴ Jia-nan Zhou,¹ Yan Zhang,¹ and Huabo Yao¹

¹Zhejiang Provincial Key Lab for Chem & Bio Processing Technology of Farm Product, Key Laboratory of Recycling and Eco-Treatment of Waste Biomass of Zhejiang Province, Zhejiang University of Science and Technology, Hangzhou 310023, China

²Key Laboratory of Pulp and Paper Science & Technology of Ministry of Education of China, Qilu University of Technology, Jinan 250353, China

³Zhejiang Yongtai Paper Co. Ltd, Hangzhou 311421, China

⁴State Key Lab of Pulp and Paper Engineering, South China University of Technology, Guangzhou 510640, China

Correspondence should be addressed to Fei Yang; yangfei@scut.edu.cn

Received 5 October 2016; Accepted 21 November 2016

Academic Editor: Weifeng Zhao

Copyright © 2016 Hua Chen et al. This is an open access article distributed under the Creative Commons Attribution License, which permits unrestricted use, distribution, and reproduction in any medium, provided the original work is properly cited.

In this study, pulping conditions for kraft pulping of bamboo residues were investigated, predominantly focusing on cooking temperature and time during pulping. Oxalic acid and cationic starch were used for the modification of natural stellerite, and the use of modified stellerite for preparing filter paper for PM_{2.5} filtration was investigated. The optimal pulping technology of bamboo residues was established based on the following experimental parameters: liquor ratio of 1:5.5, cooking temperature of 160°C, and a holding time of 2 h. Modification by oxalic acid resulted in the promotion of pore formation at the stellerite surfaces and induced the microscopic changes. Nevertheless, paper strength remained practically unchanged after the addition of fillers, indicating that the cationic starch preblend method is a promising technique for papermaking because it enhances the strength properties of paper. With the variation in the addition of modified stellerite from 3 to 15%, while simultaneously maintaining the basis weight constant at 60 gm⁻², the filtration efficiency of paper sheets first increased and then decreased later; thus the optimum stellerite content was found to be 9%. Filtration efficiency was suggested to be affected by gas flowing velocity.

1. Introduction

With the economic development of China as well as the growth of its transportation industry, air pollution is becoming more serious in recent years. Several contaminants and pollutants can be adsorbed on the particles suspended in the atmosphere and enter the body via respiration.

Most studies have reported that PM_{2.5} (particles with an aerodynamic diameter of 2.5 μm or less) [1] with small average particles size, large-scale impact, and high specific surface area can enter the human respiratory system and even penetrate through the lung cells into blood circulation, posing serious hazards to human health [2], including asthma [3] and bronchitis [4]. More importantly studies have increasingly reported that PM_{2.5} possibly stimulates the mutation of the p53 gene in nasopharyngeal epithelial cells and plays an important role in the carcinogenesis of oral tissues [5].

According to the American Cancer Society, an 8% increase in cancer mortality for every 10 μgm⁻³ increase in PM_{2.5} consistency for city population has been observed.

On the other hand, China has the richest resources of bamboo in the world, where 33,000 km² or 3% of the country's total forest area is occupied by bamboo [6]. With the development of the bamboo industry, a large number of residues are produced, and the utilization of these bamboo residues is not greater than 10%, where its collecting and treatment has noticed by people [7].

Both domestic and international studies have indicated that fiber filter material exhibits several advantages, such as mass production, low cost, high surface area, porous nature, and good flexibility [8–12]. The main raw materials used for filter material for high-efficiency PM_{2.5} capture include natural plant, synthetic fiber, glass, ceramic, and metal fibers.

TABLE 1: Cooking process.

Sample	Extension	Cooking temperature (°C)	Cooking time (h)
BR	Bamboo residue	—	—
P1	Pulp 1	150	1.5
P2	Pulp 2	150	2.0
P3	Pulp 3	150	2.5
P4	Pulp 4	160	1.5
P5	Pulp 5	160	2.0
P6	Pulp 6	160	2.5

Natural plant fiber, such as bamboo residues, is probably the most promising one among various PM_{2.5} filter materials, attributed to its wide spread sources, low cost, and excellent reprocessing performance.

Zeolite is a type of aqueous silicoaluminate mineral with excellent adsorption characteristics. Porous zeolites have been widely used in catalysis, adsorption, and separation attributed to their open frameworks, high surface areas, and ordered pore structures [13–15]. Nevertheless, few studies have been reported on natural zeolite, despite its low cost and abundant storage [16].

In this study, the effect of filter paper made from bamboo residue and oxalic-acid-modified stellerite on PM_{2.5} filtration was comprehensively investigated. Factors affecting pulping and the use of stellerite were also investigated.

2. Experimental

2.1. Materials

2.1.1. Raw Materials. Stellerite was purchased from Jinshansida Co., Ltd. (Guilin, China). Oxalic acid, sodium hydroxide (NaOH), and sodium sulfide nonahydrate (Na₂S·9H₂O) with purities of 96% were supplied by Linfeng Chemical Co., Ltd. (Shanghai, China). Cationic starch with a substitution degree of 0.028 was purchased from Hengfeng Chemical Co., Ltd. (Zhejiang, China). Bamboo (*Bambusa rigida species*) residue was provided by a bamboo products company (Anji, China). The residue exhibited the following average characteristics: 49.96% cellulose, 22.88% total lignin, and 17.97% hemicelluloses.

2.1.2. Pulping and Beating. First, bamboo residue (abbreviated as BR) was crushed and screened through a mesh with a size of 160. According to ISO 287-1985 standard, its moisture content was determined to be 12.27%. Pulping was conducted by the kraft pulping method with a liquor ratio of 1 : 5.5, active alkali of 30%, and a sulfured degree of 30%. Samples were referred to as P1, P2, P3, P4, P5, and P6 according to the cooking process as shown in Table 1.

Filtration and washing were conducted after pulping. Finally, the pulp was refined to 30°SR using a TD7 Refiner (TD7-PFI, SUST, Shanxi, China).

2.1.3. Modification of Stellerite. Stellerite was obtained from Jinshansida Co., Ltd. (Guangxi, China). First, stellerite was repeatedly washed using distilled water for removing some impurity ions, and this was followed by dehydration in an oven box at 100°C for 12 h. Second, stellerite (7.5 g) was added into a round flask containing aqueous solution of oxalic acid (150 mL, 1.0 molL⁻¹). Third, the reaction temperature was maintained constant at 85°C for 5 h under stirring. Next, the solid liquid mixture was filtered, and stellerite was washed with distilled water. Further, a AgNO₃ test was performed to ensure the absence of remaining Cl⁻ ions in stellerite. After grinding, stellerite was calcined at 105°C for 12 h.

2.1.4. Capping of Cationic Starch Preblend. First, distilled water (400 mL) and cationic starch (20 g) were added together in a 500-mL four-necked-round-bottom flask; and the resulting slurry was stirred to ensure sufficient mixing. Second, modified stellerite (20 g) was added to the slurry, and after stirring for 25 min at 90°C, it was dried at 95°C for 12 h. Finally, the mixture was ground into a powder, and cationic-starch-capped modified stellerite was prepared by the preblend method, with a mass ratio of 1:1 for cationic starch and modified stellerite.

2.1.5. Preparation of Hand Sheets and Testing. First, the beaten pulp was diluted to a consistency of 1.2% using distilled water, followed by disintegration using a standard disintegrator at 20,000 revolutions until all fiber bundles were dispersed. Second, cationic-starch-capped modified stellerite was added under stirring at 3000 revolutions for 1 min, where the concentration of the added fillers was maintained constant at 3, 6, 9, 12, and 15% (based on oven-dry pulp mass). Hand sheets with a target basis weight of 60 gm⁻² were prepared using the ZBJ1-B Automatic Sheet Former System (SUST, Shanxi, China) according to TAPPI T 205 (TAPPI Test Methods, 2002), with the exception that the pressure utilized for wet sheet pressing was controlled at 200 kPa, followed by drying at 102°C using a Formax 12" Drum Dryer (Thwing-Albert Instrument, USA). The hand sheets were conditioned under a controlled environment (temperature of 23 ± 1°C and relative humidity of 50 ± 1%) before analysis.

The tensile index and air permeability of hand sheets were determined according to the relevant TAPPI Standards. The tensile index of the paper sheets was determined using a WZL-300B Tensile Strength Tester (Qitongboke, China), and air permeability was tested using an Air Permeance Tester (Messmer Instruments Ltd., Testing Machines Inc., USA). The ash content of the fibers was measured according to ISO 2144:1997 method, and the ash content of the pulp and paper sheets was determined according to TAPPI T 413 om-85 (1985) standards. The retention efficiency of the fillers was calculated by using

$$R = \frac{(A - B) \cdot (1 - L - C)}{(L - B) \cdot (1 - A - C)} \times 100\%. \quad (1)$$

Here, *A*, *B*, and *L* represent the ash content of the paper sheets, fiber, and pulp, respectively, and *C* represents the loss on ignition of stellerite.

TABLE 2: Pore structure analysis of fibers and stellerite.

Sample	Specific surface area (S_{BET} , $\text{m}^2 \text{g}^{-1}$)	Pore volume ($V_{t\text{-plot}}$, $\text{cm}^3 \text{g}^{-1}$)	Pore size (D_{BET} , nm)	Yield (%)
P1	0.0064 ± 0.0001	0.000126 ± 0.000003	2941.4 ± 76.48	35.46 ± 0.85
P2	0.0316 ± 0.0001	0.000169 ± 0.000007	714.2 ± 14.99	38.19 ± 0.99
P3	0.0687 ± 0.0002	0.000269 ± 0.000010	405.1 ± 10.94	39.72 ± 1.23
P4	0.0753 ± 0.0005	0.000322 ± 0.000009	218.5 ± 5.244	40.98 ± 0.98
P5	0.0932 ± 0.0007	0.000358 ± 0.000012	89.4 ± 1.699	42.91 ± 1.03
P6	0.0417 ± 0.0008	0.000125 ± 0.000004	120.2 ± 3.366	36.77 ± 1.02
Natural stellerite	2.2179 ± 0.0581	0.000487 ± 0.000012	8.0 ± 0.152	—
Modified stellerite	108.8327 ± 2.1921	0.051550 ± 0.001288	1.9 ± 0.034	91.41 ± 2.01

Filtration efficiencies of various hand sheets were investigated using TSI-8130 Automated Filter Tester (TSI Company, USA). The $0.3 \mu\text{m}$ NaCl particle was used as the filtration simulation model (adjusted flow of 32 Lmin^{-1}).

2.1.6. Determination of Pore Distribution. A pore size distribution detector ASAP2010M (Micromeritics, USA) was used for the structural analyses of fiber pores. High-purity N_2 was used as the adsorbate, and the adsorption-desorption of high-purity N_2 was determined at 77 K in a liquid nitrogen trap by a static volumetric method.

2.1.7. Fourier Transform Infrared Spectroscopy Analysis. Fourier transform infrared (FTIR) spectroscopy analysis of the samples was conducted in the transmission mode by macrotechniques (13 mm Φ pellet; ca. 1.5 mg sample with 350 mg KBr). The spectra were recorded using a Nexus Vector spectrometer (Nexus 670, Thermo Nicolet Company, USA) under the following specifications: Apodization: triangular; detector: DTGS/KBr; regulation: 4 cm^{-1} ; and number of scans: 32.

2.1.8. X-Ray Diffraction Analysis. The X-ray powder diffraction (XRD) patterns of the samples were recorded on a Bruker D8 Advance XRD instrument (step size of 0.02° with 17.7 s per step). A Generator with 40 kV and a current of 40 mA were employed as sources for $\text{CuK}\alpha$ radiation.

The crystallinity index was calculated from the relative intensities of the diffraction peaks [17] as follows:

$$a = \frac{I_{020}}{(I_{020} + I_{\text{am}})} \times 100\%. \quad (2)$$

Here, I_{020} represents the intensity ($2\theta \approx 22.5^\circ$) of the peak belonging to the {020}, which contributes to the strength of the crystalline region, and I_{am} represents the intensity ($2\theta \approx 18^\circ$) between the {020} and {110}, which represents the intensity of the amorphous region.

2.1.9. Scanning Electron Microscopy Analysis. Morphologies of the hand sheet surfaces were examined by scanning electron microscopy (SEM, JSM-IT300, JEOL, Japan) operating at an accelerating voltage of 15 kV. Before observation, the samples were coated with gold using a vacuum sputter-coater.

All experiments were conducted in triplicate with a relative standard deviation (RSD) of approximately 5%.

3. Results and Discussion

3.1. Pore Structure Analysis of Fibers and Stellerite. Table 2 lists the results obtained from the pore structural analysis of fibers and stellerite. The results indicated that, with increasing cooking degree, surface area and pore volume became greater than the initial volume. Moreover, pore size significantly decreased, indicative of the generation of abundant micropores and mesopores. At this stage, the pulping yield increased because of the reduction in the discharge rate during filtration after cooking. However, cooking for a long time resulted in overcooking, leading to a decrease of surface area and the destruction of the fiber porous structure. Moreover, pulping yield also decreased during overcooking, attributed to the massive reduction of fines in washing process. Thus, the optimal pulping conditions were as follows: cooking temperature of 160°C and a holding time of 2 h (sample P5).

With respect to the oxalic-acid-modified stellerite, specific surface area (S_{BET}) for natural stellerite was $2.2179 \text{ m}^2 \text{g}^{-1}$; in contrast, for the sample treated with 1.0 mol L^{-1} oxalic acid, S_{BET} was $108.8327 \text{ m}^2 \text{g}^{-1}$ (increase by 49 times). In particular, pore size (D_{BET}) was also significantly less than that observed for natural stellerite, indicating that a microporous structure was formed. Moreover, the modification yield was 91.41%, attributed to the removal of impurities and loss during washing.

3.2. Functional Group Analysis of Different Samples. Figure 1 shows the FTIR spectra of samples BR, P1, P2, P3, P4, P5, and P6. The peak observed at 3447 cm^{-1} is attributed to the hydroxyl groups (OH) in the fibers; it is a band characteristic of cellulose [18]. The peak observed at 2960 cm^{-1} is attributed to the C–H absorption. The strong band observed at 1642 cm^{-1} is attributed to the vibration of absorbed water molecules in the noncrystalline region of cellulose. The band observed at 1511 cm^{-1} is attributed to the vibration of the aromatic ring of lignin, and the peak observed at 1735 cm^{-1} is ascribed to the C=O stretching vibration of acetyl and carboxyl of hemicellulose [19]. The comparison of the different spectra indicated that, with increasing cooking degree, the cellulose characteristics of spectra were more apparent,

TABLE 3: Effect of the variation of stellerite content on filter performance*.

Dosage of stellerite (%)	0	3	6	9	12	15
Filtration efficiency (%)	59.3 ± 2.1	72.5 ± 1.9	74.1 ± 2.3	78.4 ± 2.5	76.5 ± 2.9	75.8 ± 3.1

* Gas flowing velocity = 0.2 ms⁻¹.

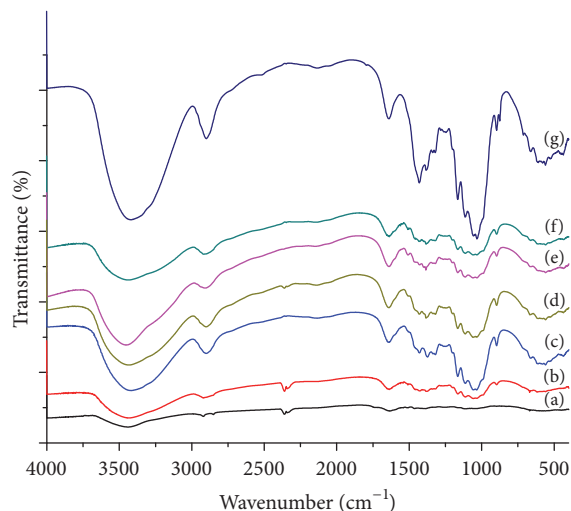


FIGURE 1: FTIR spectroscopy of different pulp samples: (a) BR, (b) P1, (c) P2, (d) P3, (e) P4, (f) P5, and (g) P6.

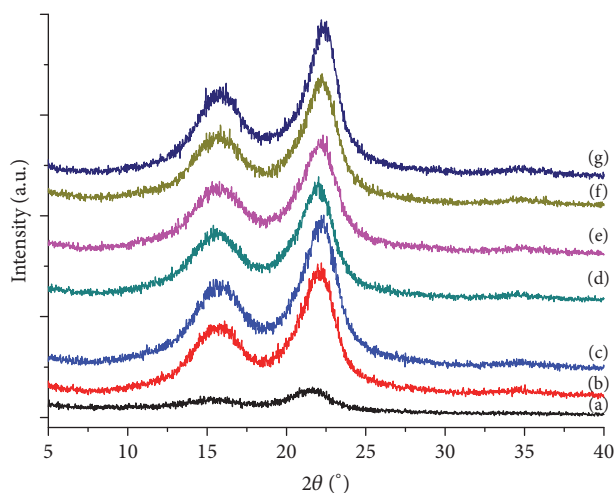


FIGURE 2: XRD curves of different samples: (a) BR, (b) P1, (c) P2, (d) P3, (e) P4, (f) P5, and (g) P6.

attributed to the fact that, in comparison, cellulose, lignin, and hemicellulose degrade more rapidly in the cooking process.

3.3. XRD Patterns of Fibers. Figure 2(a) shows the XRD patterns of bamboo residues, exhibiting low crystallinity (crystallinity index = 51.8%), as evidenced by their faint pattern. The crystallinity of pulp clearly increased after cooking, with the main peaks observed at 2θ of 22.5° and 18°, attributed to {020}, and the amorphous region of cellulose.

Moreover, the crystallinity of P1, P2, P3, P4, P5, and P6 increased to 54.4, 55.6, 56.8, 57.2, 59.9, and 57.8%, respectively. This result is attributed to the following two reasons: the removal of disordered material in the amorphous region and the formation of new crystalline region, ascribed to the realignment of the cellulose chain caused by the penetration of water molecules into the amorphous region [19].

3.4. SEM Images of Different Samples. Figure 3 shows the SEM images of different samples, clearly displaying their surface morphology. The bamboo residues consist of piece structure, with several pits randomly distributed on the residue surface (Figure 3(a)). The bamboo fibers with complete shape and clear contours were obtained for the appropriate cooking process (P5, Figure 3(b)). Natural stellerite exhibits a clear layer structure (Figure 3(c)). Treatment with oxalic acid led to the formation of cracks on its surface, resulting in the promotion of pore formation at the stellerite surfaces and induced microscopic changes; this result is consistent with those shown in Table 2 (Figure 3(d)). Figure 3(e) shows the hand sheet without fillers, and Figure 3(f) demonstrates the distribution of granular-modified stellerite between fibers.

3.5. Ash Content and Filler Retention. Figure 4 shows the ash content and filler retention of different paper sheets. With increasing stellerite content, ash content increases, and approximately 7.2% of ash was obtained with the addition of 15% stellerite. In contrast, filler retention significantly decreases.

3.6. Tensile Indices and Air Permeability of Paper Sheets. Figure 5 shows the effects of stellerite content on the tensile indices and air permeability of the paper sheets. Compared to the control (without stellerite), the tensile index of the paper sheet with the addition of 3% stellerite indicated a 3.7% increase; however, the ash content increased from 0.14 to 1.98%. Thus, under experimental conditions employed in this study, appropriate addition of cationic-starch-preblend-modified stellerite exerted a certain positive effect on the tensile index of the paper sheet, possibly attributed to the improvement of evenness. Moreover, with increasing filler content, air permeability also increased. With the addition of 15% stellerite, the air permeability of the paper sheet increased from 3.44 to 6.62 $\mu\text{m Pa}^{-1} \text{s}^{-1}$, indicating that the porosity of the paper increased because of the addition of filler.

3.7. Filter Performance of Paper Sheets. Tables 3 and 4 summarize the filter performance of different paper sheets and the impact of gas flowing velocities. The filter performance was suggested to be affected not only by the dosage of fillers, but also by the gas flowing velocities during testing. The best performance was obtained with the addition of 9% modified

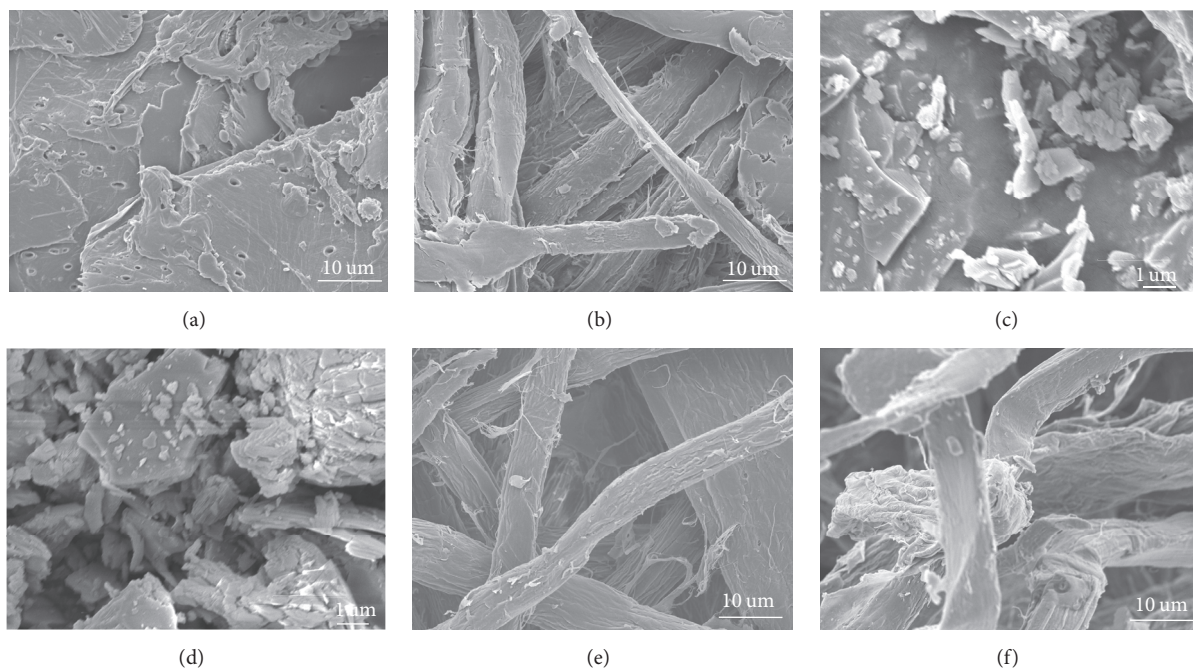


FIGURE 3: SEM images of different samples: (a) BR, (b) P5, (c) natural stellerite, (d) modified stellerite, (e) hand sheet composed of P5 without stellerite, and (f) hand sheet composed of P5 with modified stellerite (9%).

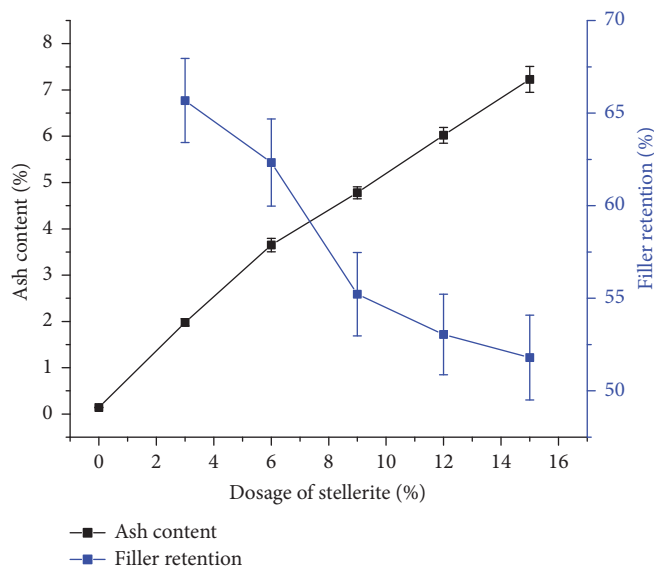


FIGURE 4: Ash content and filler retention of different paper sheets.

TABLE 4: Effect of different gas flowing velocities on filter performance*.

Gas flowing velocities (ms^{-1})	0.2	0.4	0.6	0.8
Filtration efficiency (%)	78.4 ± 2.8	69.7 ± 1.7	62.6 ± 2.5	58.2 ± 2.0

* Dosage of stellerite = 9%.

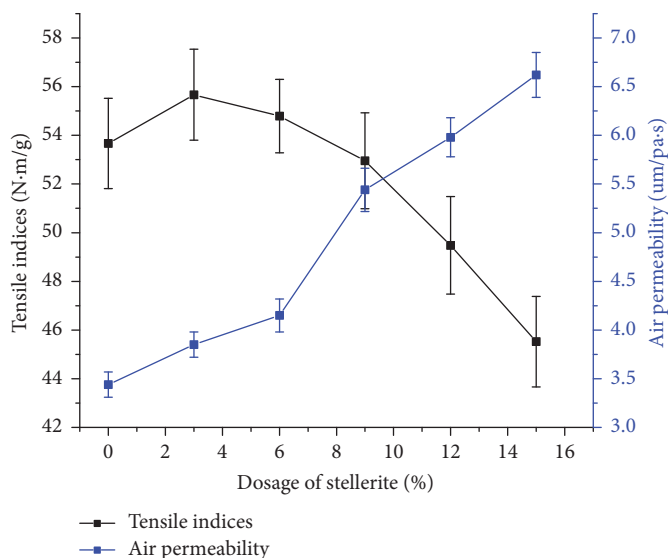


FIGURE 5: Tensile indices and air permeability of paper sheets.

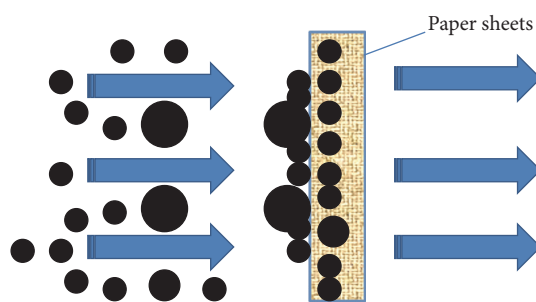


FIGURE 6: Filtration sketch of paper sheets.

stellerite, predominantly attributed to the fact that extremely high air permeability of paper sheets results in the decline of adsorption quantity. This result indicates the existence of an important difference between fibers and fillers in the adsorption of $PM_{2.5}$. It has been reported that micron wood fibers have low collection efficiency toward particles with the diameter from 0.4 to 0.6 μm , while they have significantly higher collection efficiency for particles with other sizes. Among these particles with the diameter of 0.01 μm , the collection efficiency of micron wood fibers can reach up to 90% [20].

In fact, the filtering process of $PM_{2.5}$ particles by plant fibers and fillers is very complex and specific to location; therefore, filter performance is affected not only by the z -direction position, but also by time. This observation is referred to as layered filtration and nonstationary filtration (see Figure 6), which will be further explored in our future study.

4. Conclusions

In this study, the following optimum cooking condition of the bamboo residues by kraft pulping was established: a

liquor ratio of 1:5.5, a cooking temperature of 160°C, and a holding time of 2 h. Modification with oxalic acid resulted in the promotion of pore formation at the stellerite surfaces, which induced microscopic changes while simultaneously maintaining the porous structure of stellerite. The cationic starch preblend method is a promising technique for paper-making as it results in the enhanced strength of paper. The filter performance of paper sheets was significantly increased by the addition of oxalic-acid-modified stellerite. With the addition of 9% oxalic-acid-modified stellerite, the paper sheet exhibited the best filter performance (78.4%) at a gas flowing velocity of 0.2 ms^{-1} .

Competing Interests

The authors declare that they have no competing interests.

Acknowledgments

The authors greatly acknowledge the support from the Zhejiang Provincial Natural Science Foundation of China (Grant no. LY15C160002), Zhejiang Provincial Collaborative Innovation Center of Agricultural Biological Resources Biochemical Manufacturing (Grant no. 2016KF0016), and Key Laboratory of Recycling and Eco-Treatment of Waste Biomass of Zhejiang Province (Grant no. 2016REWB12).

References

- [1] W.-B. Xue, F. Fu, J.-N. Wang et al., "Numerical study on the characteristics of regional transport of $PM_{2.5}$ in China," *China Environmental Science*, vol. 34, no. 6, pp. 1361–1368, 2014.
- [2] B. Luo, H. Shi, L. Wang et al., "Rat lung response to $PM_{2.5}$ exposure under different cold stresses," *International Journal of Environmental Research and Public Health*, vol. 11, no. 12, pp. 12915–12926, 2014.

- [3] C. Loftus, M. Yost, P. Sampson et al., "Regional PM_{2.5} and asthma morbidity in an agricultural community: a panel study," *Environmental Research*, vol. 136, pp. 505–512, 2015.
- [4] R. Ghosh, P. Rossner, K. Honkova, M. Dostal, R. J. Sram, and I. Hertz-Picciotto, "Air pollution and childhood bronchitis: interaction with xenobiotic, immune regulatory and DNA repair genes," *Environment International*, vol. 87, pp. 94–100, 2016.
- [5] L. Calderon-Garciduenas, A. Rodriguez-Alcaraz, A. Villarreal-Calderon, O. Lyght, D. Janszen, and K. T. Morgan, "Nasal epithelium as a sentinel for airborne environmental pollution," *Toxicological Sciences*, vol. 46, no. 2, pp. 352–364, 1998.
- [6] J. M. O. Scurlock, D. C. Dayton, and B. Hames, "Bamboo: an overlooked biomass resource?" *Biomass and Bioenergy*, vol. 19, no. 4, pp. 229–244, 2000.
- [7] M. He, Y. Zhang, Q. Hu et al., "Comparison of different pre-treatment methods for bamboo residues," *Chinese Journal of Applied Environmental Biology*, vol. 17, no. 2, pp. 232–236, 2011.
- [8] J. Li, F. Gao, L. Q. Liu, and Z. Zhang, "Needleless electro-spun nanofibers used for filtration of small particles," *Express Polymer Letters*, vol. 7, no. 8, pp. 683–689, 2013.
- [9] J. Li, X. Shi, F. Gao et al., "Filtration of fine particles in atmospheric aerosol with electrospinning nanofibers and its size distribution," *Science China Technological Sciences*, vol. 57, no. 2, pp. 239–243, 2014.
- [10] Y. Mei, Z. Wang, and X. Li, "Improving filtration performance of electrospun nanofiber mats by a bimodal method," *Journal of Applied Polymer Science*, vol. 128, no. 2, pp. 1089–1094, 2013.
- [11] J. Lang, S. Cheng, J. Li et al., "A monitoring and modeling study to investigate regional transport and characteristics of PM_{2.5} pollution," *Aerosol and Air Quality Research*, vol. 13, no. 3, pp. 943–956, 2013.
- [12] N. Vitichuli, Q. Shi, J. Nowak, M. McCord, M. Bourham, and X. Zhang, "Electrospun ultrathin nylon fibers for protective applications," *Journal of Applied Polymer Science*, vol. 116, no. 4, pp. 2181–2187, 2010.
- [13] L. Wang, C. Han, M. N. Nadagouda, and D. D. Dionysiou, "An innovative zinc oxide-coated zeolite adsorbent for removal of humic acid," *Journal of Hazardous Materials*, vol. 313, pp. 283–290, 2016.
- [14] K. Guesh, C. Márquez-Álvarez, Y. Chebude, and I. Díaz, "Enhanced photocatalytic activity of supported TiO₂ by selective surface modification of zeolite Y," *Applied Surface Science*, vol. 378, pp. 473–478, 2016.
- [15] P. Vinaches, J. A. B. L. R. Alves, D. M. Melo, and S. B. C. Pergher, "Raw powder glass as a silica source in the synthesis of colloidal MEL zeolite," *Materials Letters*, vol. 178, pp. 217–220, 2016.
- [16] H. Chen, J. Wang, H. Wang et al., "Preparation of stellerite loading titanium dioxide photocatalyst and its catalytic performance on methyl orange," *Journal of Nanomaterials*, vol. 2015, Article ID 701589, 6 pages, 2015.
- [17] Y. M. Chen, J. Q. Wan, Y. W. Ma, W. W. Wu, and Y. Wang, "Effects of pressing and drying on the cellulose crystalline degree of recycled fiber," *China Pulp & Paper Industry*, vol. 8, pp. 26–29, 2008.
- [18] C. Da Silva Meireles, G. R. Filho, R. M. N. De Assunçã, M. Zeni, and K. Mello, "Blend compatibility of waste materials—cellulose acetate (from sugarcane bagasse) with polystyrene (from plastic cups): diffusion of water, FTIR, DSC, TGA, and SEM study," *Journal of Applied Polymer Science*, vol. 104, no. 2, pp. 909–914, 2007.
- [19] D. L. Cheng, S. X. Jiang, and Q. S. Zhang, "The effect and mechanism of cooking on the chemical components of bamboo fibers," *Journal of Bamboo Research*, vol. 29, no. 1, pp. 50–53, 2010.
- [20] X. R. Guo and P. Wang, "Simulation of steady collection efficiency of micron wood fiber pits on ultrafine particles," *Journal of Nanjing Forestry University: Natural Sciences Edition*, vol. 38, no. 3, pp. 98–102, 2014.

Research Article

Constructing Functional Ionic Membrane Surface by Electrochemically Mediated Atom Transfer Radical Polymerization

Fen Ran, Dan Li, and Jiayu Wu

State Key Laboratory of Advanced Processing and Recycling of Nonferrous Metals, Lanzhou University of Technology, Lanzhou 730050, China

Correspondence should be addressed to Fen Ran; ranfen@163.com

Received 22 August 2016; Accepted 5 September 2016

Academic Editor: Qiang Wei

Copyright © 2016 Fen Ran et al. This is an open access article distributed under the Creative Commons Attribution License, which permits unrestricted use, distribution, and reproduction in any medium, provided the original work is properly cited.

The sodium polyacrylate (PAA_{Na}) contained polyethersulfone membrane that was fabricated by preparation of PES-NH₂ via nonsolvent phase separation method, the introduction of bromine groups as active sites by grafting α -Bromoisobutyryl bromide, and surface-initiated electrochemically atom transfer radical polymerization (SI-eATRP) of sodium acrylate (AANa) on the surface of PES membrane. The polymerization could be controlled by reaction condition, such as monomer concentration, electric potential, polymerization time, and modifier concentration. The membrane surface was uniform when the monomer concentration was 0.9 mol/L, the electric potential was -0.12 V, the polymerization time was 8 h, and the modifier concentration was 2 wt.%. The membrane showed excellent hydrophilicity and blood compatibility. The water contact angle decreased from 84° to 68° and activated partial thromboplastin increased from 51 s to 84 s after modification of the membranes.

1. Introduction

Interfacial properties and interactions with cells and biological fluids play a vital role in the applications of polymers as biomaterials [1], and it is of great importance to control and manipulate the surface [2, 3]. It is well known that polymeric materials are widely used in the biomedical field such as cellulose acetate (CA), polymethylmethacrylate (PMMA), polyacrylonitrile (PAN), ethylene vinyl alcohol copolymer (EVAL), polyvinyl alcohol (PVA), polysulfone (PSf), and polyethersulfone (PES) [4]. Among these materials used in the biomedical field, polyethersulfone (PES) is one of the most important polymeric materials and is widely used as biomaterial for good chemical, thermal and hydrolytic stability, wide pH applicable scope, and oxidation resistance. However, blood compatibility and hydrophilicity of PES are not ideal because of intrinsic hydrophobicity.

To improve hydrophilicity and biocompatibility of PES membranes, several polymers were used for surface modification over the past two decades, such as heparin [5], heparin-like polymers [6], polyethylene glycol (PEG) [7],

and zwitterionic polymers [8]. Furthermore, many methods including coating method [9], UV grafting [10], plasma treatment [11], and surface-initiated atom transfer radical polymerization (SI-ATRP) [12] have been employed for immobilizing some functional groups onto PES membrane surfaces. ATRP-based method is one of the most popular methods of these modification techniques.

Controlled living radical polymerization has been researched in the past few decades. Matyjaszewski et al. reported the ATRP firstly. In the ATRP system, oxidation state metal halide salt $\text{Cu}^{\text{I}}\text{L}^+$ take halogen atoms from organic halide in the R-X to produce high oxidation state metal halide $\text{X-Cu}^{\text{II}}\text{L}^+$ and propagating radicals $[\text{R}\cdot]$ and $[\text{R}\cdot]$ induced monomer polymerization to produce R-Mn \cdot ; R-Mn \cdot take halogen atoms afresh to produce R-Mn-X and $\text{Cu}^{\text{I}}\text{L}^+$ [13, 14]. Radical polymerization at the same time is accompanied with the reversible and balanced reaction between free radical activity and organic macromolecular halide dormant species. ATRP is widely used for the synthesis of block and graft polymers based on a wide variety of monomers [15–17]. However, the association of X- to $\text{Cu}^{\text{II}}\text{L}^{2+}$ diminishes the concentration

of deactivator $X\text{-Cu}^{\text{II}}\text{L}^+$, and ATRP aqueous has a relatively large ratio of activators ($\text{Cu}^{\text{I}}\text{L}^+$) and deactivators ($X\text{-Cu}^{\text{II}}\text{L}^+$), which provides a high $[\text{R}\cdot]$ and fast polymerizations [18, 19], so it is difficult to achieve polymerization control and the targeted degree of polymerization via ATRP [20, 21]. Matyjaszewski et al. solved above problems by introducing electrochemistry in ATRP technology which was named electrochemically atom transfer radical polymerization (eATRP). eATRP system includes solvent, monomer, initiator, and catalyst $\text{Cu}^{\text{II}}\text{L}^{2+}$. The onset of polymerization begins only when sufficient potential is applied to the cathode so that reduction of $\text{Cu}^{\text{II}}\text{L}^{2+}$ to $\text{Cu}^{\text{I}}\text{L}^+$ occurs at the working electrode. The magnitude of potential can be appropriately chosen to achieve continuous (re)generation of a small quantity of $\text{Cu}^{\text{I}}\text{L}^+$ and consequently dictate the $[\text{R}\cdot]$. A living polymerization process is ensured by the combination of a low $[\text{R}\cdot]$ and high $[\text{Cu}^{\text{II}}\text{L}^{2+}]/[\text{Cu}^{\text{I}}\text{L}^+]$ ratio [22, 23]. Based on eATRP, Li et al. achieved surface polymerization by surface-initiated electrochemically atom transfer radical polymerization (SI-eATRP) firstly to graft functional polymer brushes on metal substrate [24]. In SI-eATRP system, $\text{Cu}^{\text{II}}\text{L}^{2+}$ catalyst can be electrochemically reduced to $\text{Cu}^{\text{I}}\text{L}^+$ activators to start a controlled polymerization [25]. Nevertheless, SI-eATRP method was not used for surface modification of polymer membrane.

In this study, PAANA was covalently grafted from PES/PES-NH₂ membrane by SI-eATRP method to improve the blood compatibility and hydrophilicity of PES membrane. The growth of polymer brushes was controlled by monomer concentration, electric potential, polymerization time, and modifier concentration. The hydrophilicity and blood compatibility of the modified membrane were investigated by water contact angle and activated partial thromboplastin time, respectively.

2. Experimental

2.1. Chemicals. Polyethersulfone (PES, Ultrason E6020P) and N, N-dimethyl acetamide (DMAc, 93%) were purchased from BASF, Germany. Nitric acid (HNO₃, 65%) and hydrochloric acid (HCl, 37%) were purchased from GuoYao Chemical Reagent Company. Cupric bromide (CuBr₂, 98%) and stannous chloride (SnCl₂, 98%) were purchased from Shanghai Zhongtai Chemical Reagent Company. Sulfuric acid (H₂SO₄, 98%) was purchased from Changliao Chemical Reagent Company. Triethylamine (TEA) was purchased from DaMao Chemical Reagent Factory. Ethanol (CH₃CH₂OH) and anhydrous diethyl ether (C₄H₁₀O) were purchased from KeLong Chemical Reagent Factory. Dibromo butyryl α -Bromoisobutyryl bromide (C₄H₆Br₂O, 98%) and tetramethyl ethylenediamine (TMEDA) were purchased from Aladdin Reagent.

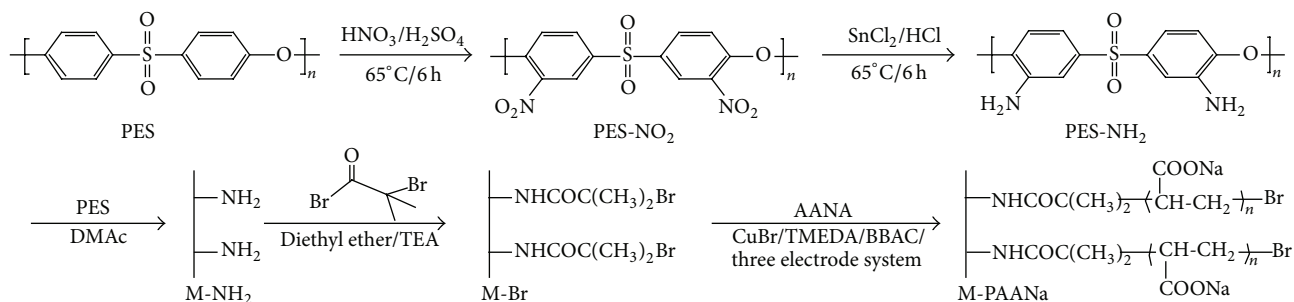
2.2. Amination of PES. Nitric acid (30 mL) and sulfuric acid (40 mL) were mixed in 250 mL flask, and then PES (10 g) was added slowly into the flask when the mixture refrigerated to room temperature. After continuous stirring at 65°C for 6 h, the resulting solution was then washed with deionized water several times. Granular PES-NO₂ was obtained after

vacuum drying for 24 h. 20 g (0.089 mol) stannous chloride was dissolved into 20 g, 37% HCl in a flask, followed by adding 50 mL ethyl alcohol [26]. Then 3 g grinded PES-NO₂ was added slowly into the flask after the mixture was stirred at 65°C for 15 min. The mixture was left to react at 65°C for another 6 h. The resulting precipitate was then washed with deionized water several times when filtering. Brown PES-NH₂ was obtained after vacuum drying for 24 h.

2.3. Preparation of PES/PES-NH₂ Membrane. PES/PES-NH₂ membrane was prepared via classical phase inversion method. Casting solution consists of different amounts of PES, corresponding to different amounts of PES-NH₂ as modifier in 8.2 mL DMAc as solvent, and was stirred for 12 h. The resultant uniform solution was degassed under vacuum at room temperature for 15 min. After that, the casting solution was daubed on a glass substrate, followed by well gluing film machine for homogeneous thickness. Finally, the glass with even solution was thrown into deionized water, and then the casting solution became membrane quickly. The membranes were immersed in deionized water at room temperature for 24 h to remove residual DMAc. Next, Br group was introduced onto the surface of membranes as active sites by nucleophilic substitution reaction between PES-NH₂ and α -Bromoisobutyryl bromide. The process is as follows: 50 mg PES/PES-NH₂ membranes were rinsed in a beaker containing 54 μL triethylamine and 30 mL diethyl ether in ice-water bath. Then, another solution including 0.39 mol α -Bromoisobutyryl bromide and 20 mL diethyl ether was added into previous solution at a rate of one drop per second. The membranes were stirred for another 0.5 h in an ice-water bath after dropping α -Bromoisobutyryl bromide. The resultant solution was stirred at room temperature for 12 h and subsequently was washed successively by diethyl ether, methylbenzene, methyl alcohol, and deionized water. PES/PES-Br membranes were obtained after drying under vacuum for 12 h.

2.4. SI-eATRP Induced Sodium Acrylate Polymerization. The reaction system includes working electrode, counter electrode, and saturated calomel electrode. Electrolyte includes monomer AANa, ligand tetramethylethylenediamine, catalyst copper bromide CuBr₂, and electrolyte benzyltributylammonium chloride BBAC. On the specific scan potential, polymerization of AANa was carried out under $\text{Cu}^{\text{II}}/\text{Cu}^{\text{I}}$ redox-catalyst system. Polymer brushes were grafted on the membrane surface. The scheme diagram of preparation process of the M-PAANA is shown in Scheme 1.

2.5. Characterization. Fourier transform infrared (FTIR) spectra were recorded on a Nicolet 560 (Spectrometer, USA). Morphology images were observed by scanning electron microscopy (SEM) using S-2500C (Hitachi, Japan). Static water contact angles (WCA) were measured by PHS-3C (Precision science co., ShangHai, China). X-ray photoelectron spectroscopy (XPS) was measured by XSAM800 (KRATOS co., Britain). 1 cm² of prepared membrane was pasted on the



SCHEME 1: Schematic diagram for preparation process of the M-PAANa.

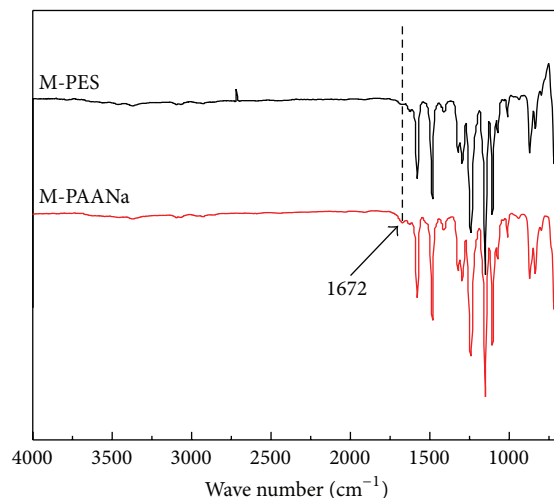


FIGURE 1: ATR-FTIR spectra for the M-PES and M-PAANa.

glass and was scanned by anatomic force microscopy (AFM) to obtain the surface morphology and three dimensional structure (scanning range was $10\ \mu\text{m} \times 10\ \mu\text{m}$) of the prepared membranes.

2.6. Grafting Yield. The grafting yield of PAANa brushes on the M-PES was calculated by (1), where m_0 (mg) and m_1 (mg) are weight before and after grafting PAANa and A is the area of membrane. The last mean result was obtained by three measurements.

$$\text{GY} = \frac{m_1 - m_0}{A} \quad (1)$$

2.7. Hydrophilicity Measurements. The hydrophilic of membrane surface was usually denoted by static water contact angle (WCA). Static water contact angle is a way to characterize the wettability properties of membrane surface [27]. $5\ \mu\text{L}$ water was dripped on the surface of the membrane; at the same time, drip pictures were obtained by lens of microscope and camera, and then the angles were calculated by digital image processing. The last mean result was obtained by three different sites measurements.

2.8. Clotting Time. Antithrombogenicity of the membrane was evaluated by activated partial thromboplastin (APTT), which was measured by an automated blood coagulation analyzer CA-50 (Sysmex Corporation, Kobe, Japan). The

test method is as follows: $0.5\ \text{cm} \times 0.5\ \text{cm}$ of membrane was immersed in 2 mL phosphate buffer saline (PBS, PH = 7.4) solution for 1 h, and then PBS was removed and 0.1 mL platelet-poor plasma (PPP) was added. $50\ \mu\text{L}$ PPP was inhaled in a test cup after incubation at 37°C for 30 min, and $50\ \mu\text{L}$ TT/APTT reagent was added in the test cup at 37°C , followed by incubation for 3 min. Then clotting time was measured and the last mean result was obtained by three measurements.

3. Results and Discussion

The preparation of the M-PAANa is shown in Scheme 1, which mainly included three steps: (i) nitrogroup was introduced to PES macromolecule and transformed to amino to obtain amino-modified PES macromolecules (PES-NH₂); (ii) PES-NH₂ and PES were blended in a certain proportion and proceeded to phase separation to achieve NH₂-grafted PES membrane (M-NH₂), which was then immersed in α -Bromoisobutyryl bromide to acquire membrane initiator (M-Br); and (iii) finally PAANa modified PES membrane (M-PAANa) was prepared by the SI-eATRP method, which was carried out in a three electrode system by using an electrochemical workstation.

Figure 1 shows the ATR-FTIR spectra of the pristine PES membrane (M-PES) and M-PAANa. Compared with the M-PES, the M-PAANa showed a new peak at $1672\ \text{cm}^{-1}$,

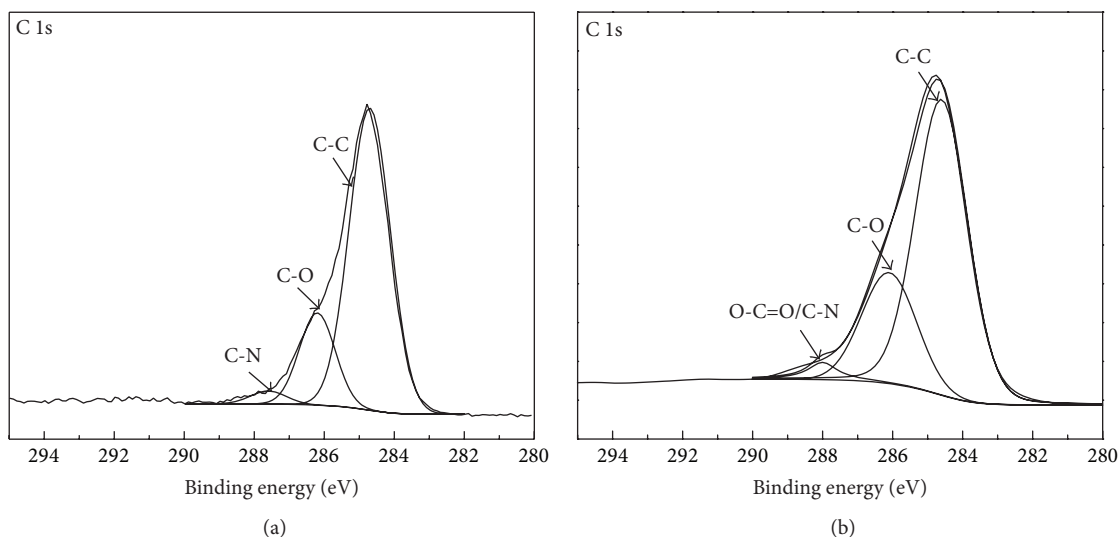


FIGURE 2: The XPS spectra of C 1s for (a) M-PES and (b) M-PAANa.

which was contributed to the antisymmetric stretching vibration band of the carboxyl on AANa structure. These results indicate that PAANa chains have been grafted on the M-PES membrane.

XPS was used to analyze the change of surface compositions of membranes. The XPS spectra of C 1s core-level spectrum are shown in Figure 2. By comparing the XPS spectra between the M-PES and M-PAANa, there were the same peaks of C-O at 286.1 eV, C-C at 284.6 eV, and C-N (C=O) at 288.0 eV at both M-PES and M-PAANa, while the M-PAANa showed a higher peak of C=O at 288.0 eV which was contributed to carboxyl of AANa, also indicating that the PAANa chains were grafted on the membrane.

The AFM images of the M-PES and the M-PAANa are shown in Figure 3. It can be found that the latter sample had an evident peak-valley structure, and there were plenty of particles (20–50 nm) on the surface of M-PAANa compared with M-PES. The roughness R_a increased from 14.4 nm of M-PES (Figure 3(a)) to 29.4 nm of M-PAANa (Figure 3(b)), which was attributed to the PAANa brushes grafted on PES membrane.

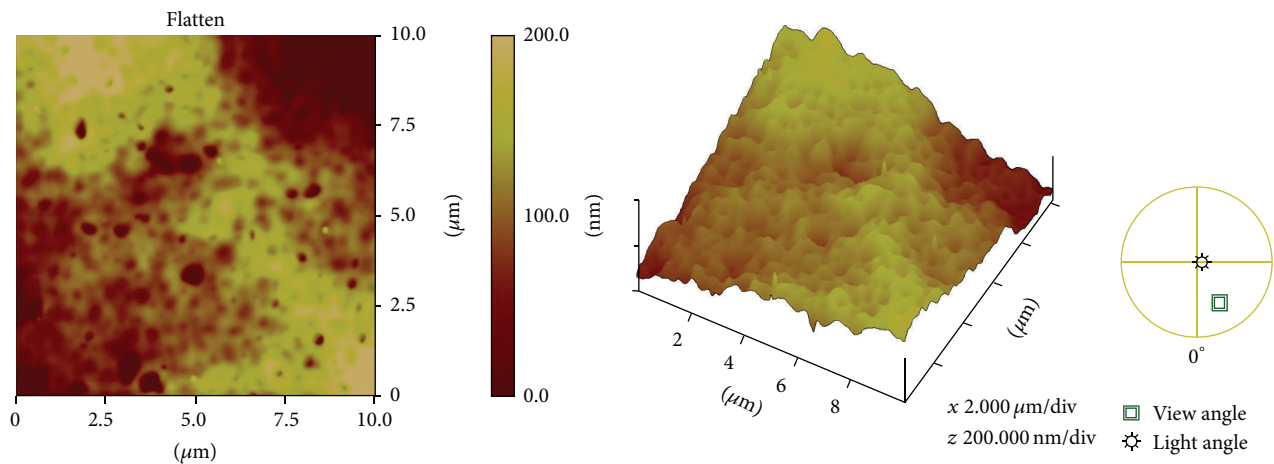
As shown in Figure 4, when the monomer concentration was 0.09 and 0.9 mol/L, the corresponding grafting yield was 0.01 and 0.36 mg/cm², respectively, at the electric potential of -0.12 V for grafting time of 8 h. It is found that the grafting yield of the former was so much lower than the latter, which may be the cause that too little monomer was scattered in the electrolyte which is difficultly grafted to the membrane surface, agreeing with the SEM results. We can see from the SEM images that there were apparent polymer nanoparticles grafted on the surface of the membrane; and the latter sample had more and bigger nanoparticles (about 20 nm) compared with that of former sample (about 3 nm). This indicates that higher concentration of monomer in the SI-eATRP system would show higher grafting degree of the polymer chain and thus thicker polymer coating.

Figure 5 shows the SEM images of M-PAANa prepared with different electric potential of -0.08 , -0.12 , and -0.2 V. By calculation, we found that their corresponding grafting yields were 0.11, 0.36, and 0.24 mg/cm² at the grafting time of 8 h, modifier concentration was 2 wt.%, and the monomer concentration was 0.9 mol/L. It can be also seen from the figure that distribution of nanoparticles was uniform and the amount of nanoparticles agreed with the result from grafting yield.

The M-PAANa was also prepared by controlling the polymerization time from 15 min to 8 h. The grafting yields were increased from 0.04 to 0.12, 0.3, and 0.36 mg/cm² when the reaction time increased from 15 min to 0.5, 1, and 8 h, respectively. Figure 6 presents the SEM images of M-PAANa prepared at different grafting time. It can be seen from the figure that the amount of nanoparticles grafted on the membrane surface increased obviously with the reaction time. In addition, there was no further obvious increase of grafted polymer through further prolonging reaction time after 1 h.

The modifier concentration during the membrane preparation process also plays an important role in controlling the graft degree. Figure 7 shows the SEM images of M-PAANa by different modifier concentrations of 0.8, 2, and 5 wt.%. As shown in the picture too low modifier concentration (0.8 wt.%) resulted in the low graft degree of the polymer brushes; and too high modifier concentration (5 wt.%) generated many macrovoids on the membrane surface. Moreover, their corresponding grafting yields were calculated to be 0.07, 0.36, and -0.02 mg/cm², consistent with the result obtained in the SEM characterization.

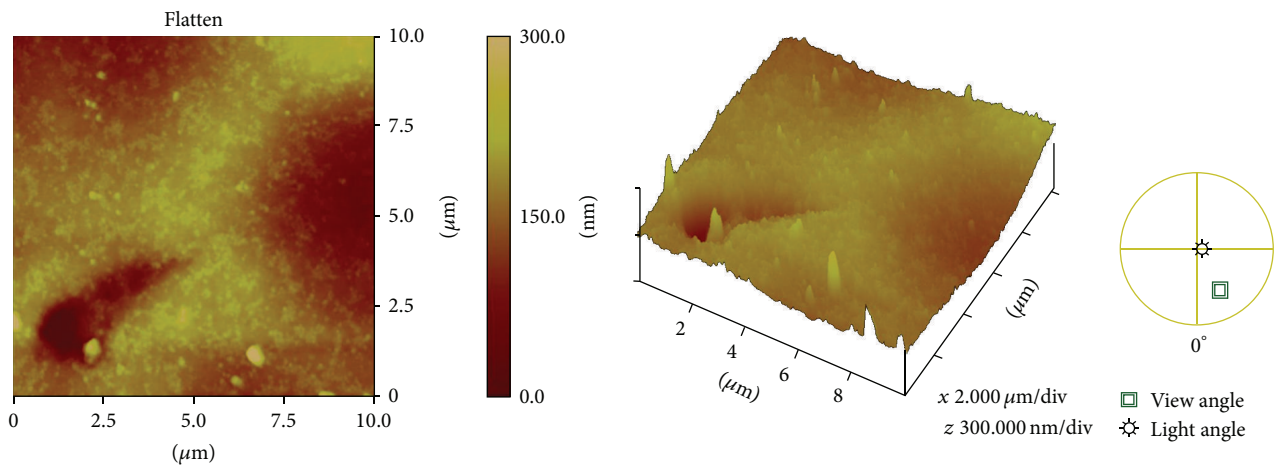
To sum up, the grafting of ion polymer chains on membrane surface can be carried out by SI-eATRP method, and the density and length of PAANa brushes can be easily controlled by the polymerization condition, such as monomer concentration, electric potential, time of SI-eATRP reaction, and modifier concentration.



Digital instruments: nanoscope
 Scan size: 10.00 μm
 Scan rate: 1.001 Hz
 Number of samples: 256
 Image data: height
 Data scale: 200.0 nm

Digital instruments: nanoscope
 Scan size: 10.00 μm
 Scan rate: 1.001 Hz
 Number of samples: 256
 Image data: height
 Data scale: 200.0 nm

(a)



Digital instruments: nanoscope
 Scan size: 10.00 μm
 Scan rate: 1.001 Hz
 Number of samples: 256
 Image data: height
 Data scale: 300.0 nm

Digital instruments: nanoscope
 Scan size: 10.00 μm
 Scan rate: 1.001 Hz
 Number of samples: 256
 Image data: height
 Data scale: 300.0 nm

(b)

FIGURE 3: AFM images of (a) M-PES and (b) M-PAANa.

The hydrophilicity of membrane surface was characterized by static water contact angle, which was used to evaluate the wettability of membrane surface. As is shown in Figure 8, the contact angle decreased from 84° of M-PES to 68° of M-PAANa, which was contributed to the hydrophilic carboxyl of AANa. The APTTs were further measured to study the blood compatibility of the modified membrane, as shown in Table 1. It was found that the blood clotting time of M-PAANa increased to 84 s compared with that of the pristine PES membrane, that is, 51 s. Then enhancement of blood compatibility is because of (i) increase of hydrophilicity of

TABLE 1: APTTs for the M-PES and M-PAANa.

Samples	M-PES	M-PAANa
Clotting time (s)	51 ± 5	84 ± 5

the membrane surface and (ii) the grafting of ionic chain on the surface. Based on these results, we can conclude that the grafting method via SI-eATRP method is an effective approach to modify the polymer membranes to improve the surface properties, such as blood compatibility.

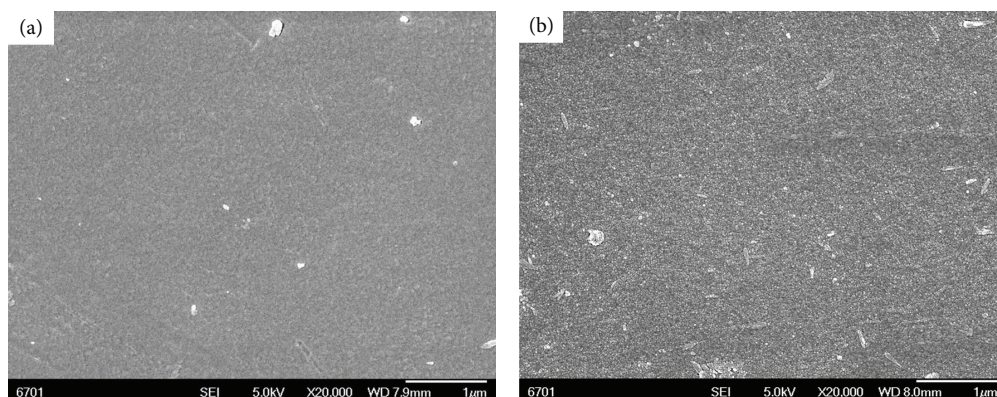


FIGURE 4: SEM images of M-PAANa modified by different monomer concentration: (a) 0.09 mol/L and (b) 0.9 mol/L.

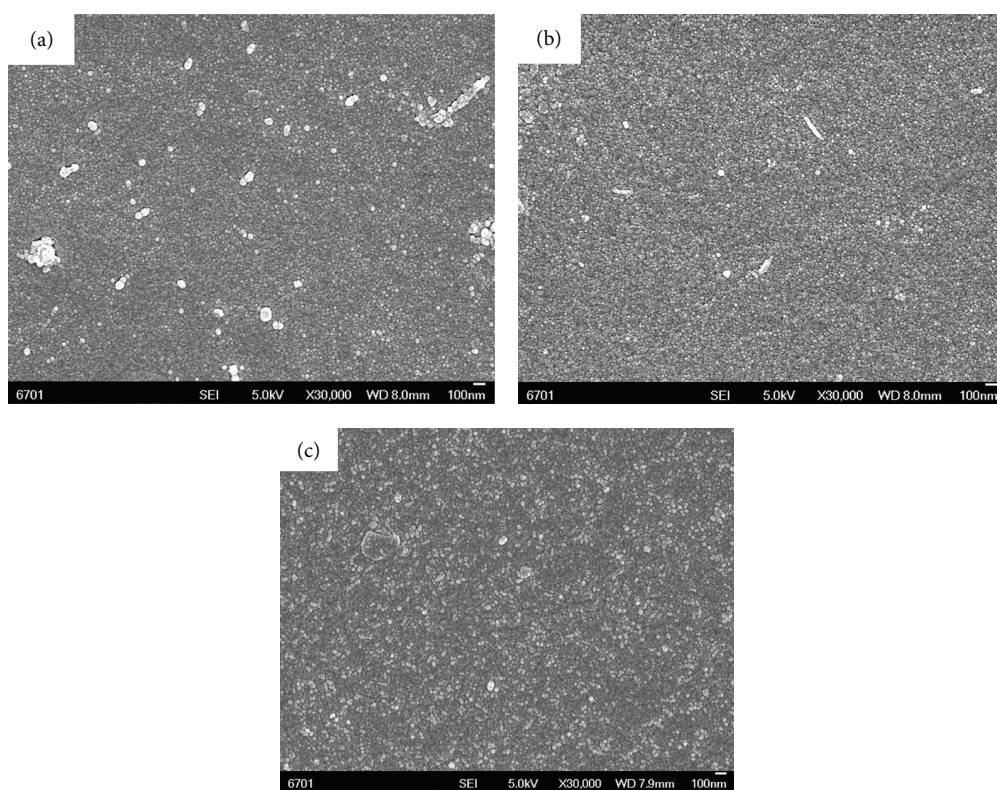


FIGURE 5: SEM images of M-PAANa prepared at different electric potential: (a) -0.08 , (b) -0.12 , and (c) -0.2 V.

4. Conclusions

In this study, polymer brushes were grafted on PES membrane by SI-eATRP method, and the results proved that the modified PES membrane has good hydrophilic and anticoagulation capability compared with those of pristine PES membrane. The water contact angle decreased from 84° to 68° and activated partial thromboplastin increased from

51 s to 84 s. Moreover, the polymerization can be controlled by reaction condition during SI-eATRP process, such as monomer concentration, electric potential, polymerization time, and modifier concentration.

Competing Interests

The authors declare that they have no competing interests.

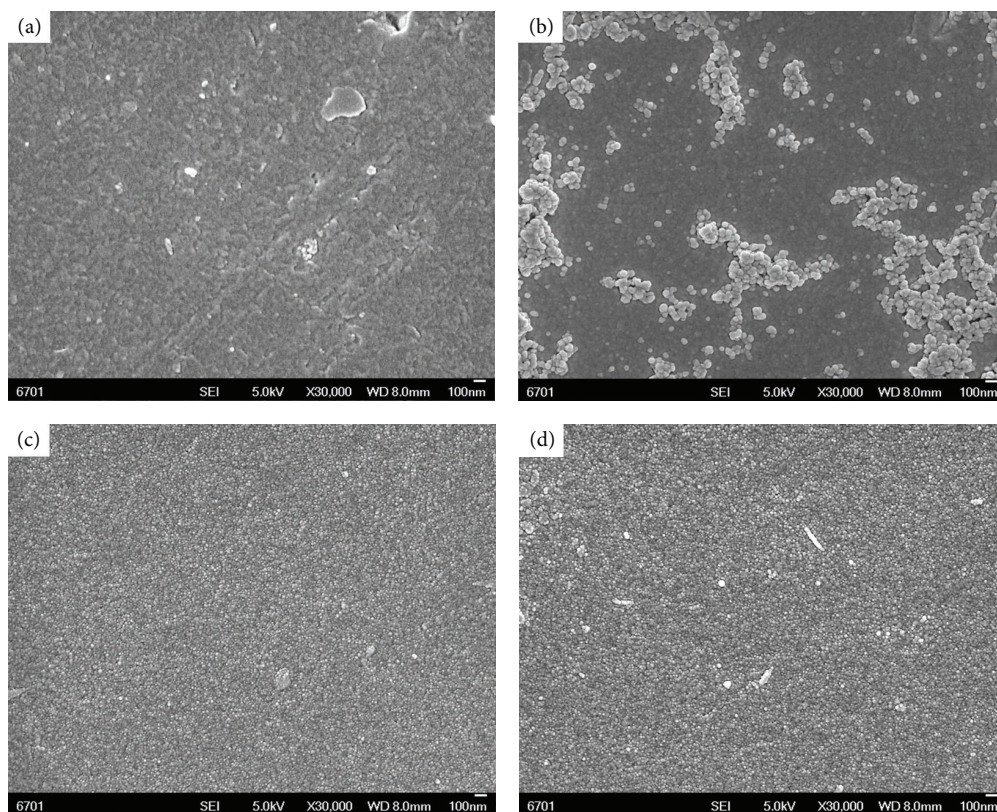


FIGURE 6: SEM images of M-PAANa prepared at different reaction times: (a) 10 min, (b) 0.5 h, (c) 1 h, and (d) 8 h.

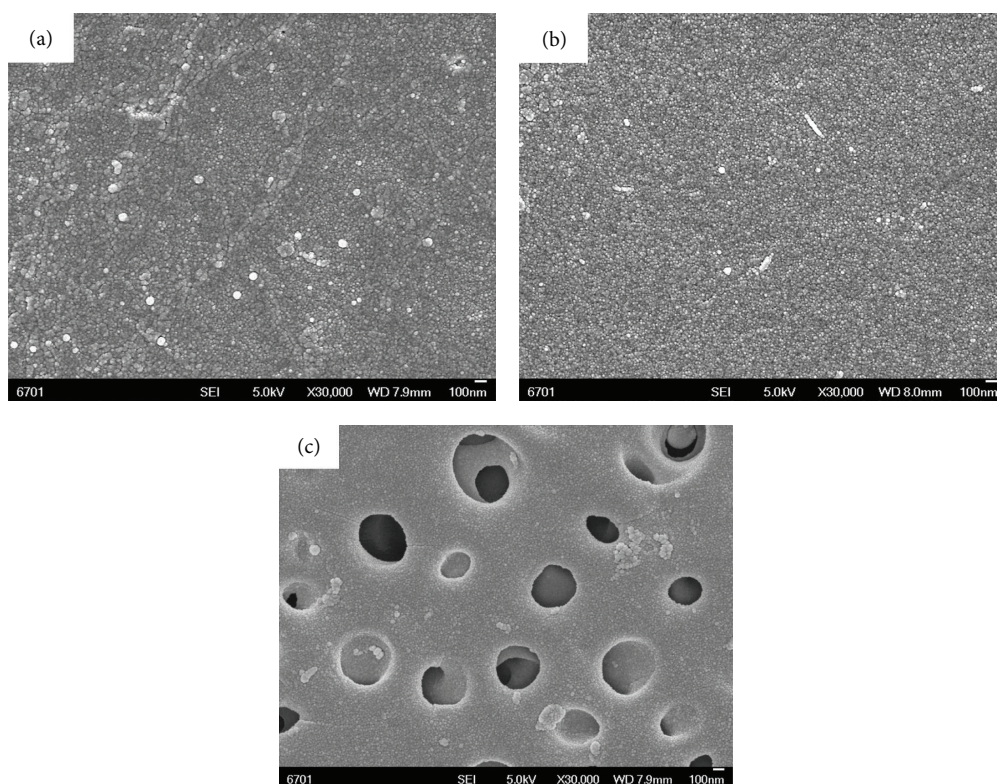


FIGURE 7: SEM images of M-PAANa prepared at different modifier concentrations: (a) 0.8, (b) 2, and (c) 5 wt.%.



FIGURE 8: Water contact angle of (a) M-PES and (b) M-PAANa.

References

- [1] T. Xiang, W.-W. Yue, R. Wang, S. Liang, S.-D. Sun, and C.-S. Zhao, "Surface hydrophilic modification of polyethersulfone membranes by surface-initiated ATRP with enhanced blood compatibility," *Colloids & Surfaces B: Biointerfaces*, vol. 110, pp. 15–21, 2013.
- [2] Q. Wei and R. Haag, "Universal polymer coatings and their representative biomedical applications," *Materials Horizons*, vol. 2, no. 6, pp. 567–577, 2015.
- [3] K. A. Heyries, L. J. Blum, and C. A. Marquette, "Direct poly(dimethylsiloxane) surface functionalization with vinyl modified DNA," *Chemistry of Materials*, vol. 20, no. 4, pp. 1251–1253, 2008.
- [4] C. Zhao, Q. Wei, K. Yang, X. Liu, M. Nomizu, and N. Nishi, "Preparation of porous polysulfone beads for selective removal of endocrine disruptors," *Separation & Purification Technology*, vol. 40, no. 3, pp. 297–302, 2004.
- [5] X.-J. Huang, D. Guduru, Z.-K. Xu, J. Vienken, and T. Groth, "Blood compatibility and permeability of heparin-modified polysulfone as potential membrane for simultaneous hemodialysis and LDL removal," *Macromolecular Bioscience*, vol. 11, no. 1, pp. 131–140, 2011.
- [6] F. Ran, S. Q. Nie, J. Li, B. H. Su, S. D. Sun, and C. S. Zhao, "Heparin-like macromolecules for the modification of anticoagulant biomaterials," *Macromolecular Bioscience*, vol. 12, no. 1, pp. 116–125, 2012.
- [7] J. Y. Park, M. H. Acar, A. Akthakul, W. Kuhlman, and A. M. Mayes, "Polysulfone-graft-poly(ethylene glycol) graft copolymers for surface modification of polysulfone membranes," *Biomaterials*, vol. 27, no. 6, pp. 856–865, 2006.
- [8] P.-S. Liu, Q. Chen, S.-S. Wu, J. Shen, and S.-C. Lin, "Surface modification of cellulose membranes with zwitterionic polymers for resistance to protein adsorption and platelet adhesion," *Journal of Membrane Science*, vol. 350, no. 1-2, pp. 387–394, 2010.
- [9] C. Cheng, S. Li, W. F. Zhao et al., "The hydrodynamic permeability and surface property of polyethersulfone ultrafiltration membranes with mussel-inspired polydopamine coatings," *Journal of Membrane Science*, vol. 417-418, pp. 228–236, 2012.
- [10] B. Kaeselev, J. Pieracci, and G. Belfort, "Photoinduced grafting of ultrafiltration membranes: comparison of poly(ether sulfone) and poly(sulfone)," *Journal of Membrane Science*, vol. 194, no. 2, pp. 245–261, 2001.
- [11] D. Tyszler, R. G. Zytner, A. Batsch et al., "Reduced fouling tendencies of ultrafiltration membranes in wastewater treatment by plasma modification," *Desalination*, vol. 189, no. 1-3, pp. 119–129, 2006.
- [12] W. W. Yue, H. J. Li, T. Xiang et al., "Grafting of zwitterion from polysulfone membrane via surface-initiated ATRP with enhanced antifouling property and biocompatibility," *Journal of Membrane Science*, vol. 446, no. 11, pp. 79–91, 2013.
- [13] J. S. Wang and K. Matyjaszewski, "Controlled/'living' radical polymerization. atom transfer radical polymerization in the presence of transition-metal complexes," *Journal of the American Chemical Society*, vol. 117, no. 20, pp. 5614–5615, 1995.
- [14] J.-S. Wang and K. Matyjaszewski, "Controlled/'living' radical polymerization. Halogen atom transfer radical polymerization promoted by a Cu(I)/Cu(II) redox process," *Macromolecules*, vol. 28, no. 23, pp. 7901–7910, 1995.
- [15] A. Mühlebach, S. G. Gaynor, and K. Matyjaszewski, "Synthesis of amphiphilic block copolymers by atom transfer radical polymerization (ATRP)," *Macromolecules*, vol. 31, no. 18, pp. 6046–6052, 1998.
- [16] D. J. Siegwart, J. K. Oh, and K. Matyjaszewski, "ATRP in the design of functional materials for biomedical applications," *Progress in Polymer Science*, vol. 37, no. 1, pp. 18–37, 2012.
- [17] J. Pyun, T. Kowalewski, and K. Matyjaszewski, "Synthesis of polymer brushes using atom transfer radical polymerization," *Macromolecular Rapid Communications*, vol. 24, no. 18, pp. 1043–1059, 2003.
- [18] N. V. Tsarevsky and K. Matyjaszewski, "'Green' atom transfer radical polymerization: from process design to preparation of well-defined environmentally friendly polymeric materials," *ChemInform*, vol. 38, no. 36, 2007.
- [19] N. V. Tsarevsky, T. Pintauer, and K. Matyjaszewski, "Deactivation efficiency and degree of control over polymerization in ATRP in protic solvents," *Macromolecules*, vol. 37, no. 26, pp. 9768–9778, 2004.
- [20] S. Coca, C. B. Jasieczek, K. L. Beers, and K. Matyjaszewski, "Polymerization of acrylates by atom transfer radical polymerization. Homopolymerization of 2-hydroxyethyl acrylate," *Journal of Polymer Science, Part A: Polymer Chemistry*, vol. 36, no. 9, pp. 1417–1424, 1998.
- [21] M. Salami-Kalajahi, V. Haddadi-Asl, S. Rahimi-Razin, F. Behboodi-Sadabad, H. Roghani-Mamaqani, and M. Hemmati,

- “Investigating the effect of pristine and modified silica nanoparticles on the kinetics of methyl methacrylate polymerization,” *Chemical Engineering Journal*, vol. 174, no. 1, pp. 368–375, 2011.
- [22] N. Bortolamei, A. A. Isse, A. J. D. Magenau, A. Gennaro, and K. Matyjaszewski, “Controlled aqueous atom transfer radical polymerization with electrochemical generation of the active catalyst,” *Angewandte Chemie—International Edition*, vol. 50, no. 48, pp. 11391–11394, 2011.
- [23] T. S. Hansen, J. U. Lind, A. E. Daugaard, S. Hvilsted, T. L. Andresen, and N. B. Larsen, “Complex surface concentration gradients by stenciled ‘electro click chemistry,’” *Langmuir*, vol. 26, no. 20, pp. 16171–16177, 2010.
- [24] B. Li, B. Yu, W. T. Huck, F. Zhou, and W. M. Liu, “Electrochemically induced surface-initiated atom-transfer radical polymerization,” *Angewandte Chemie*, vol. 124, no. 21, pp. 5182–5185, 2012.
- [25] K. Matyjaszewski, H. Dong, W. Jakubowski, J. Pietrasik, and A. Kusumo, “Grafting from surfaces for ‘everyone’: ARGET ATRP in the presence of air,” *Langmuir*, vol. 23, no. 8, pp. 4528–4531, 2007.
- [26] D. Wang, X. Zhang, S. Nie et al., “Photoresponsive surface molecularly imprinted poly(ether sulfone) microfibers,” *Langmuir*, vol. 28, no. 37, pp. 13284–13293, 2012.
- [27] A. Nabe, E. Staude, and G. Belfort, “Surface modification of polysulfone ultrafiltration membranes and fouling by BSA solutions,” *Journal of Membrane Science*, vol. 133, no. 1, pp. 57–72, 1997.

Research Article

Fish Collagen Promotes the Expression of Genes Related to Osteoblastic Activity

Mark Luigi Fabian Capati, Ayako Nakazono, Kohei Yamamoto, Kouji Sugimoto, Kajiro Yanagiguchi, Shizuka Yamada, and Yoshihiko Hayashi

Department of Cariology, Nagasaki University Graduate School of Biomedical Sciences, Nagasaki 852-8588, Japan

Correspondence should be addressed to Yoshihiko Hayashi; hayashi@nagasaki-u.ac.jp

Received 5 July 2016; Accepted 25 August 2016

Academic Editor: Yin Chen

Copyright © 2016 Mark Luigi Fabian Capati et al. This is an open access article distributed under the Creative Commons Attribution License, which permits unrestricted use, distribution, and reproduction in any medium, provided the original work is properly cited.

Tilapia type I atelocollagen (TAC) is a strong candidate for clinical application as its biological scaffold due to a high degeneration temperature and biologically safe properties. The aim of this study was to confirm the biological effects of TAC *in vitro* on osteoblastic cells, simulating its clinical application. The proliferation and differentiation of typical preosteoblasts, MC3T3-E1 cells, were investigated using a microarray analysis, staining assay for mineralization, and real-time PCR analysis of the expression of mineralization-related genes. The mRNA expression of 10 genes involved in proliferation and differentiation increased after 3-day culture on an TAC gel, with an average balanced score ratio exceeding 1.5 compared to the control. After two weeks of culture, all three experimental groups showed stronger alkaline phosphatase staining than after one week. The genes expression of alkaline phosphatase, osteocalcin, and bone sialoprotein increased under the experimental conditions. The gene expression of osteopontin did not increase, and no statistical differences were noted among the three experimental groups. The present and previous findings suggest that TAC is not only a suitable alternative to collagen products originating from mammals but also a novel biomaterial with cell differentiation ability for regenerative medicine.

1. Introduction

The research and development of nonmammalian natural biomaterials will improve the safety of scaffold and carrier in regenerative medicine, which are meaningful and beneficial, due to the global prevalence of dangerous infectious diseases (zoonosis) such as bovine spongiform encephalopathy, avian and swine influenza, tooth-and-mouth disease in cows, pigs, and buffalos, Ebola hemorrhagic fever, and Zika fever [1]. Furthermore, collagen generated from porcine and bovine sources cannot be used due to religious objections in some countries. Fish, which are the most genetically distant relatives from mammals, have recently attracted attention as an alternative source of collagen. Fish collagen (FC) derived from the scales, skin, and bone has interested many laboratories worldwide for its bioactive properties, such as excellent biocompatibility, low antigenicity, high biodegradability, and cell proliferation potential [2, 3].

The weakest point of fish collagen is its relatively low denaturation temperature (T_d), which indicates a poor stability in clinical applications. However, our recent experiment using calorimetry revealed that T_d of collagen solution derived from the tropical fish, tilapia (tilapia type I atelocollagen [TAC]), was 35–36°C [4], indicating that the abovementioned weak point has been completely overcome. In addition, the biological safety of TAC has been confirmed using various test methods recommended with ISO standards [5]. The long-term storage of TCA under frozen conditions for over 1 year has already been demonstrated in our laboratory (unpublished data). These data and findings strongly support TAC as a candidate for clinical application as a biological scaffold.

In the present experiment, we confirmed the biological effects of TAC *in vitro* on osteoblastic cells simulating its clinical application as a suitable alternative to collagen products

TABLE 1: Primers designed for RT-PCR analyses of genes related to cell proliferation and differentiation.

Gene name	Oligonucleotides
Matrix metalloproteinase 13 (Mmp13)	Forward: AGGCCTTCAGAAAAGCCTTC Reverse: GGTCCTTGGAGTGATCCAGA
Wnt inhibitory factor 1 (Wif1)	Forward: GAGTGTCCGGATGGGTCTA Reverse: TGGTTGAGCAGTTTGCTTTG
Receptor activity modifying protein 1 (Ramp1)	Forward: GCGGTATCCTCCTGAAAACA Reverse: CAGTCCTCCAGTTGGACCAT
SMAD family member 6 (Smad6)	Forward: ACGGTGACCTGCTGTCTCTT Reverse: AGCGAGTACGTGACCGTCTT
Platelet-derived growth factor, D polypeptide (Pdgfd)	Forward: TCAGCTGTGTGCTCAACAAA Reverse: ATTGGGCCTGGCTTACTTCT
Chordin-like 1 (Chrd1)	Forward: TGGTCTTTGCTTTCCCATGT Reverse: CCCAGGTGTTCTCTGAAAGC
Septin 4 (Sept4)	Forward: TTCAGGTCCAAAAGCCAGTT Reverse: TGACTTCCCTATCCCTGCTG
Fibroblast growth factor receptor 3 (Fgfr3)	Forward: ACAAGGACCGTACTGCCAAG Reverse: ACCTGGTAGGCACAGGACAC
Lumican (Lum)	Forward: TTCTCTCTTGCCTTGGCATT Reverse: CACTGCAGGTCTGTGACGTT
Vitamin D receptor (Vdr)	Forward: CGGAAATGGGTACCAAAATG Reverse: CACGTAGCAAGCGCTATGAA
Ribosomal protein S17 (rpS17)	Forward: GCATATCATGCAACGCTTTC Reverse: GGAGCTTCAGCATCTCCTTG

originating from mammals. The proliferation and differentiation of MC3T3-E1 cells, which are typical preosteoblasts, were investigated using a microarray analysis, staining assay for mineralization, and real-time PCR analysis (RT-PCR) to determine the expression of calcification-related genes.

2. Materials and Methods

2.1. Cell Culture for Passage. The used MC3T3-E1 cells derived from mouse calvaria were the typical preosteoblasts. They were cultured in a 100 mm dish at a density of 1.5×10^6 cells in α -MEM (Gibco, Palo Alto, CA, USA) with 10% fetal bovine serum (FBS) (MP Biomedicals, Santa Ana, CA, USA) and penicillin-streptomycin (Life Technologies, Carlsbad, CA, USA) and then incubated [6].

2.2. The Dissolution of TAC. TAC (0.6%) produced by solubilized tilapia skin was supplied by Nippi Inc., Biomatrix Institute (Ibaraki, Japan). A diluted 0.1% TAC solution in 1.5-fold concentration PBS (-) (pH 7.4) was used for the biological experiments.

2.3. Total RNA Isolation for Microarray. For FC gel group, 1 mL of 0.1% TAC was added to a 60 mm culture dish. TCA solution was gelled at 37°C for 30 min in a condition of 5% CO₂ and air. MC3T3-E1 cells were seeded in a 60 mm culture dish covered with or without TAC gel at a density of 1.5×10^6 cells. After 3-day culture, total RNA from cells was isolated

using TRIzol reagent (1 mL/10 cm²) (Invitrogen, Carlsbad, CA, USA) and purified in accordance with the manufacturer's instructions [6].

2.4. Microarray of Gene Expression for Checking Proliferation and Differentiation [6]. The cRNA was amplified and hybridized to an Affinity Mouse Genome 430 2.0 array (for 39,000 transcriptional products), scanned by an Affymetrix scanner, and calculated using the Affymetrix Expression Console™.

2.5. Filter Criteria for Data Analysis [6]. We then established the criteria for upregulated genes (Z score > 3.0, ratio > 1.5-fold).

2.6. RT-PCR following Microarray. The MC3T3-E1 cells were seeded and cultured ($n = 3$ for FC group, $n = 3$ for control group) under the same conditions as in the experiment for total RNA isolation for microarray. The primers are indicated in Table 1. The analyses of RT-PCR were carried out according to the similar methods to our recent study [6], except the following two steps. The first was that the protocol of amplification and quantification was 40 cycles (58-59°C, 1 min). The second was that, in the final calculations, the data were normalized by ribosomal protein S17.

2.7. Alkaline Phosphatase (ALP) Staining. For the FC gel group, 90 μ L of 0.1% TAC was poured into each well. TCA solution was gelled at 37°C for 30 min in an atmosphere of

TABLE 2: Primers designed for RT-PCR analyses of gene related to calcification.

Gene name	Oligonucleotides
Alkaline phosphatase (ALP)	Forward: GTTGCCAAGCTGGGAAGAACAC Reverse: CCCACCCCGCTATTCCAAAC
Osteopontin (OPN)	Forward: CATTGCCTCCTCCCTCCCGGTG Reverse: GCTATCACCTCGGCCGTTGGGG
Osteocalcin (OCN)	Forward: AGGGAGGATCAAGTCCCG Reverse: GAACAGACTCCGGCGCTA
Bone sialoprotein (BSP)	Forward: TGTCTGCTGAAACCCTTC Reverse: GGGGTCTTTAAGTACCGGC
Ribosomal protein S17 (rpS17)	Forward: GCATATCATGCAACGCTTTC Reverse: GGAGCTTCAGCATCTCCTTG

5% CO₂ and air. The MC3T3-E1 cells were cultured in a 24-well plate at a density of 5×10^4 cells/well and incubated for 1 or 2 weeks. The following four groups ($n = 3$ wells for each group and each week) were designed for comparison: (1) the control group (culture medium: α -MEM with FBS), (2) FC-positive group (culture medium: α -MEM with FBS), (3) FC-negative and BGP-positive group {culture medium: α -MEM supplemented with FBS, 50 μ g/mL ascorbic acid (Wako, LTD., Osaka, Japan), and 10 mM β -glycerophosphate ([BGP] nakarai tesque, Kyoto, Japan)}, (4) FC-positive and BGP-positive group (culture medium: α -MEM with FBS, 50 μ g/mL ascorbic acid, and 10 mM BGP). The medium was renewed every three days. The ALP Staining Kit (Stemgent, Inc., Cambridge, MA, USA) was used to stain for ALP expression in accordance with the maker's instructions.

2.8. RT-PCR for Calcification-Related Genes. For the FC gel group, 1 mL of 0.1% TAC was added to a 60 mm culture dish. TCA solution was gelled at 37°C for 30 min in a condition of 5% CO₂ and air. MC3T3-E1 cells were seeded in a 60 mm culture dish covered with or without TAC gel at a density of 1.5×10^6 cells. The abovementioned four groups were also prepared for this experiment ($n = 3$ for each group). After three days of culture, RT-PCR was applied to check the expression of four calcification-related genes: ALP, osteopontin (OPN), osteocalcin (OCN), and bone sialoprotein (BSP). All the methods were similar to the abovementioned methods. The primer designs for these genes are represented in Table 2.

2.9. Statistical Analyses. All data were represented as the mean \pm standard deviation (SD). The statistical significance ($P < 0.05$) of the differences between the two different experimental groups was demonstrated using a paired Student's *t*-test.

3. Results

3.1. Genes Expression to Proliferation and Differentiation. Microanalysis revealed 72 of the upregulated genes (Z score > 3.0). The following 10 genes related to proliferation and differentiation of osteoblastic cells were compared with the control using the RT-PCR: vitamin D receptor (Vdr), lumican (Lum), matrix metalloproteinase 13 (Mmp13), SMAD family

TABLE 3: Genes expression represented in cell proliferation and differentiation.

Gene name	Z score	Ratio ^a	Confirmation ^b
Vdr	3.9	1.6	1.5
Lum	4.9	1.7	1.5
Mmp13	12.2	4.4	3.5
Smad6	3.7	1.5	2.0
Pdgfd	3.4	1.5	1.6
Wif1	6.3	2.0	5.1
Fgfr3	4.8	1.7	2.0
Sept4	6.5	2.1	2.3
Ramp1	4.3	1.6	3.2
Chrd11	6.0	1.9	3.9

^aThe change raw signal ratio. ^bConfirmed by the RT-PCR data (triplicate samples).

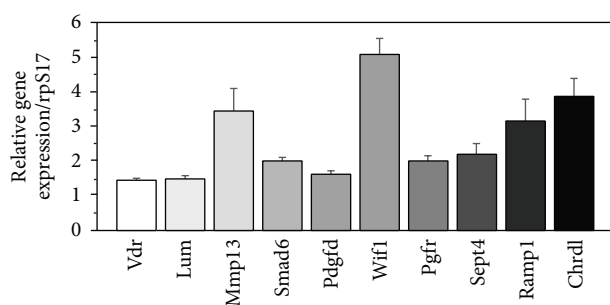


FIGURE 1: RT-PCR for 10 genes in relation to cell proliferation and differentiation. Each bar indicates the SD of triplicate samples.

member 6 (Smad6), platelet-derived growth factor D (Pdgfd), Wnt inhibitory factor 1 (Wif1), fibroblast growth factor receptor 3 (Fgfr3), septin 4 (Sept4), receptor (calcitonin) activity modifying protein 1 (Ramp1), and chordin-like 1 (Chrd11) (Table 3). The RT-PCR analyses revealed that the mRNA expression of these 10 genes also increased after 3-day culture on FC gel, with an average balanced score ratio exceeding 1.5 compared to the control (Figure 1).

3.2. Alkaline Phosphatase Staining (Figure 2). In group (1) after 2 weeks of culture, very-weak-intensity ALP staining

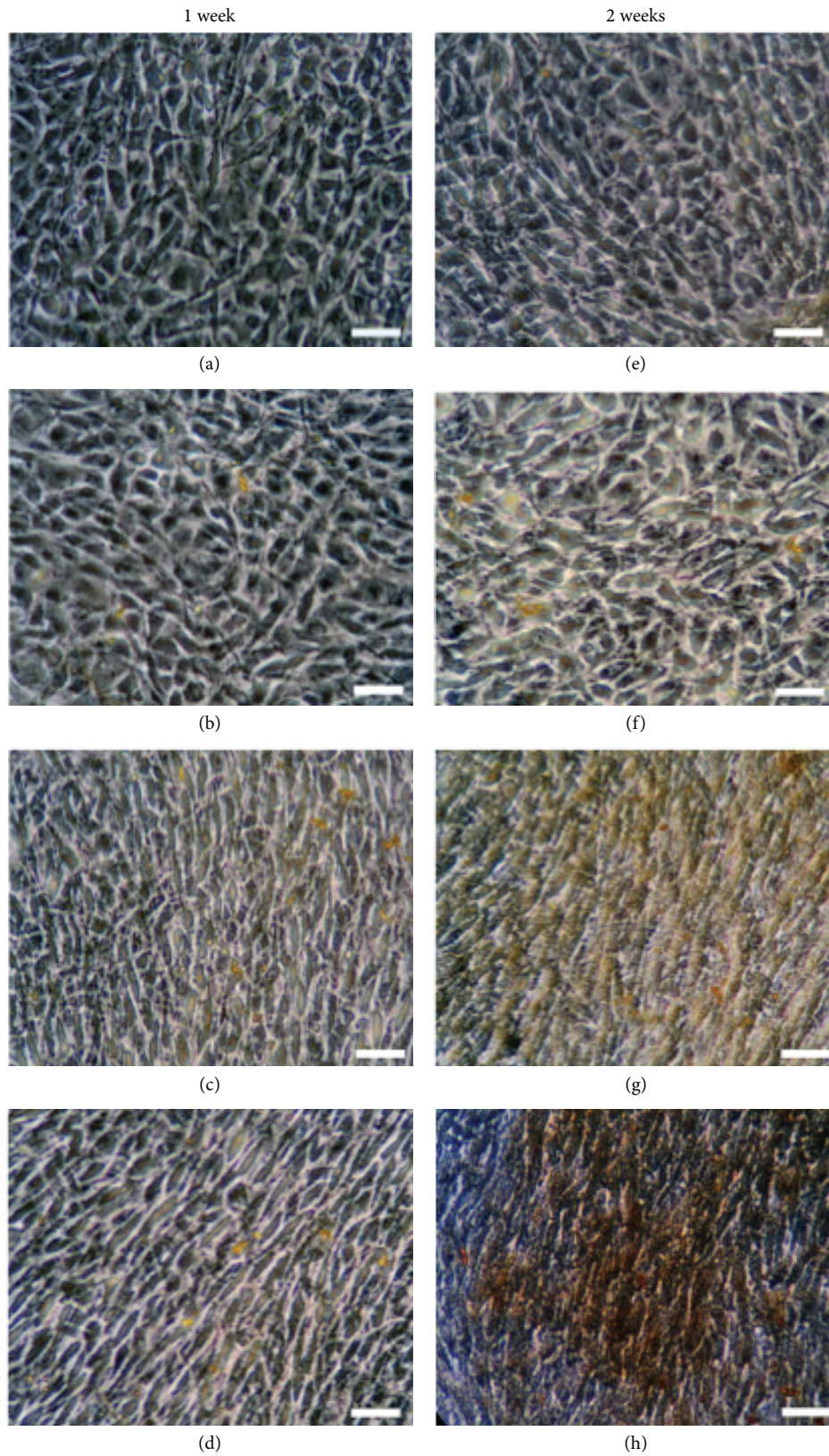


FIGURE 2: Representative ALP staining photographs after one or two weeks of culture: (a, e) FC-negative group, (b, f) FC-positive group, (c, g) FC-negative and BGP-positive group, and (d, h) FC-positive and BGP-positive group. ALP staining shows either a yellow or brown color. Although the typical pavement-like shape is observed at (a), (e), and (b), (f), on the whole, the cell morphology changes to a spindle-like cell shape (c, g, and d, h). Scale bar = 15 μm .

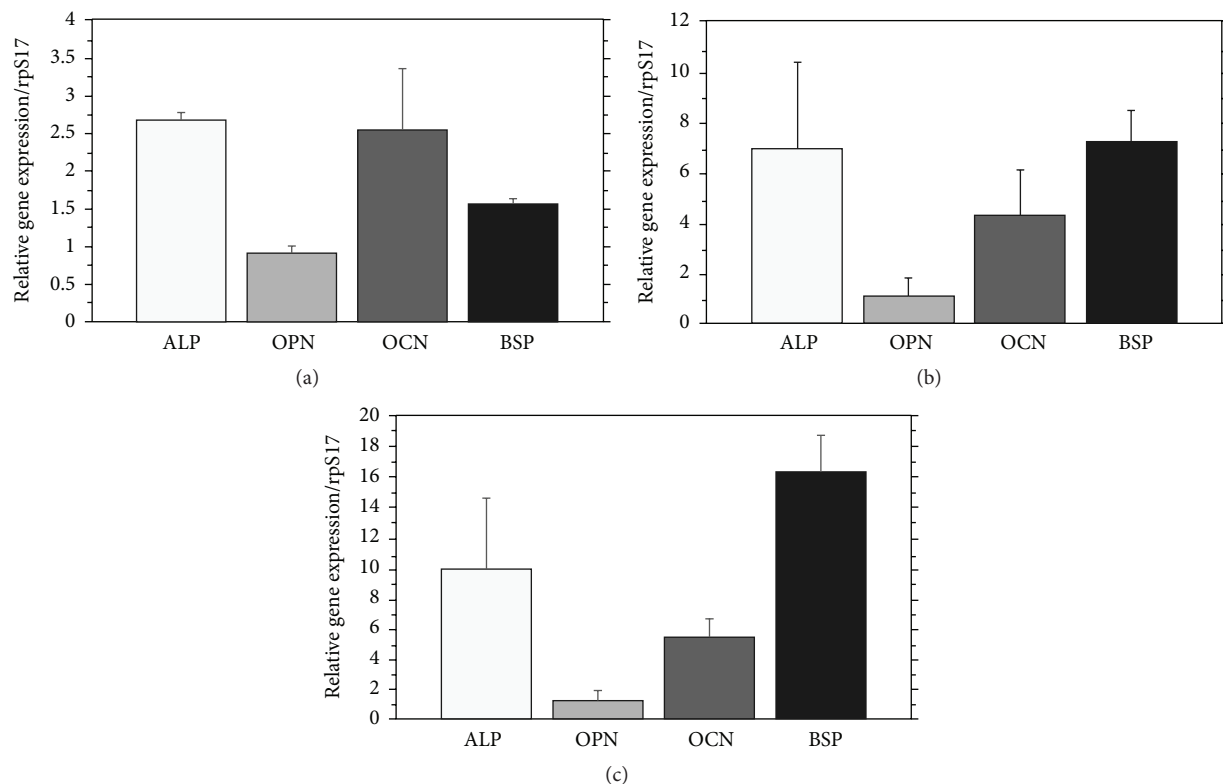


FIGURE 3: RT-PCR for four calcification-related genes: (a) FC-positive group (group 2), (b) FC-negative and BGP-positive group (group 3), and (c) FC-positive and BGP-positive group (group 4). Each bar represents the SD of triplicate samples.

was observed, similar to that in group (2) after 1 week. After 2 weeks of culture, each group showed stronger staining than after 1 week. On the whole, the spindle-like shape was observed in groups (3) and (4) (Figures 2(c), 2(g), and 2(d), 2(h)). The intensity of staining increased with increasing group number from group (2) to group (4).

3.3. Gene Expression for Calcification. The RT-PCR analyses demonstrated that the mRNA expression of four calcification-related genes in three experimental groups was analyzed after 3-day culture, compared to the control group (1) (Figure 3). Although the gene expression of ALP, OCN, and BSP increased with increasing group number from group (2) to group (4), a significant increase was recognized in BSP gene expression ($P < 0.01$). The raw data of OPN expression of OPN was around 1.0 in three groups, although there was a significant increase between group (2) and group (3) ($P < 0.05$).

4. Discussion

Cell culture method using the type I collagen gel was first reported by Elsdale and Bard [7]. The cells have well grown within a three-dimensional (3D) structure, as the conditions more closely resemble those of the *in vivo* condition of the osteoblast than the traditional two-dimensional (2D) cultures. Cells growth in 3D gels showed positive mineral staining and induction of osteoblastic marker genes earlier

than cell growth in 2D cultures [8]. Although the present culture conditions were not the exact 3D gel culture system, the present environment was remarkably similar to a 3D culture environment, as a low-concentration TCA solution was gelled to mimic wet and elastic conditions [9].

Microarray and RT-PCR analyses for checking the genes involved in proliferation and differentiation in MC3T3-E1 cells demonstrated that the Z score data using the standard deviations presented the effect of FC on MC3T3-E1 cells more clearly than the original ratio results. Ten genes, including Wif1, a secreted modulator of Wnt proteins [10], increased expressions compared with a control condition. This datum is the first to reveal that FC directly accelerates the activity of MC3T3-E1 cells in order to maintain the preosteoblast nature.

In the present experiment, the function of MC3T3-E1 cells was accelerated after three-day culture in FC-positive or BGP-positive group, which was confirmed by the increase of the expression of calcification-related genes, except OCN. ALP is an early expression marker essential for osteoblast proliferation [11], which was well demonstrated by the present ALP staining findings and the typical change in the cell shape. Furthermore, the time lapse between mRNA expression (3 days) and protein synthesis (7 days) seemed reasonable. Although OPN, OCN, and BSP are generally used as differentiation markers for osteoblasts [11–13], OPN was also reported to act as a mineralization inhibitor to regulate crystal growth [14, 15]. The present PCR data of OPN clearly demonstrated this osteoclastic function of OPN.

Although the intracellular signal transduction pathway and the related gene expression in osteoblast differentiation have been widely investigated [16–22], the direct trigger mechanisms for osteoblast proliferation and differentiation by collagen have not yet been clarified. Recently, an interesting study revealed that adhesion of human mesenchymal stem cells on tilapia collagen *in vitro* was faster and higher than that on porcine collagen or a noncoated surface, probably due to the texture flexibility and surface softness of the tilapia scale collagen, making the binding between collagen and integrin easier to trigger and stimulate both proliferation and differentiation of preosteoblasts [23]. A 0.1% TAC solution was used to make a gel in the present FC group. The nature of this gel is very soft, even after 2 weeks in the CO₂ incubator, and is thought to be possessed of sufficient flexibility and surface softness. This means that cultured cells may also behave as they would in a 3D culture system.

Proper biodegradation and suitable biocompatibility are indispensable for biomaterials. The biodegradation of collagen is closely linked to and dependent on the constitution of amino acids in a given species. Compared to bovine collagen, the contents of methionine, isoleucine, leucine, hydroxylysine, and lysine are lower in TAC [24]. As these amino acids are related to the collagen stiffness, the tilapia collagen can be easily degraded *in vivo*. The characteristics of these amino acids give TAC its abovementioned nature.

From our previous data [4, 5] and the present results, TAC may represent not only a promising alternative to mammalian and avian collagen products but also a novel biomaterial with cell differentiation ability. The final goal with TAC is its clinical application as a scaffold in regenerative medicine. The enzymatic digestion time for atelotreatment and the elimination of enzyme in TAC are controlled to a clinical level (personal communication). The preliminary experimental data concerning pulp regeneration [24] using TAC as a scaffold revealed no rejection reaction on the newly regenerated pulp tissue in dogs (unpublished data). These findings suggest that TAC may be useful for clinical application after further animal experiments.

5. Conclusion

The present *in vitro* experiments using osteoblasts clearly revealed that TAC is not only a suitable alternative to collagen products originating from mammals for cell proliferation and differentiation as the scaffold for regenerative medicine.

Competing Interests

The authors declare no conflicts of interests in association with this study.

Authors' Contributions

Mark Luigi Fabian Capati and Ayako Nakazono contributed equally to this work.

Acknowledgments

This study was supported in part by Funds for Integrated Promotion of Social System Reform and Research and Development, Contract Grant Sponsor: Ministry of Education, Science, Sports, and Culture of Japan.

References

- [1] Y. Hayashi, S. Yamada, T. Ikeda, Z. Koyama, and K. Yanagiguchi, "Chitosan and fish collagen as biomaterials for regenerative medicine," in *Marine Medical Food*, S.-K. Kim, Ed., vol. 65, chapter 6, pp. 107–120, Academic Press, London, UK, 2012.
- [2] A. K. Dillow and A. M. Lowman, *Biomimetic Materials and Design: Biointerfacial Strategies, Tissue Engineering, and Targeted Drug Delivery*, Marcel Dekker, New York, NY, USA, 2002.
- [3] S. Yang, K.-F. Leong, Z. Du, and C.-K. Chua, "The design of scaffolds for use in tissue engineering. Part I. Traditional factors," *Tissue Engineering*, vol. 7, no. 6, pp. 679–689, 2001.
- [4] K. Yamamoto, Y. Yoshizawa, K. Yanagiguchi, T. Ikeda, S. Yamada, and Y. Hayashi, "The characterization of fish (tilapia) collagen sponge as a biomaterial," *International Journal of Polymer Science*, vol. 2015, Article ID 957385, 5 pages, 2015.
- [5] K. Yamamoto, K. Igawa, K. Sugimoto et al., "Biological safety of fish (tilapia) collagen," *BioMed Research International*, vol. 2014, Article ID 630757, 9 pages, 2014.
- [6] M. L. F. Capati, A. Nakazono, K. Igawa et al., "Boron accelerates cultured osteoblastic cell activity through calcium flux," *Biological Trace Element Research*, 2016.
- [7] T. Elsdale and J. Bard, "Collagen substrata for studies on cell behavior," *Journal of Cell Biology*, vol. 54, no. 3, pp. 626–637, 1972.
- [8] B. G. Matthews, D. Naot, K. E. Callon et al., "Enhanced osteoblastogenesis in three-dimensional collagen gels," *Bonekey Reports*, vol. 3, article 560, 2014.
- [9] E. Hesse, T. E. Hefferan, J. E. Tarara et al., "Collagen type I hydrogel allows migration, proliferation, and osteogenic differentiation of rat bone marrow stromal cells," *Journal of Biomedical Materials Research Part A*, vol. 94, no. 2, pp. 442–449, 2010.
- [10] S. W. Cho, J.-Y. Yang, H. J. Sun et al., "Wnt inhibitory factor (WIF)-1 inhibits osteoblastic differentiation in mouse embryonic mesenchymal cells," *Bone*, vol. 44, no. 6, pp. 1069–1077, 2009.
- [11] T. A. Owen, M. Aronow, V. Shalhoub et al., "Progressive development of the rat osteoblast phenotype in vitro: reciprocal relationships in expression of genes associated with osteoblast proliferation and differentiation during formation of the bone extracellular matrix," *Journal of Cellular Physiology*, vol. 143, no. 3, pp. 420–430, 1990.
- [12] J. E. Aubin, F. Liu, L. Malaval, and A. K. Gupta, "Osteoblast and chondroblast differentiation," *Bone*, vol. 17, no. 2, supplement 1, pp. S77–S83, 1995.
- [13] J. B. Lian and G. S. Stein, "Development of the osteoblast phenotype: molecular mechanisms mediating osteoblast growth and differentiation," *The Iowa Orthopaedic Journal*, vol. 15, pp. 118–140, 1995.
- [14] H. Yoshitake, S. R. Rittling, D. T. Denhardt, and M. Noda, "Osteopontin-deficient mice are resistant to ovariectomy-induced bone resorption," *Proceedings of the National Academy of Sciences of the United States of America*, vol. 96, no. 14, pp. 8156–8160, 1999.

- [15] J. Sodek, B. Ganss, and M. D. McKee, "Osteopontin," *Critical Reviews in Oral Biology and Medicine*, vol. 11, no. 3, pp. 279–303, 2000.
- [16] G. S. Stein, J. B. Lian, J. L. Stein, A. J. Van Wijnen, and M. Montecino, "Transcriptional control of osteoblast growth and differentiation," *Physiological Reviews*, vol. 76, no. 2, pp. 593–629, 1996.
- [17] M.-H. Lee, A. Javed, H.-J. Kim et al., "Transient upregulation of CBFA1 in response to bone morphogenetic protein-2 and transforming growth factor β 1 in C2C12 myogenic cells coincides with suppression of the myogenic phenotype but is not sufficient for osteoblast differentiation," *Journal of Cellular Biochemistry*, vol. 73, no. 1, pp. 114–125, 1999.
- [18] K. Miyama, G. Yamada, T. S. Yamamoto et al., "A BMP-inducible gene, *Dlx5*, regulates osteoblast differentiation and mesoderm induction," *Developmental Biology*, vol. 208, no. 1, pp. 123–133, 1999.
- [19] K.-S. Lee, H.-J. Kim, Q.-L. Li et al., "Runx2 is a common target of transforming growth factor β 1 and bone morphogenetic protein 2, and cooperation between Runx2 and Smad5 induces osteoblast-specific gene expression in the pluripotent mesenchymal precursor cell line C2C12," *Molecular and Cellular Biology*, vol. 20, no. 23, pp. 8783–8792, 2000.
- [20] K. Nakashima, X. Zhou, G. Kunkel et al., "The novel zinc finger-containing transcription factor Osterix is required for osteoblast differentiation and bone formation," *Cell*, vol. 108, no. 1, pp. 17–29, 2002.
- [21] M.-H. Lee, Y.-J. Kim, H.-J. Kim et al., "BMP-2-induced Runx2 expression is mediated by *Dlx5*, and TGF- β 1 opposes the BMP-2-induced osteoblast differentiation by suppression of *Dlx5* expression," *Journal of Biological Chemistry*, vol. 278, no. 36, pp. 34387–34394, 2003.
- [22] K. Felber, P. M. Elks, M. Lecca, and H. H. Roehl, "Expression of osterix is regulated by FGF and Wnt/ β -catenin signalling during osteoblast differentiation," *PLoS ONE*, vol. 10, no. 12, Article ID e0144982, 2015.
- [23] R. Matsumoto, T. Uemura, Z. Xu, I. Yamaguchi, T. Ikoma, and J. Tanaka, "Rapid oriented fibril formation of fish scale collagen facilitates early osteoblastic differentiation of human mesenchymal stem cells," *Journal of Biomedical Materials Research A*, vol. 103, no. 8, pp. 2531–2539, 2015.
- [24] Y. Hayashi, T. Ikeda, S. Yamada, Z. Koyama, and K. Yanagiguchi, "The application of fish collagen to the dental and hard tissue regenerative medicine," in *Seafood Processing By-Products: Trends and Applications*, S.-K. Kim, Ed., chapter 22, pp. 455–462, Springer, New York, NY, USA, 2014.

Research Article

The Influence of Irradiation and Accelerated Aging on the Mechanical and Tribological Properties of the Graphene Oxide/Ultra-High-Molecular-Weight Polyethylene Nanocomposites

Guodong Huang, Zifeng Ni, Guomei Chen, and Yongwu Zhao

School of Mechanical Engineering, Jiangnan University, Wuxi, Jiangsu 214122, China

Correspondence should be addressed to Zifeng Ni; nizf@jiangnan.edu.cn and Yongwu Zhao; zhaoyw@jiangnan.edu.cn

Received 28 June 2016; Accepted 11 August 2016

Academic Editor: Yin Chen

Copyright © 2016 Guodong Huang et al. This is an open access article distributed under the Creative Commons Attribution License, which permits unrestricted use, distribution, and reproduction in any medium, provided the original work is properly cited.

Graphene oxide/ultra-high-molecular-weight polyethylene (GO/UHMWPE) nanocomposite is a potential and promising candidate for artificial joint applications. However, after irradiation and accelerated aging, the mechanical and tribological behaviors of the nanocomposites are still unclear and require further investigation. GO/UHMWPE nanocomposites were successfully fabricated using ultrasonication dispersion, ball-milling, and hot-pressing process. Then, the nanocomposites were irradiated by gamma ray at doses of 100 kGy. Finally, GO/UHMWPE nanocomposites underwent accelerated aging at 80°C for 21 days in air. The mechanical and tribological properties of GO/UHMWPE nanocomposites have been evaluated after irradiation and accelerated aging. The results indicated that the incorporation of GO could enhance the mechanical, wear, and antiscratch properties of UHMWPE. After irradiation, these properties could be further enhanced, compared to unirradiated ones. After accelerated aging, however, these properties have been significantly reduced when compared to unirradiated ones. Moreover, GO and irradiation can synergistically enhance these properties.

1. Introduction

Ultra-high-molecular-weight-polyethylene (UHMWPE) is considered as being suitable bearing materials for orthopedic implants [1] because it has excellent properties including good wear resistance, exceptional toughness, a lower friction coefficient, and good biocompatibility [2]. However, during the long-term application process, wear, oxidation, and wear debris accumulation easily result in osteolysis [3] and aseptic loosening [4, 5]. And it ultimately leads to failure of orthopedic implants. In order to increase the longevity of orthopedic implants, much effort has been placed on improving mechanical and tribological properties of UHMWPE. Among most of methods, gamma-irradiation and UHMWPE-based composites are two main methods.

Gamma-irradiation is the usual method for enhancing polymer properties, which not only provides reliable and effective medical sterilization but also can cross-link the

polymer. The free radicals are generated during gamma-irradiation through the scission of C-H and C-C bonds. In the one aspect, free radicals produced by irradiation can form crosslinking by recombining each other in the amorphous phase of polyethylene. As a consequence, wear properties of UHMWPE have been significantly improved [6]. In the other aspect, in crystalline phase of polyethylene, residual free radicals can react with oxygen and result in oxidation degradation of UHMWPE during shelf aging or after implantation [7, 8], which greatly affect mechanical and tribological properties. Therefore, accelerated aging methods are used to evaluate potential for long-term oxidation resistance of the polymer in air. It is crucial for long-lasting artificial joint to understand the influence of irradiation and long-term shelf aging in air on the oxidation of UHMWPE.

In addition to gamma-irradiation, another alternative method is UHMWPE-based composites. Various fillers such

as Graphene [9–11], carbon nanotubes (CNTs) [12], graphite, calcium carbonate (CaCO_3) [13], and wollastonite [14] have been applied to enhance mechanical and antiwear properties of the polymer. Among the above fillers, Graphene is regarded as an ideal reinforcing filler due to its superior mechanical [15] and lubricant properties [16]. However, it is difficult to disperse Graphene in the polymer matrix [17]. As a result, Graphene oxide (GO), which is one of the most important Graphene derivatives, has been widely used to enforce polymer properties due to excellent dispersion in polymer matrix. The incorporation of GO into UHMWPE can significantly improve antiwear and mechanical properties of UHMWPE. For instance, GO/UHMWPE nanocomposites can enhance the hardness, tensile strength, and impact strength of UHMWPE [18–20]. And GO can reduce the wear rate but increase mean friction coefficient of UHMWPE [21, 22]. Moreover, it is also found that the optimum 0.5 wt% GO content for the nanocomposites can effectively improve GO/UHMWPE nanocomposites performance, compared to pure UHMWPE [23]. Although these important results give important insights into GO/UHMWPE nanocomposites, the influence of gamma-irradiation and accelerated aging on antiwear and mechanical properties of GO/UHMWPE nanocomposites has rarely been reported. In this paper, the mechanical and tribological properties of GO/UHMWPE nanocomposites are studied after gamma-irradiation and accelerated aging.

2. Experimental Details

2.1. Sample Preparation Method. UHMWPE powder with a density of 0.93 g/cm has a molecular weight of approximately 5 million. GO is prepared via the modified Hummer's methods [24]. GO/UHMWPE composites with 0.5 wt% GO loading are prepared by following route reported by previous work [25]. In brief, 0.5 g GO powder is dispersed in 200 mL alcohol solution and sonicated for 30 min. Then, 99.5 g UHMWPE powder is dispersed in GO solution and sonicated for another 40 min. Next, the mixture solution is kept in an oven at 60°C until the solvent is completely volatilized. Subsequently, dried powder composites are ball-milled for 2 h at the constant rotation rate of 400 rpm. Afterward, the powder composites are prepressed in the model at 15 MPa for 15 min. Then pressed powder composites are heated for 2 h at 200°C in an air oven. Finally, the powder composites taken out from an air oven are pressed at 10 MPa until their temperature cools to room temperature.

Vacuum-packed samples are irradiated at room temperature by ^{60}Co gamma-rays (WuXi EL PONT Radiation Technology Co., Ltd.) with irradiation doses of 100 kGy.

Accelerated aging process is carried out at 80°C for 21 days in an air oven (according to ASTM F2003-00; ASTM: American Society for Testing and Materials).

The morphology of the surface is observed by Hitachi's S-4800 field emission scanning electron microscopy (SEM).

2.2. Mechanical Properties. The test samples are cut into dumbbell-shaped test specimens according to the ASTM

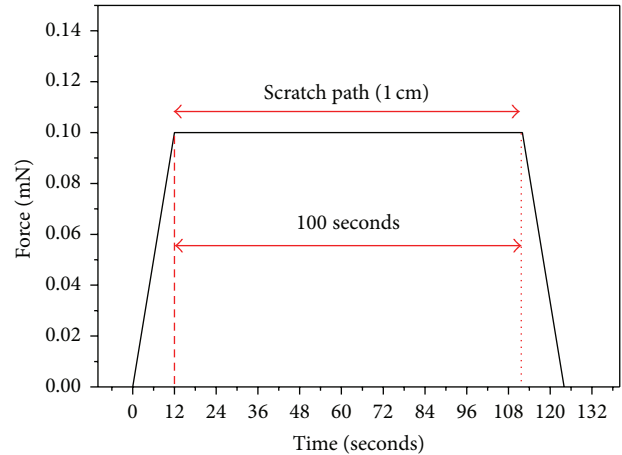


FIGURE 1: The loading-unloading curve in scratching process.

D638 (Type IV; thickness: 3.2 mm). Tensile tests are performed on a tensile machine (WDW-200, Ji'nan Shijin Group Co. Ltd., China) at the crosshead speed of 50 mm/min. At least five specimens are tested for each case. Young's modulus, yield stress, and fracture stress are calculated according to the stress-strain curves.

The ball indentation hardness is measured according to the ISO2039-73 [26, 27] as a referee and the measurements are carried out with Rtec Tribometer (Type: MFT-5000; Rtec Instruments, Inc., USA). The indenter is a Si_3N_4 ball of 5 mm in diameter. The initial applied preload is 9.8 N and the applied test load is 132 N. The measured hardness H can be calculated according to the following equation [27]:

$$H = \frac{P_{\max}}{\pi D h_{\max}}, \quad (1)$$

where P_{\max} is the test force, D is the diameter of the ball, and h_{\max} is the reduced depth of the impression.

2.3. Scratching Test. Scratching testing is performed with Rtec Tribometer (Type: MFT-5000; Rtec Instruments, Inc., USA). Conical diamond tip (1 mm × 5 mm × 60°, 12.5 micron diamond radius) is used to scratch the surface of the samples. The loading-unloading curve is shown in Figure 1. In scratching process, the applied constant load is 0.1 N; the scratch velocity is about 10 mm/s and the scratch length is set at 10 mm. The residual depth of the scratch is measured by Rtec Profilometer (Type: MFD-D; Rtec Instruments, Inc., USA). The friction coefficient (μ) is calculated according to the following equation:

$$\mu = \frac{F_T}{F_N}, \quad (2)$$

where F_N is normal force and F_T is lateral force. Scratch causing wear resistance of test samples is assessed by measuring the volume loss by Rtec Lambda view (Rtec Instruments, Inc., USA).

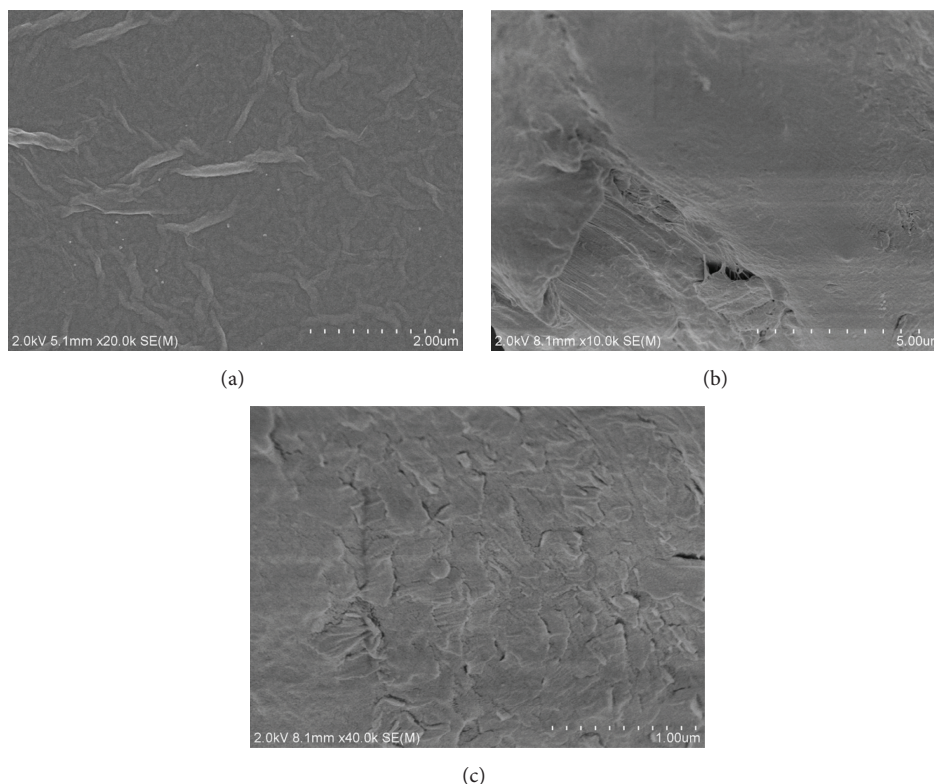


FIGURE 2: The SEM images of (a) GO, (b) UHMWPE, and (c) GO/UHMWPE composites.

3. Results and Discussion

3.1. Surface Topography. The SEM image of GO (Figure 2(a)) displays the rough and wrinkled morphology. The surface topography of UHMWPE and GO/UHMWPE composites is shown in Figures 2(b) and 2(c), respectively. It can be clearly seen from SEM images that incorporation of GO into UHMWPE matrix has a dramatic influence on the surface topography of UHMWPE. In comparison with UHMWPE, GO/UHMWPE composites show uneven surface because crumpled and wrinkled GO sheets are dispersed in the interface of the composites. The wrinkled rough surface of GO can result in a stronger interfacial adhesion between GO and polymer matrix [28]. GO possesses much oxygen-containing polar functionalities, such as hydroxyl, carbonyl, epoxide, and carboxyl groups, which make it more versatile in interacting with various polymers [29]. The stronger interfacial adhesion is beneficial to stress transfer between GO and polymer matrix [30], which can significantly influence the mechanical and tribological properties of UHMWPE.

3.2. Mechanical Properties. The mechanical properties measured are Young's modulus, yield stress, fracture stress, and hardness, which are shown in Figure 3. The results indicate that GO, irradiation, and accelerated aging significantly affect the mechanical properties of test samples.

The nanocomposites with lower GO loading can offer significant improvement in mechanical properties. Young's modulus, yield stress, fracture stress, and hardness

of GO/UHMWPE composites are increased by 22.44%, 8.10%, 42.53%, and 44.32%, respectively, compared to pure UHMWPE. These mechanical behaviors of typical GO/polymer systems have been reported in previous studies [18–20, 23]. The improved mechanical properties of the composites can be attributed to strong interfacial adhesion between GO and UHMWPE matrix, which plays a crucial role in mechanical performance of polymer-GO composites [15]. In GO/UHMWPE composites, van der Waals interaction plays an important role among GO and UHMWPE matrix and consequently GO affects UHMWPE response to tensile loading. Wrinkled GO, tightly adhering on the interface of UHMWPE, can result in interface roughness which may likely lead to an enhanced mechanical interlocking and adhesion with the polymer chains [29]. Moreover, GO contains a range of hydrophilic functionalities on its basal planes and carbon edges, which can enhance compatibility with polymer matrix. Consequently, interfacial forces are transferred efficiently from the polymer matrix to reinforcement [31].

Irradiation further enhances mechanical properties of the composites. Young's modulus, yield stress, fracture stress, and hardness of irradiated composites are increased by 17.22%, 11.66%, 19.50%, and 13.25%, respectively, compared to unirradiated composites. The similar change trends have been observed in irradiated UHMWPE/MWNT nanocomposites [32]. The mechanical properties of the composites depend directly on the crystallinity [33]. During irradiation in vacuum, free radicals are formed due to the cleavage of

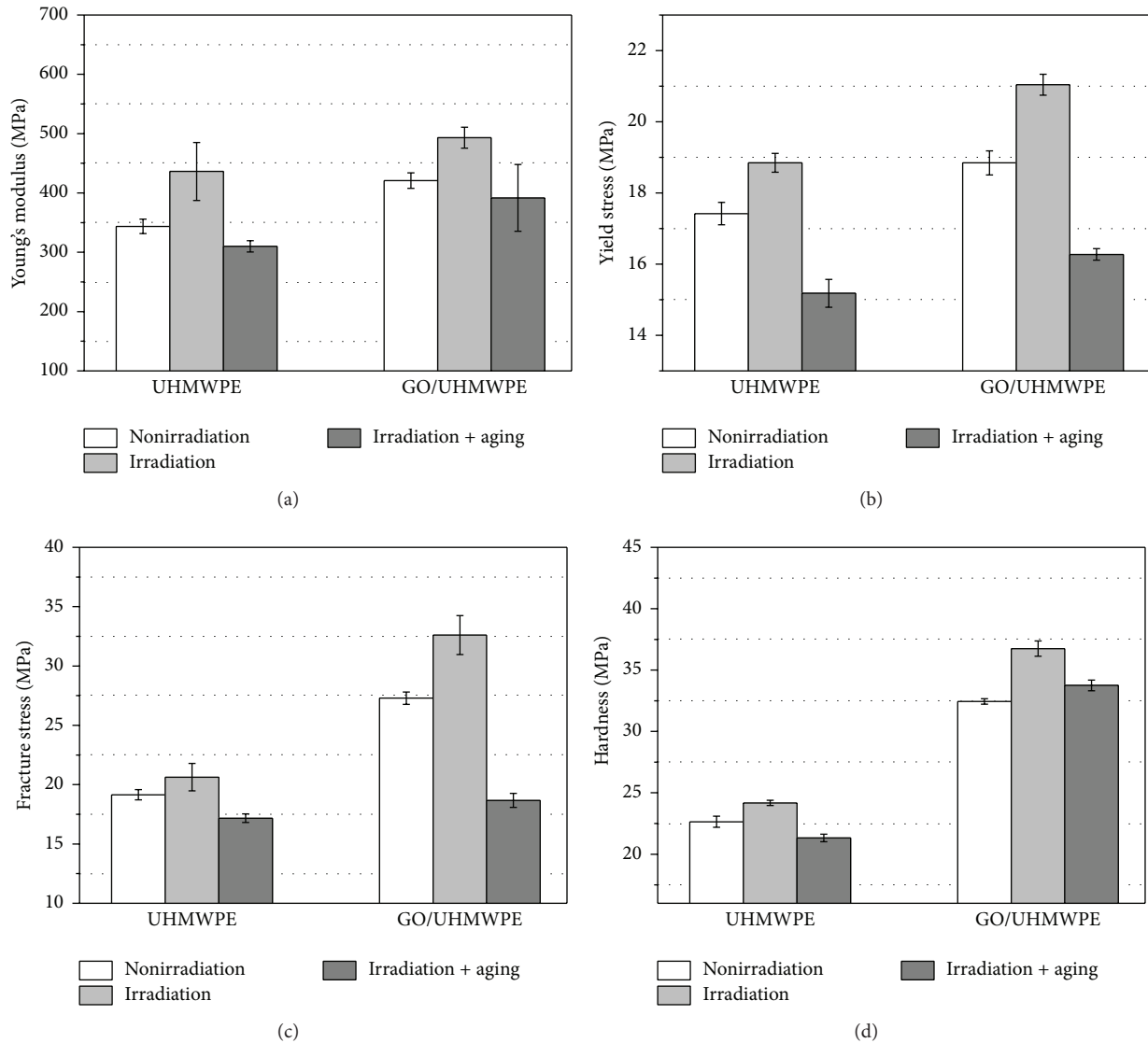


FIGURE 3: Mechanical properties: (a) Young's modulus; (b) yield stress; (c) fracture stress; (d) hardness.

C-C and C-H bond and can recombine with each other to form crosslinking which results in the enhancement of the crystallinity of UHMWPE. According to our previous studies [25], irradiation can significantly increase the crystallinity of GO/UHMWPE composites. Moreover, irradiation can cause bond scission in GO and produce dangling bonds [34] which can create molecular bond with matrix. Recently, it has been reported that GO was very weak radicals scavenger [35]. It may be proposed that few free radicals in UHMWPE may bond with GO. Consequently, irradiation may result in the stronger GO/matrix interaction. Therefore, irradiated composites obtain better mechanical properties than nonirradiated composites. Moreover, GO and irradiation can synergistically enhance the mechanical performance of UHMWPE. These similar results have been reported in irradiated MWCNTs/UHMWPE [32].

However, accelerated aging leads to a significant decrease in mechanical properties of the samples. Young's modulus, yield stress, fracture stress, and hardness of aged composites are reduced by 20.58%, 22.66%, 42.75%, and 8.16%, respectively, compared to irradiated composites. And Young's modulus, yield stress, fracture stress, and hardness of aged UHMWPE are reduced by 28.91%, 19.45%, 20.14%, and 11.78%, respectively, compared to irradiated UHMWPE. After accelerated aging, the reduced mechanical properties are attributed to oxidative degradation of thermal. When the samples undergo accelerated aging, high temperature accelerates oxygen diffusion in the interior of UHMWPE and the migration of free radicals in the crystallinity phase of UHMWPE, which greatly increases the reaction probability of oxygen with free radicals. As a consequence, accelerated oxidative degradation produces a great deal of ketone,

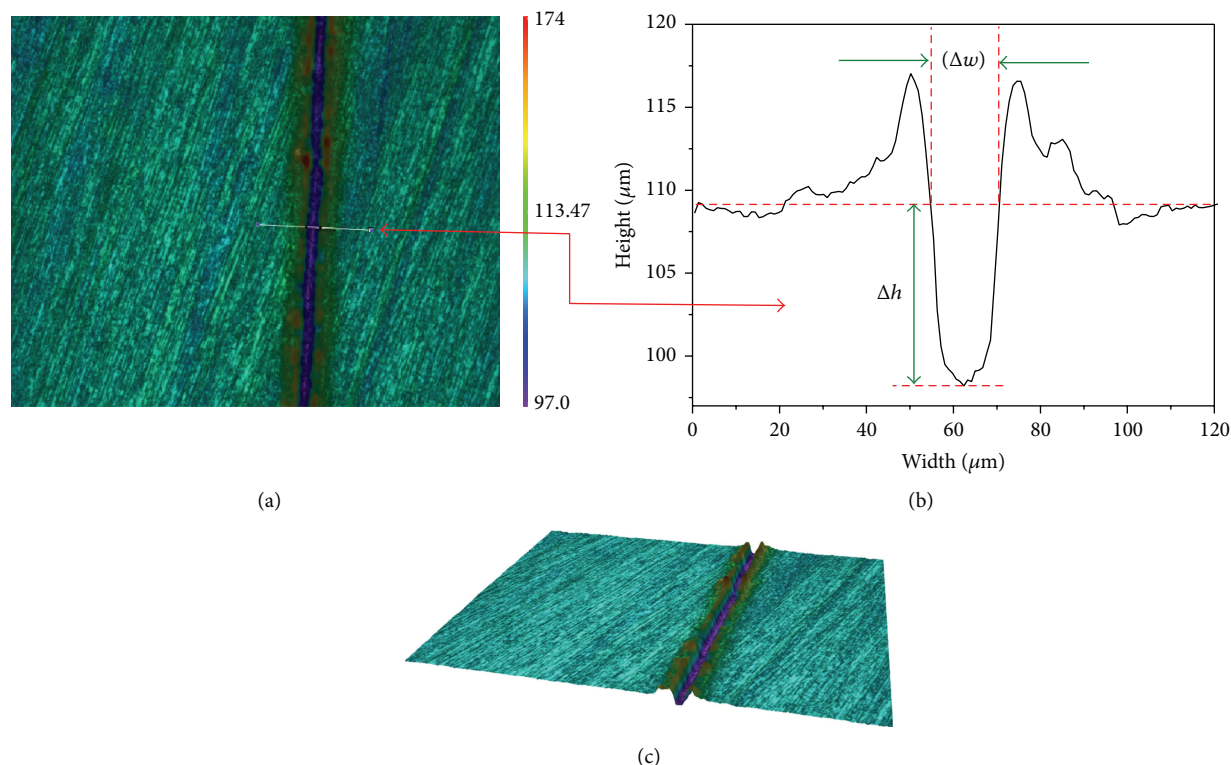


FIGURE 4: (a) 2D image of the scratch. (b) Width and depth profile through the scratch on the test sample. (c) 3D image of the scratch.

alcohol, carboxylic acids, and esters, finally resulting in degradation of mechanical properties of the samples. According to Figure 3, it is also observed that GO cannot restrict the aging degradation of the mechanical properties of UHMWPE. Although GO shows the capacity of scavenging free radicals [35], GO may display a very weak radical scavenging activity in GO/UHMWPE composites, resulting in poor antioxidant capacity [25]. Therefore, the mechanical properties of the composites have been greatly reduced during accelerated aging.

3.3. Tribological Properties. The scratch technique is extensively applied to evaluate the frictional, wear, and scratch resistance characteristics of polymer composites under specified conditions [36]. A diamond tip is pressed on the surface of the samples and then drawn on the surface under a constant force and with a constant velocity. As a typical scratched surface is shown in Figure 4, Δh is mean scratch depth.

In scratching process, the coefficients of friction (COF) are calculated based on (2). Figures 5(a) and 5(b) show the variations of the COF values of different samples. The results indicate that the incorporation of GO shows a slight increase in COF values of GO/UHMWPE nanocomposites, compared to the samples without adding GO. In comparison with unirradiation samples, irradiation further increases the COF of the samples. However, accelerated aging produces a marked decrease in the COF of the samples.

GO is considered as a good candidate for solid lubricants, which can reduce the adhesion and friction force between the

contact surfaces [37]. However, in our experiments, it seems that GO does not display lubricant properties because of a slight increase in the COF, when GO is added into UHMWPE matrix. The similar results have been found by Tai et al. [22]. The reason can be attributed to increased lateral force. The additional lateral force encountered by a diamond tip during travel inside the GO/UHMWPE composites consists of three aspects: GO-UHMWPE bond; GO-GO interlayer van der Waals bonds; and C-C bond in GO plane. Moreover, wrinkled GO sheets can make wrinkled or rough surface and enhance mechanical properties of UHMWPE. As a consequence, the COF of the composites has a slight increase.

After irradiation, the increased COF can be attributed to the crosslinking and chain-reorganization. Free radicals induced by irradiation recombine each other, resulting in chain-reorganization. Crosslinking restricts the mobility of molecular chains in the amorphous region and decreases the creep behavior of UHMWPE. Furthermore, irradiation affects structural integrity and mechanical properties of UHMWPE. Consequently, the plastic property has a reduction and the hardness has been increased, which may result in an increase in the lateral force.

Aging leads to oxidative degradation of polymer composites, which efficiently embrittles the surface and significantly reduces mechanical performance of polymer composites. Aged composites include much shorter chains and have weaker bonding between polymer matrix and the dispersed fillers, compared to unaged polymer composites. Thus, debonding and cracking in the scratch process can be more easily caused in oxidized dominant region of the scratched

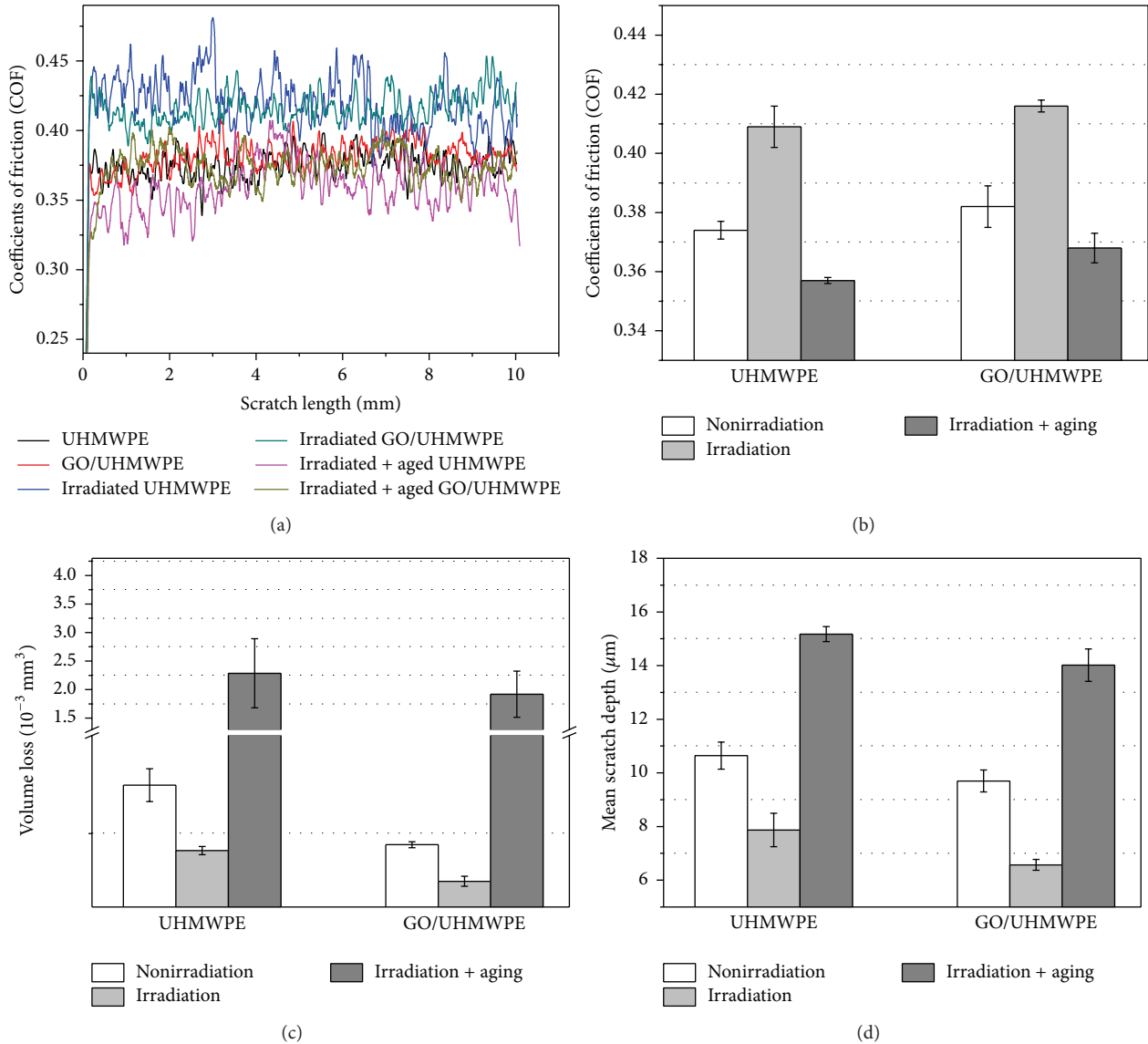


FIGURE 5: ((a), (b)) Coefficients of friction (COF) of test samples. (c) Wear rate of test samples. (d) Mean scratch depth.

subsurface. Consequently, the COF of aged composites has a slight reduction.

The wear volume losses induced by scratch are adopted to evaluate wear resistance properties. The variations of wear volume of all samples are shown in Figure 5(c). The incorporation of GO can improve wear resistance and irradiation further improves wear resistance. However, accelerated aging reduces wear resistance. Comparing wear rate and mechanical properties, it is found that wear rate has a relation with mechanical properties. The wear protection of GO can be attributed to increased mechanical strength and hardness [16]. Irradiation can further increase wear resistance of the composites due to crosslinking. Crosslinking induced by irradiation can increase the wear resistance of UHMWPE by improving the crossing-path motion. Moreover, crosslinking can efficiently restrict chain slippage and make UHMWPE more resistant to being drawn into fibrils [38]. However, after

aging, oxygen degradation can break down the crosslinking and decrease wear resistance while further resulting in reducing mechanical properties.

Figure 5(d) summarizes mean residual depth of the scratch. Adding GO can significantly reduce scratch depth, compared to the samples without adding GO. Irradiation can further decrease residual depth, compared to unirradiated samples. In comparison to GO and irradiation, accelerated aging produces a marked increase of residual depth. Figure 6 shows optical scratching images of test samples. The shallower scratch grooves without fracture are observed from all samples. After accelerated aging, subsurface lateral cracking results in chipping (see Figures 6(e) and 6(f)).

In general, the scratch depth is important microstructure parameters to evaluate scratch resistance [39, 40]. Moreover, the surface deformation is strongly affected by mechanical properties, ductility, and modulus [41]. So, the materials with

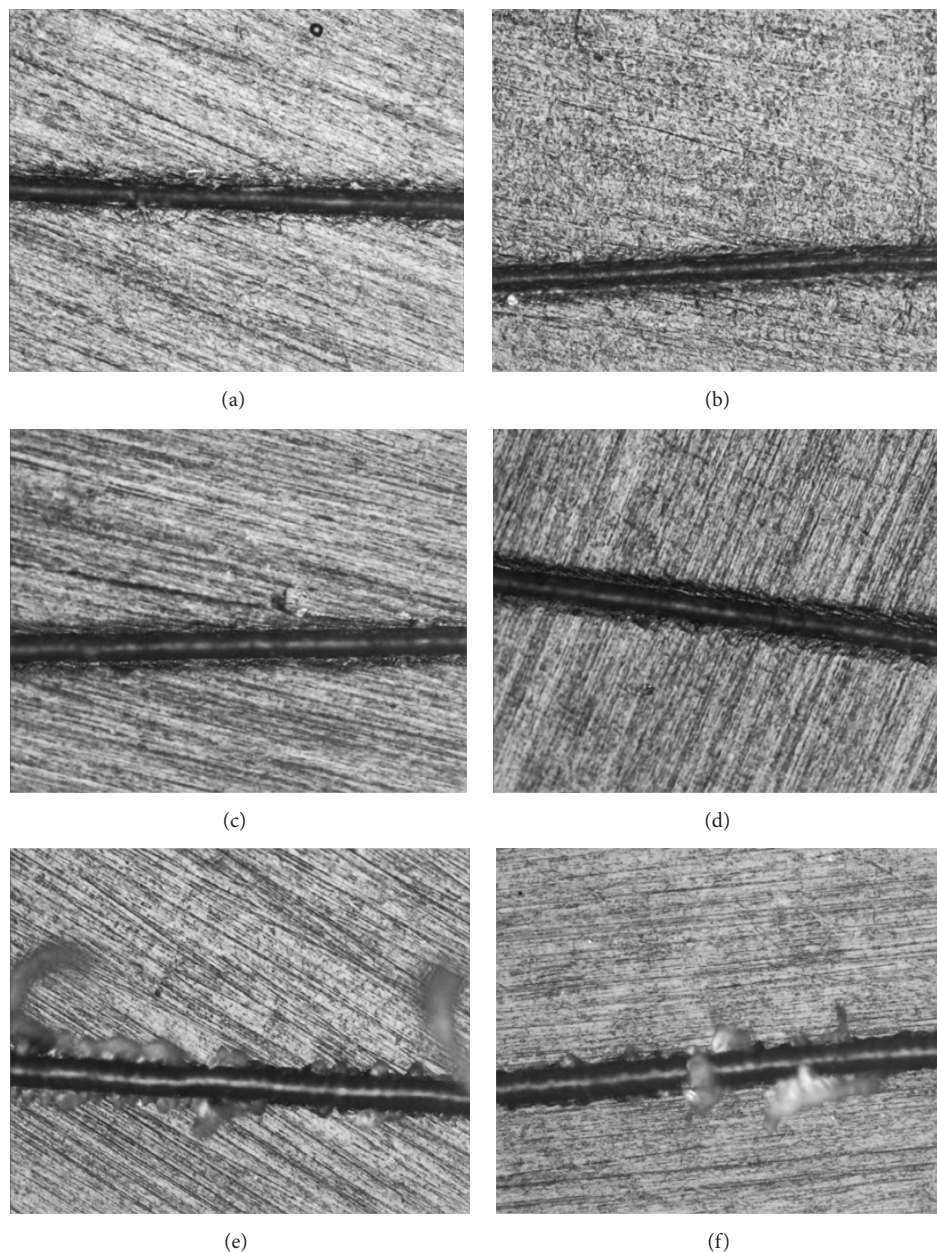


FIGURE 6: Optical scratching images of test samples ($\times 20$): (a) UHMWPE; (b) GO/UHMWPE nanocomposites; (c) irradiated UHMWPE; (d) irradiated GO/UHMWPE nanocomposites; (e) irradiated + aged UHMWPE; (f) irradiated + aged GO/UHMWPE nanocomposites.

excellent mechanical properties may display high scratch resistance. Adding GO can efficiently improve scratch resistance of UHMWPE. The reason is that the incorporation of GO into UHMWPE can increase the crystallinity [20], modulus, and yield stress. Similar results were observed in GO/polypropylene nanocomposites [42]. Irradiation further enhances scratch resistance of the samples because irradiation further increases mechanical properties. In comparison to GO and irradiation, accelerated aging produces a marked increase of residual depth due to oxidative degradation. And, the chip is generated. So accelerated aging leads to a deterioration of scratch resistance properties. Moreover, it is found that the scratch resistance of GO/UHMWPE

composites is synergistically enhanced by combining GO and irradiation.

4. Conclusions

After irradiation and accelerated aging, the mechanical and tribological properties of GO/UHMWPE nanocomposites have been evaluated. The following conclusions can be obtained from above studies.

- (1) The addition of GO to UHMWPE significantly improves the mechanical properties of UHMWPE. Gamma-irradiation further enhances the mechanical properties of GO/UHMWPE nanocomposites.

However, accelerated aging reduces the mechanical properties of GO/UHMWPE nanocomposites.

- (2) Adding GO slightly increases COF values. Irradiation further increases the COF values. But, accelerated aging significantly decreases the COF values.
- (3) GO increases wear resistant properties of UHMWPE and irradiation further enhances the wear resistant properties of the composites. But, accelerated aging significantly reduces wear resistant properties of the samples.
- (4) GO improves antiscratch properties. Irradiation further enhances antiscratch properties. But, accelerated aging reduces antiscratch properties.
- (5) GO and irradiation can synergistically enhance the mechanical, tribological, and antiscratch properties.

Competing Interests

The authors declare that they have no competing interests.

Acknowledgments

The authors are grateful for the financial support from the National Science Foundation of China (Grant nos. 51305166, 51675232), the Natural Science Foundation of Jiangsu Province, China (BK20130143), the Fundamental Research Funds for the Central Universities (JUDCF13028), and Research and Innovation Project for College Graduates of Jiangsu Province in China (CXZZ13_0738).

References

- [1] S. M. Kurtz, *UHMWPE Biomaterials Handbook: Ultra-High Molecular Weight Polyethylene in Total Joint Replacement and Medical Devices*, Academic Press, New York, NY, USA, 2009.
- [2] L. Pruitt, "Conventional and cross-linked polyethylene properties," in *Total Knee Arthroplasty*, pp. 353–360, Springer, Berlin, Germany, 2005.
- [3] Y. Abu-Amer, I. Darwech, and J. C. Clohisy, "Aseptic loosening of total joint replacements: mechanisms underlying osteolysis and potential therapies," *Arthritis Research & Therapy*, vol. 9, supplement 1, article S6, 2007.
- [4] A. V. Lombardi Jr., T. H. Mallory, B. K. Vaughn, and P. Drouillard, "Aseptic loosening in total hip arthroplasty secondary to osteolysis induced by wear debris from titanium-alloy modular femoral heads," *The Journal of Bone & Joint Surgery—American Volume*, vol. 71, no. 9, pp. 1337–1342, 1989.
- [5] Y.-H. Kim, J.-S. Kim, J.-W. Park, and J.-H. Joo, "Periacetabular osteolysis is the problem in contemporary total hip arthroplasty in young patients," *Journal of Arthroplasty*, vol. 27, no. 1, pp. 74–81, 2012.
- [6] A. A. Edidin, L. Pruitt, C. W. Jewett, D. J. Crane, D. Roberts, and S. M. Kurtz, "Plasticity-induced damage layer is a precursor to wear in radiation- cross-linked UHMWPE acetabular components for total hip replacement," *The Journal of Arthroplasty*, vol. 14, no. 5, pp. 616–627, 1999.
- [7] V. Premnath, W. H. Harris, M. Jasty, and E. W. Merrill, "Gamma sterilization of UHMWPE articular implants: an analysis of the oxidation problem," *Biomaterials*, vol. 17, no. 18, pp. 1741–1753, 1996.
- [8] L. Costa, M. P. Luda, L. Trossarelli, E. M. Brach Del Prever, M. Crova, and P. Gallinaro, "Oxidation in orthopaedic UHMWPE sterilized by gamma-radiation and ethylene oxide," *Biomaterials*, vol. 19, no. 7, pp. 659–668, 1998.
- [9] H. Bahrami, S. Ramazani, M. Shafiee, and A. Kheradmand, "Preparation and investigation of tribological properties of ultra-high molecular weight polyethylene (UHMWPE)/graphene oxide," *Polymers for Advanced Technologies*, vol. 27, no. 9, pp. 1172–1178, 2016.
- [10] M. H. Al-Saleh, "Electrical and electromagnetic interference shielding characteristics of GNP/UHMWPE composites," *Journal of Physics D: Applied Physics*, vol. 49, no. 19, Article ID 195302, 2016.
- [11] L. Xu, Y. Zheng, Z. Yan et al., "Preparation, tribological properties and biocompatibility of fluorinated graphene/ultrahigh molecular weight polyethylene composite materials," *Applied Surface Science*, vol. 370, pp. 201–208, 2016.
- [12] Z. Xu, H. Li, and N. Sun, "Rheological investigation of creep recovery for UHMWPE or carbon nanotubes in isotactic polypropylene matrix," *e-Polymers*, vol. 16, no. 2, pp. 145–150, 2016.
- [13] U. Mueller, J. Reinders, and J. Kretzer, "Wear performance of a prototype calcium carbonate containing pmma knee spacer," *The Bone & Joint Journal*, vol. 98, supplement 9, p. 60, 2016.
- [14] J. A. Puértolas and S. M. Kurtz, "Evaluation of carbon nanotubes and graphene as reinforcements for UHMWPE-based composites in arthroplastic applications: a review," *Journal of the Mechanical Behavior of Biomedical Materials*, vol. 39, pp. 129–145, 2014.
- [15] K. Hu, D. D. Kulkarni, I. Choi, and V. V. Tsukruk, "Graphene-polymer nanocomposites for structural and functional applications," *Progress in Polymer Science*, vol. 39, no. 11, pp. 1934–1972, 2014.
- [16] D. Berman, A. Erdemir, and A. V. Sumant, "Graphene: a new emerging lubricant," *Materials Today*, vol. 17, no. 1, pp. 31–42, 2014.
- [17] X. Yang, L. Li, S. Shang, and X.-M. Tao, "Synthesis and characterization of layer-aligned poly(vinyl alcohol)/graphene nanocomposites," *Polymer*, vol. 51, no. 15, pp. 3431–3435, 2010.
- [18] W. Pang, Z. Ni, G. Chen, G. Huang, H. Huang, and Y. Zhao, "Mechanical and thermal properties of graphene oxide/ultrahigh molecular weight polyethylene nanocomposites," *RSC Advances*, vol. 5, no. 77, pp. 63063–63072, 2015.
- [19] H. Bahrami, A. S. A. Ramazani, A. Kheradmand, M. Shafiee, and H. Baniasadi, "Investigation of thermomechanical properties of UHMWPE/graphene oxide nanocomposites prepared by in situ ziegler-natta polymerization," *Advances in Polymer Technology*, vol. 34, no. 4, Article ID 21508, 2015.
- [20] Y. Chen, Y. Qi, Z. Tai, X. Yan, F. Zhu, and Q. Xue, "Preparation, mechanical properties and biocompatibility of graphene oxide/ultrahigh molecular weight polyethylene composites," *European Polymer Journal*, vol. 48, no. 6, pp. 1026–1033, 2012.
- [21] Y. F. An, Z. X. Tai, Y. Y. Qi et al., "Friction and wear properties of graphene oxide/ultrahigh-molecular-weight polyethylene composites under the lubrication of deionized water and normal saline solution," *Journal of Applied Polymer Science*, vol. 131, no. 1, Article ID 39640, 2014.
- [22] Z. X. Tai, Y. F. Chen, Y. F. An, X. B. Yan, and Q. J. Xue, "Tribological behavior of UHMWPE reinforced with graphene

- oxide nanosheets," *Tribology Letters*, vol. 46, no. 1, pp. 55–63, 2012.
- [23] S. Suñer, R. Joffe, J. L. Tipper, and N. Emami, "Ultra high molecular weight polyethylene/graphene oxide nanocomposites: thermal, mechanical and wettability characterisation," *Composites Part B: Engineering*, vol. 78, pp. 185–191, 2015.
- [24] W. S. Hummers Jr. and R. E. Offeman, "Preparation of graphitic oxide," *Journal of the American Chemical Society*, vol. 80, no. 6, p. 1339, 1958.
- [25] G. Huang, Z. Ni, G. Chen, W. Pang, and Y. Zhao, "Effects of gamma irradiation and accelerated aging on GO/UHMWPE nanocomposites," *International Journal of Polymer Analysis and Characterization*, vol. 21, no. 5, pp. 417–427, 2016.
- [26] ISO, "Plastics and ebonite—determination of hardness by the ball indentation method," ISO 2039-73, International Organization for Standardization, 1973.
- [27] S. Cao, H. Liu, S. Ge, and G. Wu, "Mechanical and tribological behaviors of UHMWPE composites filled with basalt fibers," *Journal of Reinforced Plastics and Composites*, vol. 30, no. 4, pp. 347–355, 2011.
- [28] R. Verdejo, M. M. Bernal, L. J. Romasanta, and M. A. Lopez-Manchado, "Graphene filled polymer nanocomposites," *Journal of Materials Chemistry*, vol. 21, no. 10, pp. 3301–3310, 2011.
- [29] T. Ramanathan, A. A. Abdala, S. Stankovich et al., "Functionalized graphene sheets for polymer nanocomposites," *Nature Nanotechnology*, vol. 3, no. 6, pp. 327–331, 2008.
- [30] Z. Li, R. J. Young, and I. A. Kinloch, "Interfacial stress transfer in graphene oxide nanocomposites," *ACS Applied Materials and Interfaces*, vol. 5, no. 2, pp. 456–463, 2013.
- [31] L. Gong, I. A. Kinloch, R. J. Young, I. Riaz, R. Jalil, and K. S. Novoselov, "Interfacial stress transfer in a graphene monolayer nanocomposite," *Advanced Materials*, vol. 22, no. 24, pp. 2694–2697, 2010.
- [32] M. J. Martínez-Morlanes, P. Castell, V. Martínez-Nogués, M. T. Martínez, P. J. Alonso, and J. A. Puértolas, "Effects of gamma-irradiation on UHMWPE/MWNT nanocomposites," *Composites Science and Technology*, vol. 71, no. 3, pp. 282–288, 2011.
- [33] N. Shibata, S. M. Kurtz, and N. Tomita, "Recent advances of mechanical performance and oxidation stability in ultrahigh molecular weight polyethylene for total joint replacement: highly crosslinked and α -tocopherol doped," *Journal of Biomechanical Science and Engineering*, vol. 1, no. 1, pp. 107–123, 2006.
- [34] L. F. Dumée, C. Feng, L. He et al., "Single step preparation of meso-porous and reduced graphene oxide by gamma-ray irradiation in gaseous phase," *Carbon*, vol. 70, pp. 313–318, 2014.
- [35] Y. Qiu, Z. Wang, A. C. E. Owens et al., "Antioxidant chemistry of graphene-based materials and its role in oxidation protection technology," *Nanoscale*, vol. 6, no. 20, pp. 11744–11755, 2014.
- [36] B. J. Briscoe, P. D. Evans, E. Pelillo, and S. K. Sinha, "Scratching maps for polymers," *Wear*, vol. 200, no. 1–2, pp. 137–147, 1996.
- [37] K.-S. Kim, H.-J. Lee, C. Lee et al., "Chemical vapor deposition-grown graphene: the thinnest solid lubricant," *ACS Nano*, vol. 5, no. 6, pp. 5107–5114, 2011.
- [38] J. De Boer, H.-J. Van Den Berg, and A. J. Pennings, "Crosslinking of ultra-high molecular weight polyethylene in the oriented state with dicumylperoxide," *Polymer*, vol. 25, no. 4, pp. 513–519, 1984.
- [39] A. Dasari, Z.-Z. Yu, and Y.-W. Mai, "Fundamental aspects and recent progress on wear/scratch damage in polymer nanocomposites," *Materials Science and Engineering R: Reports*, vol. 63, no. 2, pp. 31–80, 2009.
- [40] M. Wong, G. T. Lim, A. Moyses, J. N. Reddy, and H.-J. Sue, "A new test methodology for evaluating scratch resistance of polymers," *Wear*, vol. 256, no. 11–12, pp. 1214–1227, 2004.
- [41] R. D. K. Misra, R. Hadal, and S. J. Duncan, "Surface damage behavior during scratch deformation of mineral reinforced polymer composites," *Acta Materialia*, vol. 52, no. 14, pp. 4363–4376, 2004.
- [42] K.-Y. Shin, J.-Y. Hong, S. Lee, and J. Jang, "Evaluation of anti-scratch properties of graphene oxide/polypropylene nanocomposites," *Journal of Materials Chemistry*, vol. 22, no. 16, pp. 7871–7879, 2012.

Research Article

Bottom-Up Fabrication of PEG Brush on Poly(dimethylsiloxane) for Antifouling Surface Construction

Junmei Tang, Yuemei Han, Hao Chen, and Quankui Lin

School of Ophthalmology & Optometry, Eye Hospital, Wenzhou Medical University, Wenzhou 325027, China

Correspondence should be addressed to Quankui Lin; lqk97531@126.com

Received 5 May 2016; Accepted 26 May 2016

Academic Editor: Weifeng Zhao

Copyright © 2016 Junmei Tang et al. This is an open access article distributed under the Creative Commons Attribution License, which permits unrestricted use, distribution, and reproduction in any medium, provided the original work is properly cited.

Poly(dimethylsiloxane) silicones have found many applications in biomedical devices, whereas their surface hydrophobicity always brings about unexpected bioadhesion, causing complications of the implanted biomedical devices. In this work, surface-initiated reversible addition-fragmentation chain transfer (SI-RAFT) polymerization was utilized to generate PEG brushes on silicone surface, obtaining highly hydrophilic surface coatings. Such PEG brush coated silicone presents excellent antifouling to protein, cells, and bacteria, which may have great potential in implantable biomaterial surface modifications.

1. Introduction

Poly(dimethylsiloxane) (PDMS) silicones have found many applications in biomedical devices, such as catheters, prostheses, contact lens, and intraocular lens [1]. But their hydrophobicity always brings about unexpected bioadhesion on the surface, which may cause the main complications of the implanted biomedical devices. For example, the adhesion and proliferation of the lens epithelial cells on the silicone intraocular lens may cause the after cataract, a common complication after the cataract surgery, which leads to losing vision again [2]. It is also common that the rapid accumulation of tear proteins or the adhesion of bacteria may potentially cause the adverse clinical events in contact lens wearing [3]. These complications are related to the biofouling of the silicone materials.

Generally, biofouling is generated by the attachment of microorganisms such as cells or bacteria to the surface. To circumvent such problems, a variety of strategies have been developed to modify the surface properties of PDMS by physical modification or chemical covalent methods, including oxygen plasma, ultraviolet light/ozone, polyelectrolyte multilayers, surface activation, and chemical grafting [4–8]. Particularly, polyethylene glycol (PEG) surface modification is an effective method for antifouling purpose [7, 9]. The PEG with active ending groups can be coupled to the surface via chemical grafting. However, the

PEGylated surface fabricated from “graft-to” method only renders short term effects on antifouling, which may be due to the sparseness and irregular arrangement of the PEG chains [10, 11]. The favorable antifouling surface calls for the well-defined PEG coating techniques.

Surface-initiated living radical polymerization reactions provide a good alternative for the biomedical materials surface modification, as obtaining the well-defined polymer brushes. Reversible addition-fragmentation chain transfer (RAFT) polymerization is one of the living radical polymerization techniques and it has enjoyed widespread acceptance as a modification technique due to its capability to control polymerization of diverse monomers under mild reaction conditions without the requirement of metal catalysts [12–14]. Antifouling surface can be obtained via surface-initiated RAFT polymerization of antifouling molecules on the material surface [15–17]. In this work, surface-initiated RAFT (SI-RAFT) was carried out for bottom-up grafting PEG brushes on silicone surface for antifouling applications. The hydrophilicity of the coatings was investigated and the antifouling properties were tested by protein adsorption, *S. aureus* adhesion, and lens epithelial cell adhesion assays.

2. Materials and Methods

2.1. Materials. PDMS precursors Sylgard 184 were purchased from Dow Corning Corporation, USA.

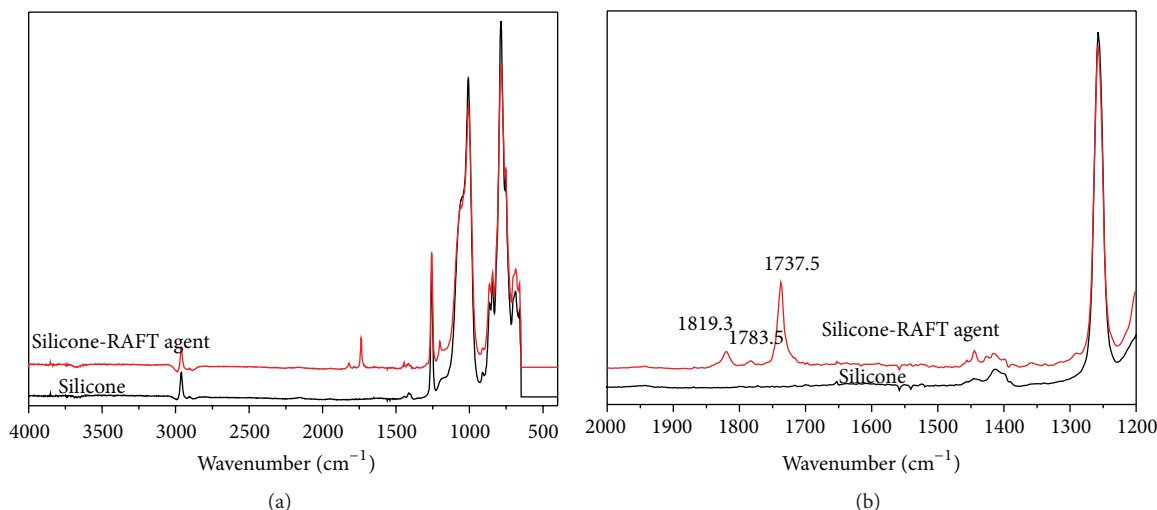


FIGURE 1: (a) The ATR-FTIR spectra of the silicone before and after RAFT agent immobilization. (b) The amplification of the ATR-FTIR spectra in the wavenumber range of 1200 to 2000 cm^{-1} .

(3-Aminopropyl)triethoxysilane (APTES), 4-cyano-4-(phenylcarbonothioylthio)pentanoic acid (CPCTTPA), N-(3-dimethylaminopropyl)-N'-ethylcarbodiimide hydrochloride (EDC), N-hydroxysulfosuccinimide sodium (NHS), polyethylene glycol methacrylate (PEGMA, $M_n = 360$), and 4-cyano-4-(2-cyano-5-hydroxy-5-oxopentan-2-yl) diazenylpentanoic acid (V501) were purchased from Sigma, USA.

2.2. Experimental Methods. Silicone was made from PDMS at a weight ratio of A : B = 1 : 10, according to the supplier. The surface modification is initiated by the RAFT agent immobilization onto the silicone. Briefly, silicone was immersed in APTES/ethanol (1%, w/v) solution overnight. The aminolyzed silicone was then immersed into a reaction vessel containing 4-cyano-4-(phenylcarbonothioylthio)pentanoic acid (CPCTTPA, 0.22 mg/mL), N-(3-dimethylaminopropyl)-N'-ethylcarbodiimide hydrochloride (EDC, 40 mg/mL), and N-hydroxysulfosuccinimide sodium (NHS, 20 mg/mL) in distilled water. The reaction mixture was left on a shaking device for 48 h at room temperature. The CPCTTPA immobilized silicone was used for SI-RAFT polymerization. Typically, polyethylene glycol methacrylate (PEGMA, $M_n = 360$) and 0.5 mg/mL 4-cyano-4-(2-cyano-5-hydroxy-5-oxopentan-2-yl) diazenylpentanoic acid (V501) were dissolved with ethanol in microwave-safe glass vials and degassed. The vials were placed in Initiator Microwave System (Initiator-60, Biotage, Sweden) to perform polymerization at 60°C for predetermined time. After reaction, the functionalized silicone was removed from the solution, washed with ethanol and distilled water ultrasonically, and dried under vacuum overnight. Fourier transform infrared (FTIR) spectroscopy in attenuated total reflection (ATR) mode was used to characterize the immobilization of the RAFT agent and contact angle observation was utilized to evaluate the hydrophilicity of PEG brush modified silicone surface. The protein adsorption, *S. aureus* adhesion, and lens epithelial cell adhesion assays were then carried out on the

functionalized silicone substrate according to the procedures in our previous publications [5, 6, 18, 19].

3. Results and Discussion

Figure 1 shows the ATR-FTIR curves of the silicone substrate before or after RAFT agent immobilization. As it can be seen in both of the spectra, there is a strongest band at the wavenumbers from 1000 to 1120 cm^{-1} , which are attributed to the stretching vibration peaks of Si-O-Si. The asymmetric and symmetric stretching vibrations of C-H₃ occur at 2962 and 2909 cm^{-1} , respectively. A sharp single peak is seen in every spectrum at 1250 cm^{-1} , attributed to the deformation vibration of C-H₃ in Si-Me₂ group [20]. Compared to the general symmetric deformation vibration of C-H₃ in alkyl group, this vibration band takes a distinct red shift from 1375 to 1250 cm^{-1} . There is a tiny peak on the silicone spectra at 2160 cm^{-1} and it disappears after the RAFT agent immobilization. The characteristic vibration of 2160 cm^{-1} is conventionally attributed to the stretching vibration of Si-H bond. The Si-H should disappear after the surface reacted with the silane coupling agent as the Si-H was substituted by the Si-O-Si after reaction. There are also some new characteristic peaks which appear after the RAFT agent immobilization. As shown in Figure 1(b), the peak at 1737.5 cm^{-1} is due to the characteristic absorption bands of the carbonyl group, originated from the carboxyl group in the RAFT agent. Peak at 1443.2 cm^{-1} is also originated from the vibration of S-C in the RAFT agent. These results indicate the successful immobilization of the RAFT agent on the silicone surface.

Figure 2 shows the results of surface contact angle (SCA) measurements of the silicone before and after SI-RAFT polymerization of PEGMA. The silicone is a material with high hydrophobic surface properties. The initial value of SCA is measured after the water drop contacting with the surface for 30 s. The initial SCA of silicone is 112.8° (Figure 2(a)(a1)).

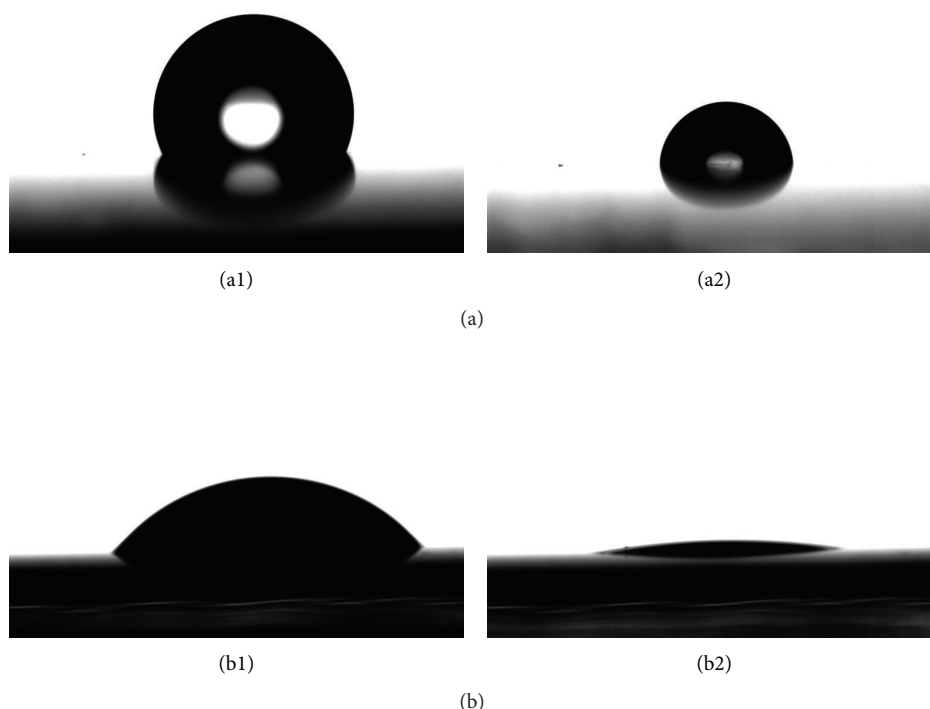


FIGURE 2: Representative surface contact angle images of silicone with (b) or without (a) PEG brush modification. The images were obtained after water drops contacting with the surface for 30 s (a1, b1) and 11 min (a2, b2).

After surface modification of PEG brushes via SI-RAFT, the SCA decreases to 50.6° (Figure 2(b)(b1)). The surface hydrophilicity is greatly improved after the PEG brushes surface modification. More interestingly, the SCA of the PEG brushes modified surface decreases to less than 8.0° after the water drop contacting with the surface for 11 min (Figure 2(b)(b2)), whereas the SCA of pristine silicone is 84.2° (Figure 2(a)(a2)). The silicone is a hydrophobic material; the small decline of the SCA on silicone surface with time increase may be due to the water evaporation. However, the dramatic decrease of the SCA on the PEG brushes modified surface is not just due to the evaporation. The SI-RAFT polymerization on the surface can obtain a brush structured polymer on the surface [15, 16]. The brush structure plays an important role in high hydrophilicity of the PEG modified surface. Surface with excellent hydrophilicity is obtained after the SI-RAFT polymerization of PEG on the surface as PEG brushes are generated via bottom-up living polymerization.

Figure 3 shows the protein adsorption results on the silicone before and after PEG brushes modification. The albumin is used as a modal protein for test. The pristine silicone easily absorbs proteins due to its hydrophobic nature. However, the hydrophilic PEG brushes modification greatly reduces the protein adsorption on the surface. The absorbed protein on the modified surface is about 40% of that on the pristine surface. Figure 4 shows the cell and bacteria adhesion results on the surface. The lens epithelial cell (LEC) and *S. aureus* are used. As we can see, the pristine silicone is bioadhesive for both LEC and *S. aureus*. Plenty of LEC and *S. aureus* are

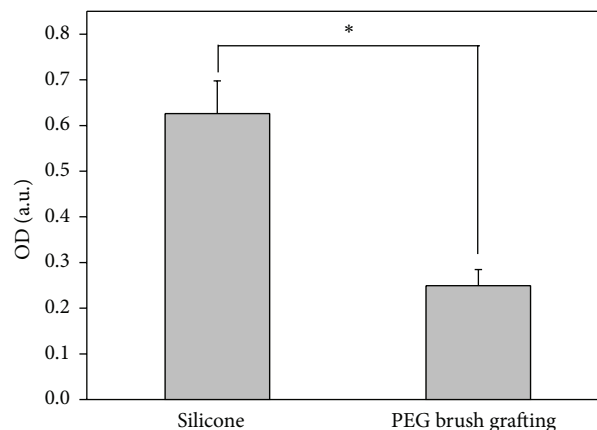


FIGURE 3: The protein adsorption of silicone before and after PEG brush grafting. *Significant difference.

found on the silicone surface (Figures 4(a) and 4(c)). The adhered cells present spreading morphology on the surface, indicating the high cell viability on such surface. The PEG brushes modification greatly reduced the cell and bacteria adhesion. Seldom cells are found on the modified surface. The few adhered cells render small round morphology, which indicates the lack of cell viability on such surface. The cell and bacterial adhesion on the implantable materials may cause lots of complications. For example, the LEC adhesion onto the material surface is the main reason for the silicone intraocular

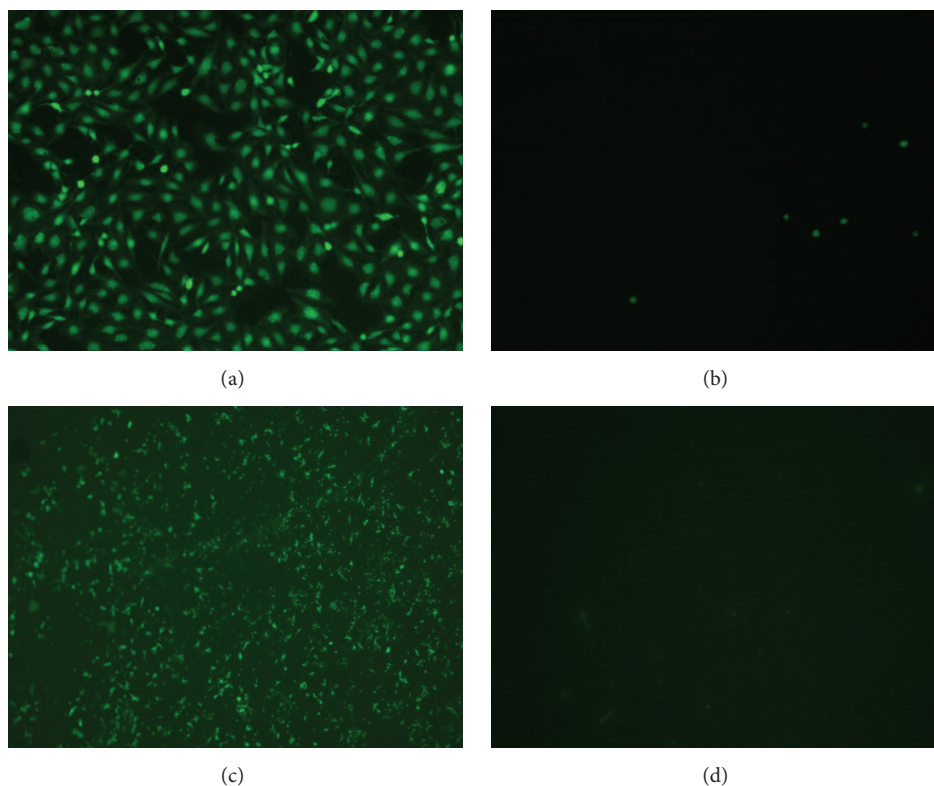


FIGURE 4: The lens epithelial cell (a, b) and *S. aureus* (c, d) adhesion on silicone before and after PEG brush grafting.

lens implantation. *S. aureus* adhesion and invasion may cause endophthalmitis, which is a critical issue of the vision loss in ophthalmologic surgery. The above result indicates that an excellent antifouling surface is obtained via SI-RAFT polymerization of PEGMA on silicone surface, which greatly improves the biocompatibility for biomaterial applications.

4. Conclusions

In this paper, a PEG brush coating is obtained via surface-initiated RAFT polymerization of polyethylene glycol methacrylate on silicone surface. The surface contact angle analysis shows the excellent hydrophilicity of the PEG brush coating surface. The in vitro protein adsorption assay indicates that the PEG brush coating can notably decrease the protein adsorption on the surface. The lens epithelial cell and *S. aureus* adhesion assay results indicate that such PEG brush modification can evidently resist the cell and bacteria adhesion. Such antifouling silicone with excellent hydrophilic PEG brush coatings might have great potential in the implantable biomaterials.

Competing Interests

The authors declare that there are no competing interests regarding the publication of this paper.

Authors' Contributions

Junmei Tang and Yuemei Han contributed equally to this paper.

Acknowledgments

The authors greatly acknowledge the financial support from National Natural Science Foundation of China (31570959 and 51203120), Natural Science Foundation of Zhejiang Province (LY16H120003 and LQ12E03001), Medical & Health Technology Program of Zhejiang Province (2014KYA149), Public Welfare Science & Technology Program of Wenzhou (Y20150083 and Y20120201), and Xinmiao Talents Program of Zhejiang Province (2015R413074).

References

- [1] M. Li, K. G. Neoh, L. Q. Xu et al., "Surface modification of silicone for biomedical applications requiring long-term antibacterial, antifouling, and hemocompatible properties," *Langmuir*, vol. 28, no. 47, pp. 16408–16422, 2012.
- [2] L. Werner, "Biocompatibility of intraocular lens materials," *Current Opinion in Ophthalmology*, vol. 19, no. 1, pp. 41–49, 2008.
- [3] H. Thissen, T. Gengenbach, R. du Toit et al., "Clinical observations of biofouling on PEO coated silicone hydrogel contact lenses," *Biomaterials*, vol. 31, no. 21, pp. 5510–5519, 2010.

- [4] W. Mussard, N. Kebir, I. Kriegel, M. Estève, and V. Semetey, "Facile and efficient control of Bioadhesion on poly(dimethylsiloxane) by using a biomimetic approach," *Angewandte Chemie—International Edition*, vol. 50, no. 46, pp. 10871–10874, 2011.
- [5] Q. Lin, X. Xu, B. Wang et al., "Hydrated polysaccharide multilayer as an intraocular lens surface coating for biocompatibility improvements," *Journal of Materials Chemistry B*, vol. 3, no. 18, pp. 3695–3703, 2015.
- [6] B. L. Wang, Q. K. Lin, T. W. Jin et al., "Surface modification of intraocular lenses with hyaluronic acid and lysozyme for the prevention of endophthalmitis and posterior capsule opacification," *RSC Advances*, vol. 5, no. 5, pp. 3597–3604, 2015.
- [7] H. Chen, Y. Chen, H. Sheardown, and M. A. Brook, "Immobilization of heparin on a silicone surface through a heterobifunctional PEG spacer," *Biomaterials*, vol. 26, no. 35, pp. 7418–7424, 2005.
- [8] C. Wetzl, J. Schönfelder, W. Schwarz, and R. H. W. Funk, "Surface modification of polyurethane and silicone for therapeutic medical technics by means of electron beam," *Surface & Coatings Technology*, vol. 205, no. 5, pp. 1618–1623, 2010.
- [9] K. Chawla, S. Lee, B. P. Lee, J. L. Dalsin, P. B. Messersmith, and N. D. Spencer, "A novel low-friction surface for biomedical applications: modification of poly(dimethylsiloxane) (PDMS) with polyethylene glycol(PEG)-DOPA-lysine," *Journal of Biomedical Materials Research Part A*, vol. 90, no. 3, pp. 742–749, 2009.
- [10] Á. Serrano, O. Sterner, S. Mieszkin et al., "Nonfouling response of hydrophilic uncharged polymers," *Advanced Functional Materials*, vol. 23, no. 46, pp. 5706–5718, 2013.
- [11] X. Xu, J.-M. Tang, Y.-M. Han, W. Wang, H. Chen, and Q.-K. Lin, "Surface PEGylation of intraocular lens for PCO prevention: an *in vivo* evaluation," *Journal of Biomaterials Applications*, 2016.
- [12] Y. Shi, M. Liu, K. Wang et al., "Direct surface PEGylation of nanodiamond via RAFT polymerization," *Applied Surface Science*, vol. 357, pp. 2147–2153, 2015.
- [13] K. Ohno, Y. Ma, Y. Huang et al., "Surface-initiated reversible addition-fragmentation chain transfer (RAFT) polymerization from fine particles functionalized with trithiocarbonates," *Macromolecules*, vol. 44, no. 22, pp. 8944–8953, 2011.
- [14] M. C. R. Tria, C. D. T. Grande, R. R. Ponnepati, and R. C. Advincula, "Electrochemical deposition and surface-initiated RAFT polymerization: protein and cell-resistant PPEGMEMA polymer brushes," *Biomacromolecules*, vol. 11, no. 12, pp. 3422–3431, 2010.
- [15] F. Audouin and A. Heise, "Surface-initiated RAFT polymerization of NIPAM from monolithic macroporous polyHIPE," *European Polymer Journal*, vol. 49, no. 5, pp. 1073–1079, 2013.
- [16] J. Yuan, X. Huang, P. Li, L. Li, and J. Shen, "Surface-initiated RAFT polymerization of sulfobetaine from cellulose membranes to improve hemocompatibility and antibiofouling property," *Polymer Chemistry*, vol. 4, no. 19, pp. 5074–5085, 2013.
- [17] B. L. Wang, T. W. Jin, Y. M. Han et al., "Surface-initiated RAFT polymerization of p (MA POSS-co-DMAEMA⁺) brushes on PDMS for improving antiadhesive and antibacterial properties," *International Journal of Polymeric Materials and Polymeric Biomaterials*, vol. 65, no. 2, pp. 55–64, 2016.
- [18] Q. K. Lin, X. Ding, F. Y. Qiu, X. Song, G. Fu, and J. Ji, "In situ endothelialization of intravascular stents coated with an anti-CD34 antibody functionalized heparin-collagen multilayer," *Biomaterials*, vol. 31, no. 14, pp. 4017–4025, 2010.
- [19] Q. K. Lin, X. Xu, Y. Q. Wang et al., "Antiadhesive and antibacterial polysaccharide multilayer as IOL coating for prevention of postoperative infectious endophthalmitis," *International Journal of Polymeric Materials and Polymeric Biomaterials*, 2016.
- [20] D.-J. Guo, H.-M. Han, Jing-Wang, S.-J. Xiao, and Z.-D. Dai, "Surface-hydrophilic and protein-resistant silicone elastomers prepared by hydrosilylation of vinyl poly(ethylene glycol) on hydrosilanes-poly(dimethylsiloxane) surfaces," *Colloids and Surfaces A: Physicochemical and Engineering Aspects*, vol. 308, no. 1–3, pp. 129–135, 2007.

Research Article

Influence of Sodium Alginate on Hypoglycemic Activity of Metformin Hydrochloride in the Microspheres Obtained by the Spray Drying

Marta Szekalska, Magdalena Wróblewska, Katarzyna Sosnowska, and Katarzyna Winnicka

Department of Pharmaceutical Technology, Medical University of Białystok, Mickiewicza 2c, 15-222 Białystok, Poland

Correspondence should be addressed to Katarzyna Winnicka; kwin@umb.edu.pl

Received 23 March 2016; Accepted 27 April 2016

Academic Editor: Qiang Wei

Copyright © 2016 Marta Szekalska et al. This is an open access article distributed under the Creative Commons Attribution License, which permits unrestricted use, distribution, and reproduction in any medium, provided the original work is properly cited.

Alginate microspheres with metformin hydrochloride were prepared by the spray drying method in order to improve residence time of drug in the stomach. Nine formulations (F1–F9) with various drug : polymer ratio (1 : 2, 1 : 1, and 2 : 1) and different sodium alginate concentration (1%, 2%, and 3%) were evaluated for size, morphology, drug loading, Zeta potential, and swelling degree. *In vitro* drug release, mathematical release profile, and physical state of microspheres were also evaluated. Optimal formulation characterized by the highest drug loading was formulation F6 (drug : polymer ratio 2 : 1 and 2% alginate solution). Based on glucose uptake in *Saccharomyces cerevisiae* cells and α -amylase inhibition tests, it could be concluded that alginate microspheres enhance hypoglycemic activity of metformin hydrochloride evaluated *in vitro*. Designed microspheres are promising as alternative, multicompartiment dosage form for metformin hydrochloride delivery.

1. Introduction

Sodium alginate (ALG) is nontoxic, biocompatible, and biodegradable polymer, which belongs to the group of polysaccharides naturally present in the seaweed [1, 2]. ALG is composed of monomers of β -D-mannuronic acid and α -L-guluronic acid residues joined together by (1–4) glycoside linkages. It is a biopolymer widely used for dietetic, biotechnology, cosmetic, and pharmaceutical industry [3]. Mucoadhesiveness and ability to gelate make ALG a promising excipient in the development of various dosage forms for modified drug delivery. In contact with acidic pH, ALG cross-links and forms swollen polymer matrix which acts as a reservoir enabling sustained drug release [4, 5]. Additionally, ALG is characterized by the ability to reduce body weight and to control glycemia in diabetic individuals by reduction after meal fluctuations of glucose concentrations, insulin secretion, decreasing of food intake, and delaying gastric emptying [6–8].

Metformin hydrochloride (MF) is an orally administered antidiabetic agent from biguanide group, which is the first line therapy to treat type 2 diabetes. Its hypoglycemic action includes decrease in the hepatic glucose production and in

the intestinal glucose absorption and increase in glucose metabolism which, in consequence, lead to the reduction in plasma glucose concentration. In addition, MF decreases appetite and has effect on weight reduction and improvement of the lipid profile with no risk of hypoglycemia. MF is water soluble, but its bioavailability after oral administration in conventional dosage forms is only about 50% [9, 10]. Increase in the stomach residence time and the improvement in drug bioavailability might be achieved by mucoadhesive dosage forms. Mucoadhesive drug delivery systems through the intimate contact with the absorption surface enable prolonged residence time, better drug absorption, and enhanced bioavailability and they also permit decrease in the drug dosing frequency. Microspheres are multicompartiment dosage forms which provide improved efficacy, reduced toxicity, and larger margin of safety in case of dosage form damage compared with traditional single unit formulations. Mucoadhesive polymer's matrix enables them to adhere to the mucous membranes and to remain for longer time period in the gastrointestinal tract [11, 12].

One of the most widely reported methods for preparing ALG microspheres with MF is emulsion-cross-linking and nonaqueous evaporation [13–16]; therefore, the aim of this

research was to attempt to formulate for the first time ALG microspheres with MF by the new spray drying technique. Obtained microspheres were characterized for size, morphology, entrapment efficiency, drug loading, Zeta potential, and the *in vitro* MF release. The effects of the drug:polymer ratio and concentration of ALG solution on the properties of microspheres were also studied. Mucoadhesive properties of the microspheres were examined by using TA.XT.Plus Texture Analyzer and three different models of adhesive layer: gelatin disc, mucin gel, and porcine stomach mucosa. The physical state of microspheres was determined by differential scanning calorimetry (DSC). Additionally, the hypoglycemic properties of microspheres and the influence of ALG on MF activity were studied by determination of glucose uptake in *Saccharomyces cerevisiae* cells and by α -amylase inhibition test.

2. Experimental Section

2.1. Materials. Metformin hydrochloride (MF) was obtained from Debao Fine Chemical CO (Henan, China). Sodium alginate (ALG) low viscosity (2%, 100–300 cP), mucin type II, and gelatin type B from bovine skin were purchased from Sigma Aldrich (Steinheim, Germany). Potassium dihydrogen phosphate, sodium hydroxide, hydrochloric acid, methanol, propan-1,2-diol, acetonitrile, and starch pure soluble were obtained from Chempur (Piekary Śląskie, Poland). Glucose was obtained from Prolab (Nakło, Poland). Water was distilled and passed through a reverse osmosis system, Milli-Q Reagent Water System (Billerica, USA). Porcine stomach mucosa from large white pigs weighting ≈ 200 kg was obtained from the veterinary service (Turośń Kościelna, Poland). Samples were stored at -20°C and before the experiment were defrosted and cut into 5 mm in diameter and 2 mm thick pieces. *Saccharomyces cerevisiae* was purchased from Lesaffre (Wołczyn, Poland), acarbose was obtained from Bayer Pharma AG (Berlin, Germany), and α -amylase was obtained from Polfa S. A. (Warsaw, Poland).

2.2. Formulation of Microspheres Containing MF. Microspheres were prepared using Mini Spray Dryer B-290 (Büchi, Flawil, Switzerland). The flow rate was set to 4.5 mL/min, relative spray rate was fixed to $37\text{ m}^3/\text{h}$, and spray flow was fixed to 600 L/h. The inlet and outlet temperatures were established at 200°C and 96°C , respectively. The parameters of the spray drying were optimized in a number of preliminary tests. ALG of different concentrations (1%, 2%, and 3%) and different drug:polymer ratio (1:1, 1:2, and 2:1) was sprayed to obtain different formulations of microspheres (F1–F9).

2.3. Characteristics of Microspheres

2.3.1. Morphology and Size. Microspheres were analyzed by optical microscope (Motic BA400, Wetzlar, Germany) and by scanning electron microscope (SEM) (Hitachi S4200, Tokyo, Japan). Before imaging, samples were sputter-coated with gold in an argon atmosphere (Leica EM AC 2000, Wetzlar, Germany). The microspheres size distribution was studied

using Zetasizer NanoZS90 (Malvern Instruments, Malvern, UK) by laser light-diffraction technique after suspending in propane-1,2-diol (propane-1,2-diol was used because in aqueous medium swelling and dissolving of microspheres were observed).

2.3.2. HPLC Analysis. The concentration of MF in the medium was determined by the HPLC system Agilent Technologies 1200 equipped with a G1312A binary pump, a G1316A thermostat, a G1379B degasser, and a G1315B diode array detector (Agilent, Waldbronn, Germany). Data collection and analysis were performed using Chemstation 6.0 software. Isocratic separation was achieved on Waters Spherisorb® 5.0 μM ODS 4.6 \times 250 mm, 5 μm column (Waters Corporation, Milford, USA). Mobile phase was acetonitrile: methanol: phosphate buffer, pH 3.0 (20:20:60, v/v), the flow rate was 1.0 mL/min, and UV detection was performed at a wavelength of 240 nm [17]. The column temperature was maintained at 25°C . For injection into the HPLC system, 20 μL of sample was used. All reagents used for analysis were HPLC grade. The retention time of MF was 2.8 min. Standard calibration curve was linear over the range of 1–100 $\mu\text{g}/\text{mL}$ with the correlation coefficient (R^2) 0.999.

2.3.3. MF Loading and Percentage Yield. MF loading in the microspheres was determined by dissolving an accurately weighted amount of microspheres (20 mg) in 10 mL of distilled water and agitating it for 24 h at 150 rpm in a water bath [18]. The sample solution was further diluted and filtrated through 0.45 μm cellulose acetate Millipore filters (Billerica, USA). The percentage yield of MF in the ALG microspheres was determined by using the following formula:

$$L = \frac{Q_m}{W_m} \times 100, \quad (1)$$

where L is the percentage of drug loading, Q_m is the drug loaded in the microspheres, and W_m is the weight of the microspheres. The mean drug encapsulation efficiency was calculated by the following equation:

$$EE = \frac{Q_a}{Q_t} \times 100, \quad (2)$$

where EE is the percentage of encapsulation efficiency, Q_a is the actual drug content, and Q_t is the theoretical drug content.

Percentage production yield was calculated as the relationship of the achieved weight of the microspheres related to the entire amount of the theoretical weight of drug and polymer:

$$Y = \frac{W_m}{W_t} \times 100, \quad (3)$$

where Y is the percentage production yield, W_m is the weight of microspheres, and W_t is the theoretical weight of drug and polymer.

2.3.4. Microspheres Porosity. Microspheres porosity was determined by using the solvent replacement method [19].

Dried microspheres were immersed overnight in absolute ethanol and weighed after excess ethanol on the surface was blotted. Then, porosity was calculated based on the following equation:

$$P\% = \frac{(W_W - W_D)}{\rho \times V} \times 100, \quad (4)$$

where $P\%$ is the porosity, W_D is the weight of microspheres before immersion in absolute ethanol, W_W is the weight of microspheres after immersion in absolute ethanol, ρ is the density of absolute ethanol, and V is the volume of microspheres.

2.3.5. Zeta Potential. Zeta potential measurements were performed using a Zetasizer NanoZS90 (Malvern Instruments, Malvern, UK). Before measurements, microspheres were suspended in propane-1,2-diol. Data was obtained from Zetasizer software 6.20.

2.3.6. Swelling Properties. Swelling properties were evaluated at $37 \pm 1^\circ\text{C}$ in beakers containing 25 mL of 0.1 M HCl (pH 1.2) and stirred at 100 rpm. The microspheres were periodically weighted at predetermined time intervals until a constant weight was obtained [20]. The swelling ratio was calculated by using the following formula:

$$SR = \frac{W_s - W_0}{W_0} \times 100, \quad (5)$$

where SR is the swelling ratio, W_0 is the initial weight of microspheres, and W_s is the weight of microspheres after swelling.

2.3.7. Mucoadhesiveness. Evaluation of mucoadhesiveness was performed using TA.XT.Plus Texture Analyzer (Stable Micro Systems, Godalming, UK) and three different models of mucoadhesive material: gelatin disc, mucin gel, and porcine stomach mucosa. Experimental parameters of the process were chosen during preliminary tests and set as follows: pretest speed 0.5 mm/s, test speed 0.1 m/s, contact time 180 s, posttest 0.1 mm/s, and applied force 1 N. Gelatin discs were prepared by pouring 30% (w/w) aqueous solution into a Petri dish. Layer of mucin was prepared by absorbing 10% mucin gel on discs with cellulose fiber (5 mm in diameter). The tests were conducted at $37 \pm 1^\circ\text{C}$. Adhesive layers were adhered to an upper probe and moisturized (excepted mucin) with 0.1 M HCl (pH 1.2) [21]. The mucoadhesive properties were determined as the maximum detachment force (F_{\max}) and the work of mucoadhesion (W_{ad}), calculated from the area under the force versus distance curve, expressed in μJ .

2.4. In Vitro MF Release. For the *in vitro* MF release test, apparatus type I (Erweka Dissolution tester type DT 600HH, Heusenstamm, Germany) was used [22]. Microspheres were placed in the basket, immersed in 500 mL of 0.1 M HCl (pH 1.2), and stirred at 50 rpm. In each study, the amount of microspheres equivalent to 500 mg of MF was analyzed. Samples were withdrawn and filtered through 0.45 μm cellulose

acetate Millipore filters (Billerica, USA) at predetermined time intervals and replaced with fresh dissolution medium [23]. During the dissolution process, the temperature was maintained at $37 \pm 1^\circ\text{C}$. The amount of released MF was analyzed by HPLC method (as described in Section 2.3.2).

2.5. Mathematical Modeling of MF Release Profile. MF release data were analyzed according to zero-order kinetic, first-order kinetic, Higuchi model, Korsmeyer-Peppas equation, and Hixson-Crowell cube root law to characterize mechanism of the drug release. The constants of release kinetics and the regression coefficients (R^2) were calculated from the slope of plots by linear regression analysis.

Zero-order kinetic is as follows:

$$F = k \times t. \quad (6)$$

First-order kinetic is as follows:

$$\ln F = k \times t. \quad (7)$$

Higuchi model is as follows:

$$F = k \sqrt{t}. \quad (8)$$

Korsmeyer-Peppas model is as follows:

$$F = kt^n. \quad (9)$$

Hixson-Crowell model is as follows:

$$1 - (1 - F)^{1/3} = kt, \quad (10)$$

where F is the fraction of the drug release, k is the release constant, and t is the time. For the Korsmeyer-Peppas model, the fraction of drug remaining at time t was determined for every time interval (M_t/M_∞) and plotted against the log of time t . The slope of the line was taken as the value of n , diffusional release exponent used for interpretation of release mechanism [24, 25].

2.6. Differential Scanning Calorimetry (DSC). DSC analysis of MF, ALG, and microspheres formulation F6 (with the highest drug loading) was performed using an automatic thermal analyzer system (DSC TEQ2000, TA Instruments, New Castle, USA). Each sample was precisely weighted (5 mg) and placed in sealed aluminium pan. An empty pan sealed was used as a reference. Temperature calibrations were performed using indium and zinc as standard. Samples were heated from 25°C to 200°C at scanning rate of $10^\circ\text{C}/\text{min}$ under nitrogen flow of 20 mL/min [26].

2.7. Evaluation of ALG Influence on MF Hypoglycemic Activity

2.7.1. Glucose Uptake by *Saccharomyces Cerevisiae* Cells. Glucose uptake by *Saccharomyces cerevisiae* cells is often used model to *in vitro* study hypoglycemic activity [27–29]. Cells

TABLE 1: Characteristics of MF loaded ALG microspheres (formulations F1–F9).

Formulation	Drug: polymer ratio	Zeta potential (mV)	Production yield (%)	Encapsulation efficiency (%)	Percent loading (%)	Mean diameter (μm)	Porosity (%)
1% ALG solution							
F1	1:2	-5.3 ± 0.3	57.1 ± 1.6	119.8 ± 2.1	39.9 ± 1.7	3.5 ± 0.8	73.39 ± 2.3
F2	1:1	-3.4 ± 0.4	86.1 ± 2.4	111.9 ± 2.7	55.6 ± 3.4	3.4 ± 1.1	67.02 ± 4.2
F3	2:1	-1.4 ± 0.9	85.9 ± 1.4	109.4 ± 3.2	72.9 ± 1.6	1.7 ± 0.9	60.71 ± 3.5
2% ALG solution							
F4	1:2	-5.8 ± 2.3	61.8 ± 1.5	115.4 ± 1.9	38.4 ± 2.2	5.7 ± 1.1	75.04 ± 2.5
F5	1:1	-4.2 ± 0.9	68.0 ± 1.3	103.1 ± 2.1	51.5 ± 3.6	3.6 ± 0.5	65.55 ± 2.4
F6	2:1	-1.3 ± 0.7	61.7 ± 2.1	113.4 ± 2.3	75.6 ± 1.5	3.0 ± 1.6	61.81 ± 3.7
3% ALG solution							
F7	1:2	-7.7 ± 3.8	68.9 ± 1.1	111.9 ± 2.6	37.3 ± 3.9	4.0 ± 0.8	72.97 ± 3.5
F8	1:1	-3.7 ± 1.5	58.9 ± 1.4	111.1 ± 2.9	55.7 ± 3.9	2.5 ± 1.3	60.88 ± 2.9
F9	2:1	-1.8 ± 1.1	45.0 ± 2.1	110.4 ± 3.1	73.6 ± 7.5	1.6 ± 0.4	59.70 ± 2.5

were grown at $30 \pm 1^\circ\text{C}$ in a bottom flask containing 500 mL of sterilized modified minimal medium pH 5.3 for yeast growth (0.5 g KH_2PO_4 , 0.5 g $(\text{NH}_4)_2\text{SO}_4$, 0.5 g MgSO_4 , 1 g yeast extract, and 10 g glucose) [30]. Cells growth started from a stationary preculture of about 10^7 cfu/mL. Then, cells were washed three times with distilled water and centrifugated ($3000 \times g$, 5 min). The cytocrit was adjusted to 10% cells [31]. MF, microspheres placebo, and microspheres formulation F6 were added to 1 mL of various concentrations of glucose solution (5, 10, and 25 mM) and incubated for 10 min at $37 \pm 1^\circ\text{C}$. Reaction was started by adding 100 μL of yeast suspension; then, mixture was vortexed and incubated at $37 \pm 1^\circ\text{C}$ for 60 min. After incubation, mixtures were centrifuged ($2500 \times g$, 5 min) and concentration of glucose remaining in the medium was estimated by using glucose assay kit (One Touch Select, Johnson & Johnson, New Brunswick, USA) [27].

2.7.2. α -Amylase Inhibition. α -Amylase inhibition was evaluated by modified method based on the starch iodide reaction. Mixture composed of 1 mL 0.02 M sodium phosphate buffer (pH 6.9), 5 units of α -amylase solution, and examined samples (microspheres placebo, microspheres F6, and MF) was incubated at $37 \pm 1^\circ\text{C}$ for 10 min. Then, 1 mL of starch solution (1%, w/v) was added and mixture was incubated at $37 \pm 1^\circ\text{C}$ for 15 min. To stop the enzymatic reaction, 1 M HCl (20 μL) was added, followed by the addition of 20 μL of iodide reagent (5 mM I_2 and 5 mM KI) [32–34]. To eliminate the absorbance produced by analyzed substances, appropriate controls were also included. The triiodide anion with iodide reagent creates complexes with starch, producing an intense blue color. The absorbance was measured spectrophotometrically at 586 nm using Genesys 10S UV-Vis Spectrophotometer (Thermo Scientific, Madison, USA). The activity of examined samples was compared with acarbose (3, 5, and 10 mg), a well established α -amylase inhibitor [35]. Concentration of starch was calculated according to the calibrating curve. The control reaction (without examined substances) represented 100% of

enzyme activity. α -Amylase inhibition was assessed using the following formula:

$$\% \text{IA} = \frac{(C_s - C_c)}{C_s} \times 100, \quad (11)$$

where IA is the percent of α -amylase inhibition, C_c is the concentration of starch in the control reaction, and C_s is the concentration of starch in the test sample [34–36].

2.8. Statistical Analysis. Quantity variables were expressed as the mean and standard deviation. Statistical analysis was performed using nonparametric Kruskal-Wallis test and conducted by Statistica 10.0 software (StatSoft, Tulsa, USA). Differences between groups were considered to be significant at $p < 0.05$.

3. Results and Discussion

3.1. Microspheres Morphology, Size, and Surface Charge Analysis. Spray drying is a relatively simple, one-step process which includes spray drying of drug solution or suspension in a stream of gas and depends on several parameters, for example, atomization devices, aspirator and feed rate, drying temperature, spray air flow, and properties of the drying material [37]. This method enables entrapment of both hydrophilic and hydrophobic drugs in polymer matrix and compared to other techniques (emulsification-precipitation, emulsification-cross-linking, ionotropic gelation, solvent evaporation, and coacervation) it might be used in both laboratory and industrial scale. Moreover, it is characterized by the possibility of precisely controlling production parameters, high production yield (40–80%), and encapsulation efficiency (up to 100%) [37–40]. It was shown that formulated microspheres were characterized by relatively narrow size distribution and MF loading in all formulations was in the range between $37.3 \pm 3.8\%$ and $75.6 \pm 1.4\%$ (Table 1).

Drug: polymer ratio is a key factor influencing the characteristics of microspheres. The minimum MF loading was

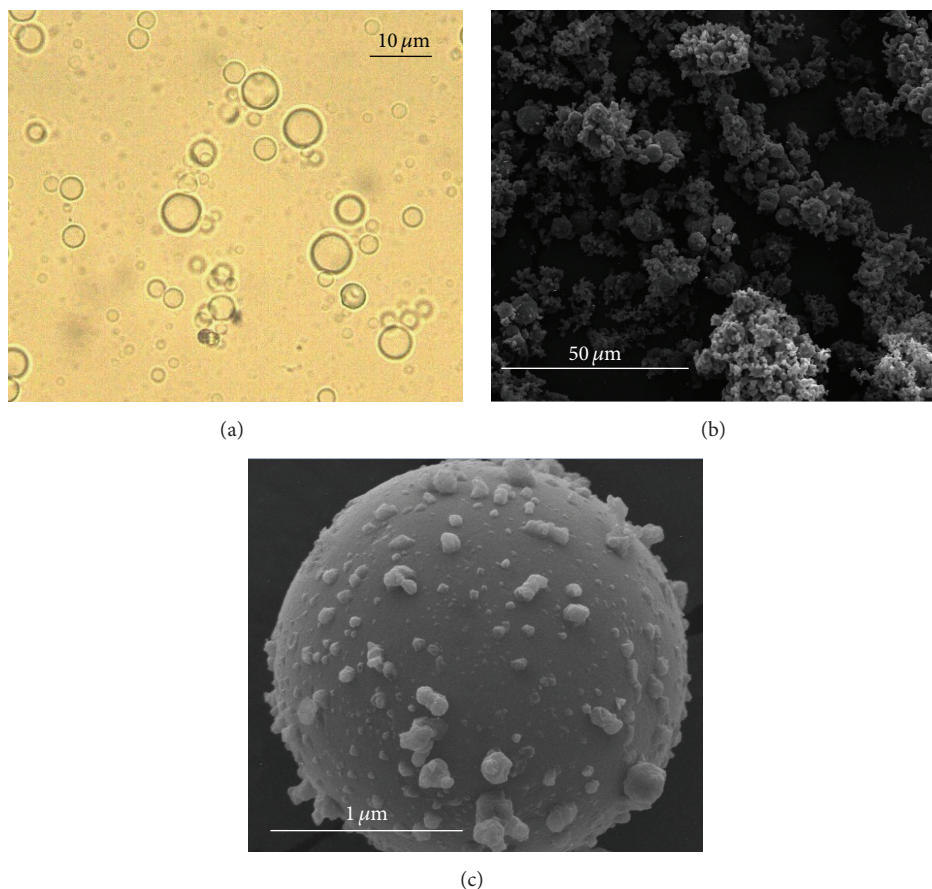


FIGURE 1: Representative images of microspheres formulation F6 under magnifications $\times 40$ (a), $\times 2000$ (b), and $\times 10000$ (c).

observed in formulations F7, F4, and F1 with drug : polymer ratio 1 : 2 ($37.3 \pm 3.9\%$, $38.4 \pm 2.2\%$, and $39.9 \pm 1.7\%$, resp.). The maximum drug loading was in formulations F6, F9, and F3 ($75.6 \pm 1.5\%$, $73.6 \pm 7.5\%$, and $72.9 \pm 1.6\%$) when drug : polymer ratio was 2 : 1. Interestingly, concentration of ALG solution had no significant impact on microspheres characteristics. Application of more concentrated solution of ALG (3%) did not result in higher production yield and diameter of obtained microspheres. It is worth noting that encapsulation efficiency in all microspheres was higher than 100%. It can be explained by a partial loss of the polymer during the preparation of microspheres, which decreased the theoretical polymer mass and changed the theoretical drug content to values higher than the previewed ones [41]. All formulations of microspheres had spherical shape. The morphology of microspheres F6 (with the highest MF loading) examined by optical and scanning electron microscopy is presented in Figure 1.

Zeta potential is an important parameter related to the stability of colloidal dispersions [42]. Zeta potential values of designed microspheres varied between -1.3 ± 0.7 and -7.7 ± 3.8 mV as shown in Table 1 (compared to -15.9 mV for ALG microspheres placebo). Although ALG is negatively charged, values of Zeta potential of microspheres with MF were close to zero. It is probably caused by complex formation between

the polyanionic ALG and oppositely charged MF. Formulation F6 (with the highest drug loading) was characterized by the lowest Zeta potential value.

3.2. Swelling and Mucoadhesive Properties. Mechanism of mucoadhesion is directly connected with water uptake into the polymer matrix, swelling, and gel layer formation [43]. Swelling is mainly attributed to the hydration of the hydrophilic groups of ALG, where water penetrates inside the microspheres and fills the inert pores among polymer chains. ALG swelling and dissolution are pH dependent. At acidic pH, as a result of reduction of the electrical repulsion between the negatively charged ALG molecules and positively charged ions in the medium, polymer is protonated and creates insoluble form of alginic acid [44, 45]. After protonation of carboxylic acid groups, the polymer shrinks, absorption of water is decreased, and in consequence swelling degree decreases [43]. The swelling profiles, represented as the swelling ratio (SR) versus time, are reported in Figure 2.

Figure 2 illustrates the swelling properties of the designed microspheres in 0.1 M HCl (pH 1.2) at different time intervals. All the curves gave linear increase, indicating a loosening of the matrix with the creation of larger pores [46]. The results indicated that formulations of microspheres swelled

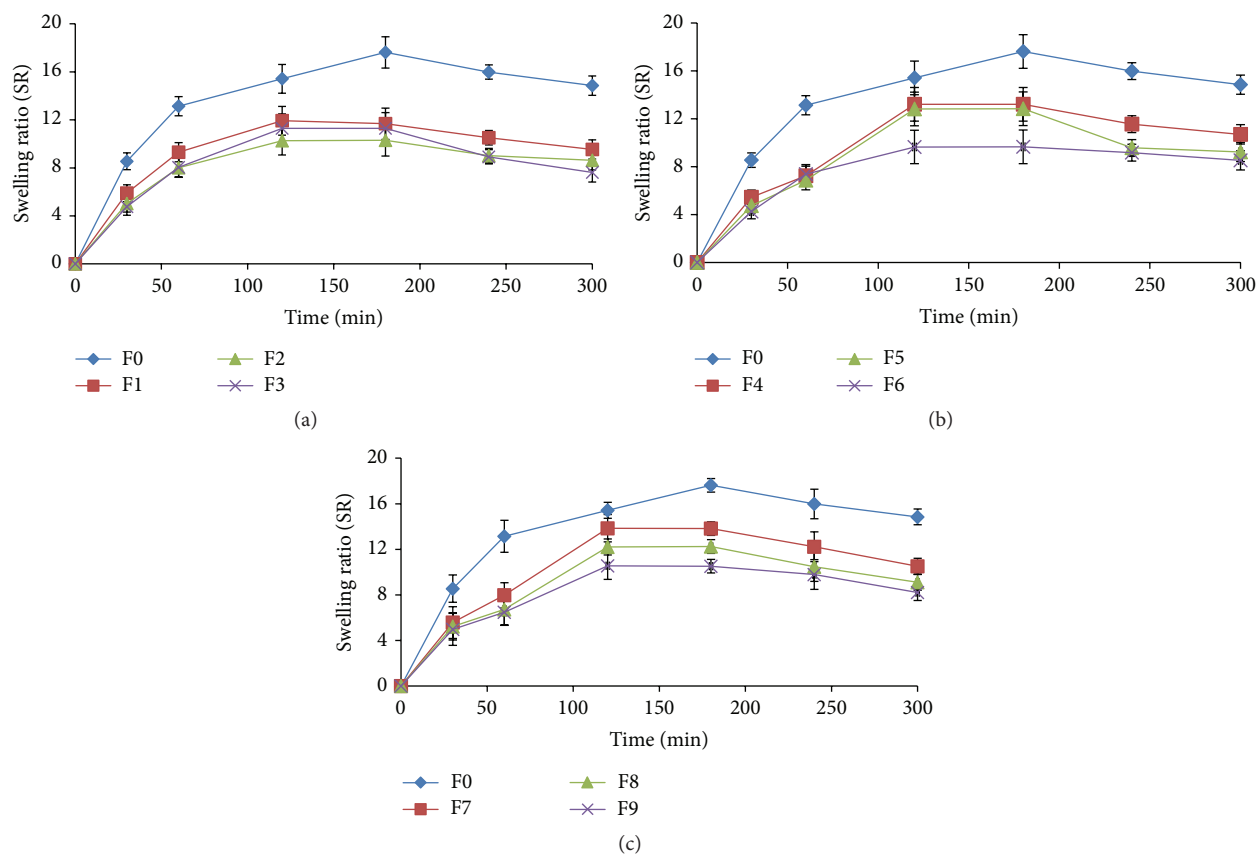


FIGURE 2: Swelling ratio (SR) of microspheres placebo (F0) and formulations F1–F3 (a), F4–F6 (b), and F7–F9 (c).

gradually. Obtained curves showed an initial rapid increase within 30 min of the experiment due to the entry of water *via* metastable pores known as hysteresis of swelling mechanism and reached the highest value after 120 min for formulations F1–F9 and after 180 min for microspheres placebo. Formulation F7 (with the lowest MF content) showed the highest swelling ratio, while microspheres F6 (with the highest MF loading) attained lower value of SR. Swelling in acidic pH as a result of osmosis caused by unbound carboxyl groups enables forming a swollen gel and surface erosion, which results in disintegration of microspheres and sustained MF release.

The mucoadhesive drug delivery systems increase drug residence time and in consequence improve its bioavailability. ALG as polyanionic polymer is characterized by higher bioadhesive properties than polycationic (chitosan, poly(l-lysine)) or nonionic polymers (macrogol, hypromellose and polyvinyl alcohol) [47, 48]. Mechanism of ALG mucoadhesion is defined by interaction between carboxyl groups of polymer and mucin through electrostatic adsorption, *van der Waals*, and hydrogen bonds. The surface of mucin is positively charged and its flexible backbone chains enable interaction with ALG carboxyl groups. Initially, contact (wetting) between polymer and mucus and, subsequently, polymer swelling make the polymer strands relax [47, 48]. This is followed by the penetration of ALG into the mucus network and finally the formation of secondary chemical

bonds between the mucus and the polymer. The influence of MF on the mucoadhesive properties of ALG microspheres is shown in Table 2.

The mucoadhesive properties were presented as maximum detachment force (F_{max}) and work of adhesion (W_{ad}) and as the adhesive layers gelatin discs, mucin gel, and porcine stomach mucosa were used. Porcine stomach mucosa model is often used in order to imitate *in vivo* conditions [49]. It was shown that ALG microspheres readily adhered to all tested mucoadhesive materials and that detachment force and work of adhesion increased when drug loading was decreased. When gelatin was used as adhesive layer, relatively large maximum detachment force and small values of the work of adhesion were observed. This fact might indicate that microspheres adhere to this layer for very short time, forming only weak bonds between gelatin and alginate. The lower mucoadhesiveness of microspheres F3, F6, and F9 is probably due to the high MF content causing disturbances in ALG gel structure. It is worth noting that significant ($p < 0.05$) differences of detachment force and work of adhesion values between gelatin and porcine stomach mucosa were observed; therefore, it might be suggested that mucin gel is a better substitute of mucous membrane.

Moreover, the obtained results indicate that there is direct correlation between mucoadhesive properties and SR. The highest values of F_{max} (0.9 ± 0.1) and W_{ad} (768.2 ± 5.4) were observed for formulation F7 with the highest SR value.

TABLE 2: Mucoadhesive properties of microspheres placebo (F0) and microspheres formulations F1–F9.

Formulation	Type of adhesive layer					
	Gelatin		Mucin		Porcine stomach mucosa	
	F_{max} [N]*	W_{ad} [μ]**	F_{max} [N]*	W_{ad} [μ]**	F_{max} [N]*	W_{ad} [μ]**
F0	0.9 ± 0.3	362.9 ± 1.8	1.1 ± 3.7	583.4 ± 1.5	1.3 ± 1.3	779.5 ± 2.4
F1	0.5 ± 0.2	237.5 ± 1.0	0.5 ± 0.2	275.1 ± 1.6	0.7 ± 0.1	428.0 ± 2.6
F2	0.5 ± 0.2	203.0 ± 0.6	0.5 ± 0.3	207.2 ± 0.5	0.7 ± 0.2	360.9 ± 1.3
F3	0.4 ± 0.3	179.5 ± 0.4	0.5 ± 0.4	179.5 ± 0.1	0.7 ± 0.1	272.3 ± 0.5
F4	0.5 ± 0.2	392.8 ± 2.1	0.6 ± 0.2	410.0 ± 2.8	0.8 ± 0.2	681.6 ± 3.9
F5	0.4 ± 0.2	264.0 ± 0.3	0.6 ± 0.3	367.7 ± 1.5	0.7 ± 0.3	560.3 ± 4.1
F6	0.5 ± 0.2	238.3 ± 0.5	0.6 ± 0.3	342.3 ± 2.9	0.6 ± 0.2	467.5 ± 1.7
F7	0.5 ± 0.3	319.4 ± 1.5	0.6 ± 0.2	501.0 ± 3.1	0.9 ± 0.1	768.2 ± 5.4
F8	0.5 ± 0.2	303.7 ± 1.3	0.7 ± 0.4	489.6 ± 3.8	0.8 ± 0.2	692.1 ± 4.6
F9	0.4 ± 0.1	234.2 ± 0.6	0.7 ± 0.3	441.8 ± 2.3	0.6 ± 0.3	657.7 ± 4.3

*Maximum detachment force and **work of adhesion.

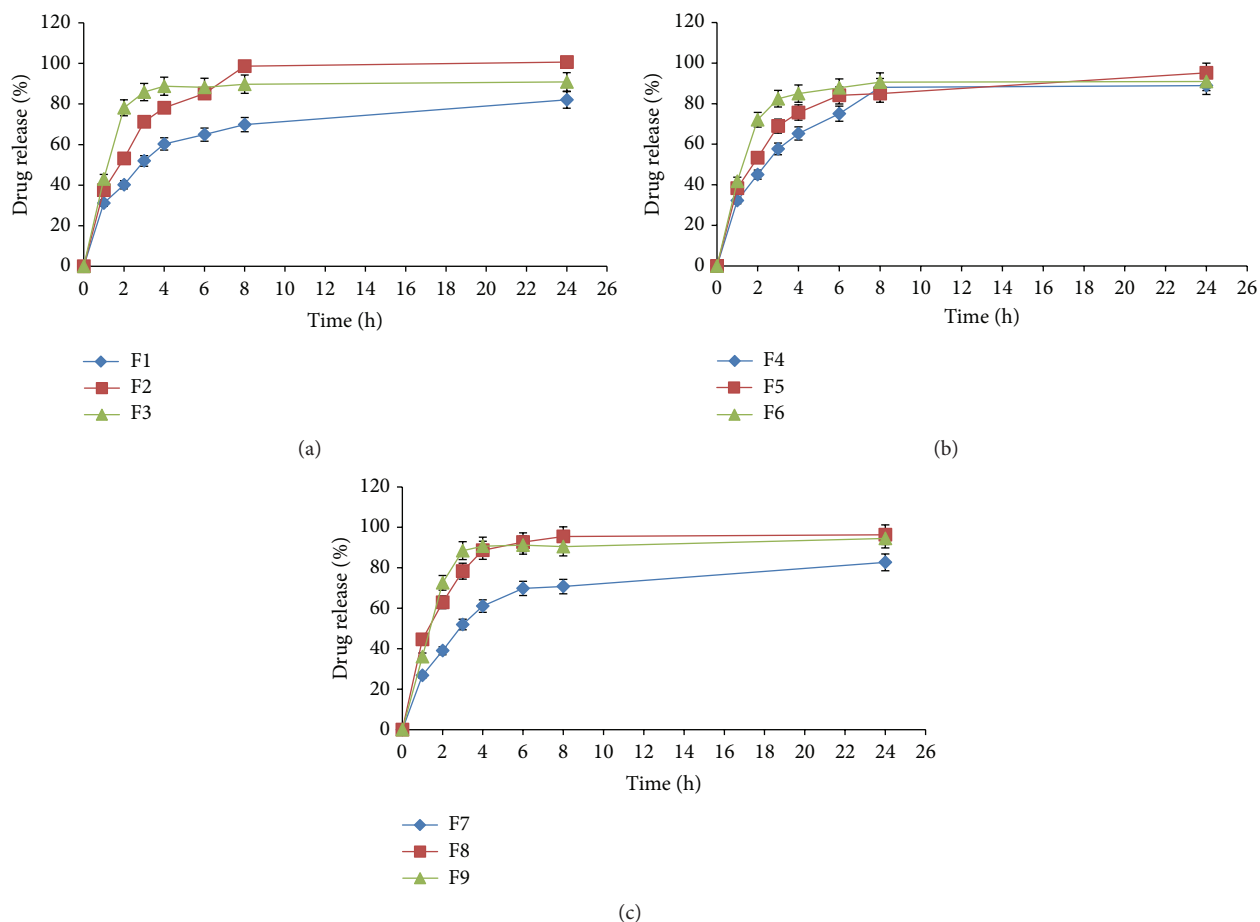


FIGURE 3: MF release from microspheres formulations F1–F3 (a), F4–F6 (b), and F7–F9 (c), $n = 3$.

3.3. *In Vitro* MF Release. The release profiles of MF from microspheres formulations F1–F9 are shown in Figure 3. In all formulations, the release profile showed a burst effect, which is the first phase of the drug release and occurs due to the free MF binding at the microparticles surface. The highest burst effect was observed in formulation F6, with the highest

drug loading; after 30 min, $41.7 \pm 0.4\%$ of MF was released. At acidic pH, ALG swells and creates gelling alginate matrix, which prevents disintegration of microspheres and controls water penetration inside the microsphere structure. Formulations F1, F4, and F7, with the lowest MF content, were characterized by the higher swelling ratio and ensured

TABLE 3: Models of MF release from microspheres formulations F1–F9.

Formulation	Zero-order kinetics		First-order kinetics		Highuchi model		Korsmeyer-Peppas model			Hixson-Crowell model	
	R^2	K	R^2	K	R^2	K	R^2	K	n	R^2	K
F1	0.92	1.67	0.97	0.17	0.98	22.98	0.94	0.31	0.08	0.96	0.18
F2	0.86	1.68	0.98	0.55	0.95	29.37	0.88	0.34	0.08	0.94	0.58
F3	0.41	4.07	0.59	0.18	0.56	16.82	0.51	0.27	0.11	0.52	0.16
F4	0.87	6.69	0.95	0.22	0.96	25.03	0.90	0.32	0.19	0.94	0.22
F5	0.82	6.55	0.95	0.13	0.93	25.15	0.86	0.32	0.17	0.95	0.27
F6	0.52	4.62	0.73	0.21	0.66	18.76	0.59	0.28	0.12	0.65	0.19
F7	0.90	7.34	0.93	0.22	0.96	27.11	0.91	0.33	0.22	0.91	0.23
F8	0.70	6.01	0.93	0.37	0.84	23.64	0.78	0.31	0.14	0.86	0.29
F9	0.45	5.15	0.66	0.25	0.60	21.33	0.58	0.31	0.14	0.58	0.22

R^2 : correlation coefficient, K : release constant, and n : the release exponent.

sustained drug release; after 8 h of the study, the amount of released MF was $82.6 \pm 1.6\%$, $88.9 \pm 2.2\%$, and $89.1 \pm 3.2\%$, respectively.

Afterwards, MF release profiles were fitted to zero-order and first-order equations and Higuchi, Korsmeyer-Peppas, and Hixson-Crowell models (Table 3).

In the Higuchi model, the best fit curve with R^2 (0.98) was observed for formulation F1. It was also noticed that mechanism of MF release from formulations F1, F2, F4, F5, and F7 was diffusion controlled first-order kinetics as the plots showed higher regression correlation coefficient. However, based on Korsmeyer-Peppas equation in case of sphere shape microspheres, the value of diffusional exponent $n \geq 0.85$ means that drug release is independent of time (case II transport), while value $n \leq 0.43$ means that release is controlled by Fickian diffusion. A value between 0.43 and 0.85 indicates combination of diffusion and swelling mechanism. The obtained values of diffusion exponent from 0.08 to 0.22 confirm diffusion as mechanism of MF release. The high values of R^2 in the Hixson-Crowell model indicate that this equation can also describe MF release and suggest that it was controlled also by disintegration process of the microspheres. The Hixson-Crowell cube root law describes the release from the systems, where drug release depends on the change in surface area and diameter of the particles with time and it is mainly applied to systems which are subjected to dissolution or erosion processes. In this case, MF release rate is limited by the microspheres erosion. The obtained data have shown that MF release from ALG microspheres is complex and includes simultaneously erosion and diffusion mechanism. MF release can be controlled by water penetration, responsible for polymer hydration, erosion of microspheres, and drug diffusion [50, 51].

3.4. Differential Scanning Calorimetry (DSC). DSC is an important tool to obtain information about possible interactions between drug and polymer, according to the appearance, shift, or disappearance of endothermic or exothermic peaks. Thermograms of MF, ALG, microspheres placebo, and

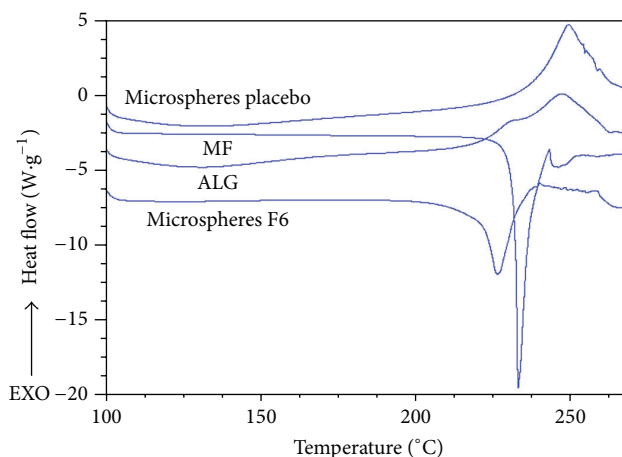


FIGURE 4: DSC thermograms of sodium alginate (ALG), metformin hydrochloride (MF), microspheres placebo, and microspheres formulation F6.

microspheres formulation F6 (with the highest MF loading) are shown in Figure 4.

Under the experimental conditions, a sharp endothermic peak for pure MF was observed at 233.02°C corresponding to its melting point. Thermogram of microspheres formulation F6 has shown that peak of MF did not shift significantly (226.55°C). Lowering of MF melting point in microspheres might be due to its mixing with ALG, which lowered the purity of each component; MF crystallinity was reduced and the drug might convert into the amorphous form. In the DSC thermogram, a small endothermic peak of ALG at 129.55°C , attributed to the dehydration process, and strong exothermic peak at 247.80°C , corresponding to the decomposition of the polymer, were observed. Melting peak of ALG (129.27°C) was not detected in microspheres F6, which might suggest that ALG has dehydrated during the spray drying process [52].

3.5. Influence of ALG on MF Hypoglycemic Activity. Type 2 diabetes is a chronic metabolic disorder characterized by

TABLE 4: *In vitro* glucose uptake by yeast cells incubated with microspheres placebo, microspheres F6, and metformin hydrochloride (MF).

	Concentration of glucose (mM) remaining in the medium		
	5 mM glucose	10 mM glucose	20 mM glucose
Control*	3.79 ± 1.67	7.48 ± 0.72	14.72 ± 1.32
Microspheres placebo	4.56 ± 0.49	9.01 ± 1.61	17.84 ± 2.86
Microspheres F6	1.65 ± 2.79	3.13 ± 1.69	6.51 ± 1.01
MF**	1.22 ± 0.18	1.50 ± 0.23	3.91 ± 0.69

*Suspension of *Saccharomyces cerevisiae* cells in glucose solution; **MF was used in an amount (10 mg) corresponding to its loading in microspheres formulation F6.

high level of blood glucose, which may lead to damage of the body organs [53]. Uncontrolled hyperglycemia can lead to the development of complications, such as dysfunction of blood vessels (retinopathy and neuropathy) and nervous system, and increasing the risk of cardiovascular diseases [54–56]. Although many antidiabetic drugs are available, most of them possess serious side effects or do not provide satisfactory glucose control. Therefore, many studies focus on the development of novel dosage forms for antidiabetic drugs. Hypoglycemic effect can be studied *in vitro* using a variety of models, which play a very important role as initial screening tools in the evaluation of antidiabetic activity of drugs and new dosage forms. To determine hypoglycemic activity of ALG microspheres with MF and to evaluate influence of ALG on MF hypoglycemic activity, glucose uptake by *Saccharomyces cerevisiae* cells and α -amylase inhibition tests were performed.

3.5.1. Glucose Uptake by *Saccharomyces Cerevisiae* Cells. Polysaccharides can influence intestinal glucose absorption and the mechanism of this action includes forming a viscous gel which may slow the access of glucose to the epithelium, thereby decreasing postprandial glucose blood concentration. Viscous gel may also delay gastric emptying, slow down carbohydrate uptake, and retard carbohydrate access to digestive enzymes which may contribute to the postprandial effect [57, 58]. Glucose uptake by *Saccharomyces cerevisiae* cells is complex process based on facilitated diffusion and controlled by multiple hexose transporters (Hxts) [59]. Roy et al. demonstrated that mechanism of glucose transport by Hxts is similar to human glucose transporters (GLUTs) [60]. As GLUT-2 is localized in the intestinal mucosa and it is responsible for monosaccharides absorption into the bloodstream [61], determination of glucose transport across the *Saccharomyces cerevisiae* cell membranes has been receiving attention as alternative method for the *in vitro* hypoglycemic effect evaluation. The amount of glucose remaining in the medium after incubation of *Saccharomyces cerevisiae* cells with different glucose concentrations (5, 10, and 20 mM) and microspheres placebo, microspheres formulation F6, and MF is presented in Table 4.

Obtained results indicate that MF significantly increased glucose uptake by *Saccharomyces cerevisiae* cells compared to the control sample. The uptake of glucose by *Saccharomyces cerevisiae* cells incubated with formulation F6 was lower than that by cells incubated with pure MF. This effect was observed at all examined glucose concentrations (5, 10, and 20 mM). In case of 10 mM glucose solution, concentration of glucose remaining in the medium was 3.13 ± 1.69 mM for microspheres F6, 1.50 ± 0.23 mM for pure MF, and 9.01 ± 1.61 mM for microspheres placebo. The highest glucose uptake inhibition was observed when *Saccharomyces cerevisiae* cells were incubated with microspheres placebo, which suggests that pure ALG demonstrates the highest intestinal glucose absorption inhibitory potential.

3.5.2. α -Amylase Inhibition. Therapeutic strategy of hyperglycemia in the treatment of type 2 diabetes involves decreasing the postprandial glucose concentration in the blood [53]. α -Amylase is an intestinal enzyme which plays an important role in the carbohydrate digestion. It hydrolyses α -bonds of polysaccharides (such as glycogen and starch) to glucose and maltose. Inhibitors of this enzyme delay carbohydrate digestion through binding to α -bonds and prevent decomposition of polysaccharides into mono- and disaccharides [62, 63]. This action prolongs the overall time for carbohydrate digestion and results in a reduction of glucose absorption. Consequently, inhibition of α -amylase reduces the postprandial fluctuations of blood glucose and decreases glycemic index of food [64–66]. It was shown that seaweeds can reduce activity of α -amylase; therefore, impact of ALG microspheres with MF on enzyme activity was studied. The results of α -amylase inhibition test are illustrated in Figure 5.

Inhibition of enzyme activity by microspheres F6 was associated with the amount of polymer; samples containing higher amount of ALG more effectively inhibited α -amylase. The values of enzyme inhibition were ranged from 5.35 ± 0.32% (for 7.56 mg of MF) to 63.82 ± 2.83% (for 10 mg of microspheres placebo) (Figure 5(a)). Microspheres formulation F6 was characterized by stronger α -amylase inhibition activity (36.34 ± 2.45%) compared to pure MF.

4. Conclusions

MF release and mucoadhesive properties of ALG microspheres obtained by the spray drying can be altered by varying the drug:polymer ratio. Optimal formulation characterized by the highest drug loading was formulation F6 (drug:polymer ratio 2:1 and 2% alginate solution). All microspheres possessed swelling and mucoadhesive properties depending on drug and polymer content. The release profile of MF from microspheres was prolonged and controlled by Fickian diffusion. Based on the *in vitro* hypoglycemic activity evaluation, it can be concluded that ALG microspheres enhance activity of MF. It was observed that ALG affects inhibition of glucose uptake in *Saccharomyces*

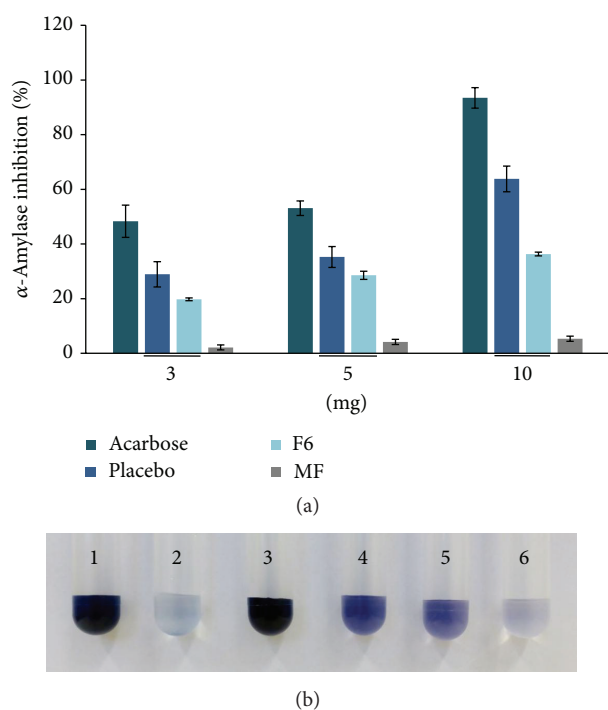


FIGURE 5: The effect of microspheres placebo (placebo), microspheres formulation F6 (F6), and metformin hydrochloride (MF) in an amount corresponding to its loading in microspheres formulation F6 (2.27 mg, 3.78 mg, and 7.56 mg, resp.) on the *in vitro* α -amylase inhibition (a), and representative images of reactive mixture: without α -amylase (1), with α -amylase (2), with acarbose (3), with microspheres placebo (4), with microspheres formulation F6 (5), and with 7.56 mg of pure metformin hydrochloride (in an amount corresponding to its loading in microspheres formulation F6) (6) (b), $n = 3$.

cerevisiae cells and reduces α -amylase activity. As inhibition of intestinal glucose absorption is crucial in type 2 diabetes treatment, ALG might be valuable excipient in designing dosage forms with MF. Designed microspheres seem to be promising as alternative, multicompartiment dosage form for metformin hydrochloride delivery. However, *in vivo* evaluation of ALG influence on hypoglycemic activity of MF in the microspheres is necessary and will be described in a due course.

Competing Interests

The authors declare no competing interests.

Acknowledgments

This research was conducted with the use of equipment purchased by the Medical University of Białystok as part of the OP DEP 2007–2013, Priority Axis I.3, Contract no. POPW.01.03.00-20-008/09, and supported by Medical University of Białystok Grant (no. N/ST/MN/16/001/2215).

References

- [1] K. N. Sachan, S. Pushkar, A. Jha, and A. Bhattacharya, "Sodium alginate: the wonder polymer for controlled drug delivery," *Journal of Pharmacy Research*, vol. 2, no. 8, pp. 1191–1199, 2009.
- [2] A. Sosnik, "Alginate particles as platform for drug delivery by the oral route: state-of-the-art," *ISRN Pharmaceutics*, vol. 2014, Article ID 926157, 17 pages, 2014.
- [3] H. H. Tønnesen and J. Karlsen, "Alginate in drug delivery systems," *Drug Development and Industrial Pharmacy*, vol. 28, no. 6, pp. 621–630, 2002.
- [4] H. K. Solanki and D. A. Shah, "Formulation optimization and evaluation of probiotic *Lactobacillus sporogenes*-loaded sodium alginate with carboxymethyl cellulose mucoadhesive beads using design expert software," *Journal of Food Processing*, vol. 2016, Article ID 6041671, 14 pages, 2016.
- [5] A. Ahmadi, S. Z. Moghadamtousi, S. Abubakar, and K. Zandi, "Antiviral potential of algae polysaccharides isolated from marine sources: a review," *BioMed Research International*, vol. 2015, Article ID 825203, 10 pages, 2015.
- [6] M. G. Jensen, M. Kristensen, and A. Astrup, "Effect of alginate supplementation on weight loss in obese subjects completing a 12-wk energy-restricted diet: a randomized controlled trial," *American Journal of Clinical Nutrition*, vol. 96, no. 1, pp. 5–13, 2012.
- [7] J. A. Williams, C.-S. Lai, H. Corwin et al., "Inclusion of guar gum and alginate into A crispy bar improves postprandial glycemia in human," *Journal of Nutrition*, vol. 134, no. 4, pp. 886–889, 2004.
- [8] N. Yavorska, "Sodium alginate—a potential tool for weight management: effect on subjective appetite, food intake, and glycemic and insulin regulation," *Journal of Undergraduate Life Sciences*, vol. 6, no. 1, pp. 66–69, 2012.
- [9] G. G. Graham, J. Punt, M. Arora et al., "Clinical pharmacokinetics of metformin," *Clinical Pharmacokinetics*, vol. 50, no. 2, pp. 81–98, 2011.
- [10] M. Foretz, B. Guigas, L. Bertrand, M. Pollak, and B. Viollet, "Metformin: from mechanisms of action to therapies," *Cell Metabolism*, vol. 20, no. 6, pp. 953–966, 2014.
- [11] Z.-H. Zhang, Y.-S. Sun, H. Pang, W. L. L. Munyendo, H.-X. Lv, and S.-L. Zhu, "Preparation and evaluation of berberine alginate beads for stomach-specific delivery," *Molecules*, vol. 16, no. 12, pp. 10347–10356, 2011.
- [12] S. C. Basak, J. Rahman, and M. Ramalingam, "Design and *in vitro* testing of a floatable gastroretentive tablet of metformin hydrochloride," *Pharmazie*, vol. 62, no. 2, pp. 145–148, 2007.
- [13] H. K. Sharma, S. Lahkar, and L. Kanta Nath, "Formulation and *in vitro* evaluation of metformin hydrochloride loaded microspheres prepared with polysaccharide extracted from natural sources," *Acta Pharmaceutica*, vol. 63, no. 2, pp. 209–222, 2013.
- [14] J. D. Ghodake, J. S. Vidhate, D. A. Shinde, and A. N. Kadam, "Formulation and evaluation of floating microsphere containing anti-diabetic (metformin hydrochloride) drug," *International Journal of PharmTech Research*, vol. 2, no. 1, pp. 378–384, 2010.
- [15] J. Balasubramaniam, V. U. Rao, M. Vasudha, J. Babu, and P. S. Rajinikanth, "Sodium alginate microspheres of metformin HCl: formulation and *in vitro* evaluation," *Current Drug Delivery*, vol. 4, no. 3, pp. 249–256, 2007.

- [16] N. Garud and A. Garud, "Preparation and in-vitro evaluation of metformin microspheres using non-aqueous solvent evaporation technique," *Tropical Journal of Pharmaceutical Research*, vol. 11, no. 4, pp. 577–583, 2012.
- [17] R. I. El-Bagary, E. F. Elkady, and B. M. Ayoub, "Liquid chromatographic methods for the determination of vildagliptin in the presence of its synthetic intermediate and the simultaneous determination of pioglitazone hydrochloride and metformin hydrochloride," *International Journal of Biomedical Science*, vol. 7, no. 3, pp. 201–208, 2011.
- [18] M. Przybyslawska, A. Amelian, and K. Winnicka, "Preparation of ciprofloxacin-encapsulated poly- ϵ -caprolactone microcapsules by the solvent evaporation technique," *e-Polymers*, vol. 13, no. 1, pp. 319–330, 2013.
- [19] S. Nanda, N. Sood, B. V. K. Reddy, and T. S. Markandeywar, "Preparation and characterization of poly(vinyl alcohol)-chondroitin sulphate hydrogel as scaffolds for articular cartilage regeneration," *Indian Journal of Materials Science*, vol. 2013, Article ID 516021, 8 pages, 2013.
- [20] M. Szekalska, K. Winnicka, A. Czajkowska-Kośnik, K. Sosnowska, and A. Amelian, "Evaluation of alginate microspheres with metronidazole obtained by the spray drying technique," *Acta Poloniae Pharmaceutica*, vol. 72, no. 3, pp. 569–578, 2015.
- [21] E. Szymańska, K. Sosnowska, W. Miłyk, M. Rusak, A. Basa, and K. Winnicka, "The effect of β -glycerophosphate crosslinking on chitosan cytotoxicity and properties of hydrogels for vaginal application," *Polymers*, vol. 7, no. 11, pp. 2223–2244, 2015.
- [22] *The European Pharmacopeia*, vol. 2, Council of Europe, Strasbourg, France, 6th edition, 2007.
- [23] E. Szymańska and K. Winnicka, "Preparation and in vitro evaluation of chitosan microgranules with clotrimazole," *Acta Poloniae Pharmaceutica*, vol. 69, no. 3, pp. 509–513, 2012.
- [24] P. Costa and J. M. Sousa Lobo, "Modeling and comparison of dissolution profiles," *European Journal of Pharmaceutical Sciences*, vol. 13, no. 2, pp. 123–133, 2001.
- [25] J. Siepmann and N. A. Peppas, "Modeling of drug release from delivery systems based on hydroxypropyl methylcellulose (HPMC)," *Advanced Drug Delivery Reviews*, vol. 48, no. 2-3, pp. 139–157, 2001.
- [26] E. Mazurek-Wadołkowska, K. Winnicka, A. Czajkowska-Kośnik, U. Czyżewska, and W. Miłyk, "Application of differential scanning calorimetry in evaluation of solid state interactions in tablets containing acetaminophen," *Acta Poloniae Pharmaceutica—Drug Research*, vol. 70, no. 5, pp. 787–793, 2013.
- [27] S. Özcan and M. Johnston, "Function and regulation of yeast hexose transporters," *Microbiology and Molecular Biology Reviews*, vol. 63, no. 3, pp. 554–569, 1999.
- [28] D. K. Patel, R. Kumar, D. Laloo, and S. Hemalatha, "Evaluation of phytochemical and antioxidant activities of the different fractions of *Hybanthus enneaspermus* (Linn.) F. Muell. (Violaceae)," *Asian Pacific Journal of Tropical Medicine*, vol. 4, no. 5, pp. 391–396, 2011.
- [29] M. Bhutkar and S. Bhise, "In vitro hypoglycemic effects of *Albizia lebbek* and *Mucuna pruriens*," *Asian Pacific Journal of Tropical Biomedicine*, vol. 3, no. 11, pp. 866–870, 2013.
- [30] M. Soupionis, E. Polichroniadou, M. Tokatlidou, M. Kanellaki, and A. A. Koutinas, "Glucose uptake rate by *Saccharomyces cerevisiae* in the presence of promoters of alcoholic fermentation using ^{14}C -labelled glucose," *Biotechnology Letters*, vol. 20, no. 5, pp. 495–497, 1998.
- [31] C. Reinhardt, B. Völker, H.-J. Martin, J. Kneiseler, and G. F. Fuhrmann, "Different activation energies in glucose uptake in *Saccharomyces cerevisiae* DFY1 suggest two transport systems," *Biochimica et Biophysica Acta (BBA)—Biomembranes*, vol. 1325, no. 1, pp. 126–134, 1997.
- [32] S. Lordan, T. J. Smyth, A. Soler-Vila, C. Stanton, and R. Paul Ross, "The α -amylase and α -glucosidase inhibitory effects of Irish seaweed extracts," *Food Chemistry*, vol. 141, no. 3, pp. 2170–2176, 2013.
- [33] P. Sudha, S. S. Zinjarde, S. Y. Bhargava, and A. R. Kumar, "Potent α -amylase inhibitory activity of Indian Ayurvedic medicinal plants," *BMC Complementary and Alternative Medicine*, vol. 11, article 5, pp. 1–10, 2011.
- [34] N. Dekdouk, N. Malafronte, D. Russo et al., "Phenolic compounds from *Olea europaea* L. possess antioxidant activity and inhibit carbohydrate metabolizing enzymes *in vitro*," *Evidence-Based Complementary and Alternative Medicine*, vol. 2015, Article ID 684925, 9 pages, 2015.
- [35] S. Akkarachiyasit, P. Charoenlertkul, S. Yibchok-Anun, and S. Adisakwattana, "Inhibitory activities of cyanidin and its glycosides and synergistic effect with acarbose against intestinal α -glucosidase and pancreatic α -amylase," *International Journal of Molecular Sciences*, vol. 11, no. 9, pp. 3387–3396, 2010.
- [36] T. Ma, X. Sun, C. Tian, J. Luo, C. Zheng, and J. Zhan, "Enrichment and purification of polyphenol extract from *Sphallerocarpus gracilis* stems and leaves and *in vitro* evaluation of DNA damage-protective activity and inhibitory effects of α -amylase and α -glucosidase," *Molecules*, vol. 20, no. 12, pp. 21442–21457, 2015.
- [37] K. Cal and K. Sollohub, "Spray drying technique. I: hardware and process parameters," *Journal of Pharmaceutical Sciences*, vol. 99, no. 2, pp. 575–586, 2010.
- [38] S. K. Singh, P. R. Vuddanda, S. Singh, and A. K. Srivastava, "A comparison between use of spray and freeze drying techniques for preparation of solid self-microemulsifying formulation of valsartan and *in vitro* and *in vivo* evaluation," *BioMed Research International*, vol. 2013, Article ID 909045, 13 pages, 2013.
- [39] Y. Baimark and Y. Srisuwan, "Preparation of polysaccharide-based microspheres by a water-in-oil emulsion solvent diffusion method for drug carriers," *International Journal of Polymer Science*, vol. 2013, Article ID 761870, 6 pages, 2013.
- [40] A. Sosnik and K. P. Seremeta, "Advantages and challenges of the spray-drying technology for the production of pure drug particles and drug-loaded polymeric carriers," *Advances in Colloid and Interface Science*, vol. 223, article no. 1537, pp. 40–54, 2015.
- [41] C. M. Silva, A. J. Ribeiro, D. Ferreira, and F. Veiga, "Insulin encapsulation in reinforced alginate microspheres prepared by internal gelation," *European Journal of Pharmaceutical Sciences*, vol. 29, no. 2, pp. 148–159, 2006.
- [42] J. D. Clogston and A. K. Patri, "Zeta potential measurement," in *Characterization of Nanoparticles Intended for Drug Delivery*, S. E. McNeil, Ed., vol. 697 of *Methods in Molecular Biology*, pp. 63–70, 2011.
- [43] R. Shaikh, T. R. Raj Singh, M. J. Garland, A. D. Woolfson, and R. F. Donnelly, "Mucoadhesive drug delivery systems," *Journal of Pharmacy and Bioallied Sciences*, vol. 3, no. 1, pp. 89–100, 2011.
- [44] K. Ghosal and S. D. Ray, "Alginate/hydrophobic HPMC (60 M) particulate systems: new matrix for site-specific and controlled drug delivery," *Brazilian Journal of Pharmaceutical Sciences*, vol. 47, no. 4, pp. 833–844, 2011.
- [45] S. Takka and A. Gürel, "Evaluation of chitosan/alginate beads using experimental design: formulation and *in vitro* characterization," *AAPS PharmSciTech*, vol. 11, no. 1, pp. 460–466, 2010.

- [46] S. A. Mortazavi and J. D. Smart, "An investigation into the role of water movement and mucus gel dehydration in mucoadhesion," *Journal of Controlled Release*, vol. 25, no. 3, pp. 197–203, 1993.
- [47] K. E. Haugstad, A. G. Håti, C. T. Nordgård et al., "Direct determination of chitosan-mucin interactions using a single-molecule strategy: comparison to alginate-mucin interactions," *Polymers*, vol. 7, no. 2, pp. 161–185, 2015.
- [48] S. Roy, K. Pal, A. Anis, K. Pramanik, and B. Prabhakar, "Polymers in mucoadhesive drug-delivery systems: a brief note," *Designed Monomers and Polymers*, vol. 12, no. 6, pp. 483–495, 2009.
- [49] S. J. Jackson and A. C. Perkins, "In vitro assessment of the mucoadhesion of cholestyramine to porcine and human gastric mucosa," *European Journal of Pharmaceutics and Biopharmaceutics*, vol. 52, no. 2, pp. 121–127, 2001.
- [50] E. Szymańska, K. Winnicka, A. Amelian, and U. Cwalina, "Vaginal chitosan tablets with clotrimazole-design and evaluation of mucoadhesive properties using porcine vaginal mucosa, mucin and gelatine," *Chemical and Pharmaceutical Bulletin*, vol. 62, no. 2, pp. 160–167, 2014.
- [51] G. P. Panizzon, F. G. Bueno, T. Ueda-Nakamura, C. V. Nakamura, and B. P. Dias Filho, "Preparation of spray-dried soy isoflavone-loaded gelatin microspheres for enhancement of dissolution: formulation, characterization and *in vitro* evaluation," *Pharmaceutics*, vol. 6, no. 4, pp. 599–615, 2014.
- [52] J. P. Soares, J. E. Santos, G. O. Chierice, and E. T. Cavalheiro, "Thermal behavior of alginic acid and its sodium salt," *Eclética Química*, vol. 29, no. 2, pp. 53–56, 2004.
- [53] J. Tuomilehto, J. Lindström, J. G. Eriksson et al., "Prevention of type 2 diabetes mellitus by changes in lifestyle among subjects with impaired glucose tolerance," *The New England Journal of Medicine*, vol. 344, no. 18, pp. 1343–1350, 2001.
- [54] I. Ruiz-Tamayo, J. Franch-Nadal, M. Mata-Cases et al., "Non-insulin antidiabetic drugs for patients with type 2 diabetes mellitus: are we respecting their contraindications?" *Journal of Diabetes Research*, vol. 2016, Article ID 7502489, 9 pages, 2016.
- [55] A. Y. Y. Cheng and I. G. Fantus, "Oral antihyperglycemic therapy for type 2 diabetes mellitus," *Canadian Medical Association Journal*, vol. 172, no. 2, pp. 213–226, 2005.
- [56] G. Wilcox, "Insulin and insulin resistance," *The Clinical Biochemist Reviews*, vol. 2, no. 3, pp. 19–39, 2005.
- [57] S. Ou, K.-C. Kwok, Y. Li, and L. Fu, "In vitro study of possible role of dietary fiber in lowering postprandial serum glucose," *Journal of Agricultural and Food Chemistry*, vol. 49, no. 2, pp. 1026–1029, 2001.
- [58] G. López, G. Ros, F. Rincón, M. J. Periago, M. C. Martínez, and J. Ortuño, "Relationship between physical and hydration properties of soluble and insoluble fiber of artichoke," *Journal of Agricultural and Food Chemistry*, vol. 44, no. 9, pp. 2773–2778, 1996.
- [59] S. Busti, P. Coccetti, L. Alberghina, and M. Vanoni, "Glucose signaling-mediated coordination of cell growth and cell cycle in *Saccharomyces cerevisiae*," *Sensors*, vol. 10, no. 6, pp. 6195–6240, 2010.
- [60] A. Roy, A. D. Dement, K. H. Cho, and J.-H. Kim, "Assessing glucose uptake through the yeast hexose transporter 1 (Hxt1)," *PLoS ONE*, vol. 10, no. 3, Article ID e0121985, 2015.
- [61] G. L. Kellett, E. Brot-Laroche, O. J. Mace, and A. Leturque, "Sugar absorption in the intestine: the role of GLUT2," *Annual Review of Nutrition*, vol. 28, no. 3, pp. 35–54, 2008.
- [62] J. Zhang, C. Tiller, J. Shen et al., "Antidiabetic properties of polysaccharide- and polyphenolic-enriched fractions from the brown seaweed *Ascophyllum nodosum*," *Canadian Journal of Physiology and Pharmacology*, vol. 85, no. 11, pp. 1116–1123, 2007.
- [63] Y. Sharifuddin, Y.-X. Chin, P.-E. Lim, and S.-M. Phang, "Potential bioactive compounds from seaweed for diabetes management," *Marine Drugs*, vol. 13, no. 8, pp. 5447–5491, 2015.
- [64] H. Ali, P. J. Houghton, and A. Soumyanath, " α -Amylase inhibitory activity of some Malaysian plants used to treat diabetes; with particular reference to *Phyllanthus amarus*," *Journal of Ethnopharmacology*, vol. 107, no. 3, pp. 449–455, 2006.
- [65] Z. Ahmad, K. F. Zamhuri, A. Yaacob et al., "In Vitro anti-diabetic activities and chemical analysis of polypeptide-k and oil isolated from seeds of *Momordica charantia* (bitter gourd)," *Molecules*, vol. 17, no. 8, pp. 9631–9640, 2012.
- [66] C. A. Tarling, K. Woods, R. Zhang et al., "The search for novel human pancreatic α -amylase inhibitors: high-throughput screening of terrestrial and marine natural product extracts," *ChemBioChem*, vol. 9, no. 3, pp. 433–438, 2008.